

Model Correlation and Updating of Geometrically Nonlinear Structural Models using Nonlinear Normal Modes and the Multi-Harmonic Balance Method

By

Christopher I. Van Damme

A dissertation submitted in partial fulfillment of the requirements for the degree of

DOCTOR OF PHILOSOPHY
(Engineering Mechanics)

at the

UNIVERSITY OF WISCONSIN-MADISON

2019

Date of final oral examination: 08/16/2019

The dissertation is approved by the following members of the Final Oral Committee:

Matthew S. Allen, Professor, Engineering Mechanics

Jacob K. Notbohm, Assistant Professor, Engineering Mechanics

Dan Negrut, Professor, Mechanical Engineering

Bill A. Sethares, Professor, Electrical and Computer Engineering

Joseph J. Hollkamp, Senior Aerospace Engineer, Air Force Research Laboratory

Abstract

Future generations of advanced spacecraft and aircraft will have a digital twin, or a model that is used to predict life and that is updated as the vehicle ages. A key component of the digital twin concept is the structural dynamics surrogate model that is used to simulate the response of structural components to the loads that the vehicle experiences. The structural surrogate will be used to predict responses, stress and ultimately the estimated life of the vehicle.

The most common approach for modeling structures in the aerospace industry is the Finite Element (FE) method, which can accurately simulate the response of the structural components due to various loading conditions. Many of these advanced vehicles will also be operating in extreme environments where certain components may behave nonlinearly such as the large deformations of thin panels. As a result, to use an FE model to simulate the response would be extremely expensive. To circumvent the use of FE models to compute the nonlinear response of structures, methods have been sought to create reduced order models (ROM)s, which capture the essential characteristics of the parent FE model but at a greatly reduced computational cost. One disadvantage of ROMs is that it tends to be more difficult to ensure that they are accurate. Regardless of the numerical modeling approach used they are unlikely to exactly represent the physical structure. As a result, model correlation and updating procedures are required to ensure they are accurate representations of the real hardware.

Unfortunately, linear model correlation and validation techniques that are commonly used in the aerospace industry are no longer valid in the nonlinear response regime so a new set of tools is required to validate nonlinear models. Both the nonlinear FE models and nonlinear ROMs can be highly sensitive to boundary conditions,

imperfections and pre-stresses which are difficult to account for in the initial model and thus model updating is required. Furthermore, as the structure ages, changes to the structure can occur and must be properly accounted for to ensure life predictions remain accurate.

The primary contribution of this work is the development of a model correlation and updating procedure applied to both FE models and ROMs based upon Nonlinear Normal Modes (NNMs) computed using the Multi-Harmonic Balance method. The NNMs serve as a strong metric to correlate the numerical models, because they represent the dynamics of the nonlinear system over a range of amplitudes and they are independent of the loading applied to the system. NNMs can be extracted from experiments so that numerical models can be correlated and validated with test data. This work presents a novel method of computing analytical gradients of the NNMs' solutions with respect to system parameters greatly accelerating the model updating procedure. The procedure is applied to both FE models and ROMs for several experimental systems demonstrating the capabilities of the model updating procedure for the two representations of geometrically nonlinear systems.

Acknowledgments

First off, I would like to give special thanks to my advisor, Prof. Matt Allen, for all of his help and support throughout my graduate career, and time as his Ph.D student. He has always been available and willing to give me guidance when needed. He has always encouraged me to pursue new and challenging opportunities. He has taught me valuable lessons not only in the field of engineering but also by being an example of an outstanding person that is hardworking, honest and dependable.

I would like to extend my gratitude to my Ph.D committee for taking the time to review the material in my dissertation and for the feedback they have provided. I would like to extend a special thanks to Dr. Joe Hollkamp for his feedback on my work throughout my graduate career. His insight into nonlinear dynamics, and nonlinear reduced order modeling has been instrumental to my work.

I thank all of my lab members for their contributions, collaborations and assistance during my time at UW-Madison.

I would like to acknowledge that this work was supported by the Air Force Office of Scientific Research, Award # FA9550-17-1-0009, under the Multi-Scale Structural Mechanics and Prognosis program managed by Dr. Jaimie Tiley.

Finally, I would like to thank my family, friends, and loved ones for all of their support throughout my entire education, especially during graduate school, and my Ph.D work. They have provided a strong foundation for which I have relied heavily on to achieve my goals.

Abbreviations

FE	:	Finite Element
FEM	:	Finite Element Model
ROM	:	Reduced Order Model
DOF	:	Degrees of Freedom
SDOF	:	Single Degree of Freedom
MDOF	:	Multiple Degrees of Freedom
IC	:	Implicit Condensation
LASSO	:	Least Absolute Shrinkage and Selection Operator
LNM	:	Linear Normal Mode
NNM	:	Nonlinear Normal Mode
HB	:	Harmonic Balance
MHB	:	Multi-Harmonic Balance
FEP	:	Frequency-Energy Plot
BC	:	Boundary Condition
CV	:	Cross Validation
MAC	:	Modal Assurance Criteria

Nomenclature

$\mathbf{x}, \dot{\mathbf{x}}, \ddot{\mathbf{x}}$	=	displacement, velocity and acceleration in physical coordinates
$\mathbf{M}, \mathbf{C}, \mathbf{K}$	=	Mass, Damping and Linear Stiffness Matrices in physical coordinates
\mathbf{f}_{nl}	=	nonlinear restoring force in physical coordinates
\mathbf{f}	=	external force in physical coordinates
$\mathbf{q}, \dot{\mathbf{q}}, \ddot{\mathbf{q}}$	=	displacement, velocity and acceleration in modal coordinates
ω_r	=	Frequency (<i>rad/sec</i>) for the r^{th} mode
φ_r	=	Mass normalized mode shape for the r^{th} mode
ζ_r	=	Damping ratio for the r^{th} mode
θ_r	=	Nonlinear restoring force for the r^{th} mode
α_r	=	Nonlinear quadratic stiffness coefficients for the r^{th} mode
β_r	=	Nonlinear cubic stiffness coefficients for the r^{th} mode
Λ	=	Modal linear stiffness matrix
\mathbf{z}	=	Fourier coefficient vector of displacement
\mathbf{F}	=	Fourier coefficient vector of nonlinear internal force and external force
$\mathbf{Q}(t)$	=	Transformation matrix from frequency to time domain
\mathbf{h}	=	Harmonic balance residual
$\mathbf{A}(\omega)$	=	Linear dynamic matrix in frequency domain
∇	=	Frequency coefficient matrix for frequency domain damping matrix
∇^2	=	Frequency coefficient matrix for frequency domain inertia matrix
$\Gamma(\omega)$	=	Inverse Fourier transformation as linear operator
$\Gamma(\omega)^+$	=	Fourier transformation as linear operator

Π = Model Updating objective function

$\mathbf{W}_s, \mathbf{W}_p$ = Weight matrices for state variables and design parameters respectively

γ = Total design scaling variable

$\Delta \mathbf{y}$ = State variable error vector

$\Delta \mathbf{p}$ = Parameter change vector

\mathbf{D} = Design sensitivity matrix

\mathbf{p} = Design parameter vector

Subscripts

h = harmonic index

p = parameter index

s = state variable index

Contents

1	Introduction	1
1.1	Motivation	1
1.2	Nonlinear Systems	5
1.3	Nonlinear Modal Analysis	10
1.4	Nonlinear Model Updating	13
2	Geometrically Nonlinear Systems	18
2.1	Nonlinear Finite Element Models	18
2.2	Nonlinear Reduced Order Models	19
2.2.1	Generating Static Force - Displacement Data	21
2.2.2	Least Squares Estimator	23
2.2.3	Least Absolute Shrinkage and Selection Operator (LASSO)	24
2.2.4	Repeated k-Fold Cross-Validation and Hyper-parameter Selection . .	25
2.2.5	Discussion on Computational Cost	27
2.3	Application to Flat Clamped-Clamped Beam	27
2.3.1	Rom Training and Nonlinear Stiffness Terms	28
2.3.2	Dynamic Accuracy Evaluation	29
2.4	Curved Panel	32
2.4.1	Training and Nonlinear Stiffness Identification	33
2.4.2	Dynamic Accuracy Evaluation	36
2.5	Recap	39

3	Nonlinear Modal Analysis	39
3.1	Introduction	39
3.2	Harmonic Balance Method	40
3.2.1	Frequency Domain Formulation	41
3.2.2	Determination of Nonlinear Terms and Derivatives	44
3.3	Continuation Routine	47
3.3.1	Predictor Step	48
3.3.2	Corrector Step	49
3.4	Nonlinear Normal Mode Formula	50
3.5	Application to Nonlinear Finite Element Models	51
3.5.1	Flat Clamped-Clamped Beam	51
3.5.2	Curved Clamped-Clamped Beam	56
3.5.3	Discovery Experimental Panel	61
3.5.4	Scaling Analysis	63
3.5.5	Discussion	67
3.6	Application to Nonlinear Reduced Order Models	67
3.6.1	Flat Clamped-Clamped Beam	67
3.6.2	Discovery Experimental Panel	70
3.6.3	Curved Clamped-Clamped Beam	75
3.6.4	Discussion	77
4	Nonlinear Model Updating Procedure	78
4.1	Algorithm Overview	78

4.2	Gradient Based Optimization Routine Setup	79
4.3	Computation of NNM Design Sensitivities within Harmonic Balance Framework	82
4.3.1	Reduced Order Model Nonlinear Internal Force Gradient	88
4.3.2	Finite Element Model Nonlinear Internal Force Gradient	91
4.3.3	Constraint on Linear Normal Mode Frequency of FE Models	94
4.3.4	Solution Selection	96
4.4	Application to Reduced Order Models	96
4.4.1	Flat Clamped-Clamped Beam - Numerical Demonstration	96
4.4.2	Curved Clamped-Clamped Beam - Numerical Demonstration	102
4.4.3	Flat Plate - Numerical Demonstration	103
4.5	Application to Finite Element Models	107
4.5.1	Boundary Springs of Flat Clamped-Clamped Beam	107
4.6	Recap	108
5	Model Updating Applied to Experimental Systems	109
5.1	Experimental Setup and Data Acquisition	110
5.1.1	Measuring Nonlinear Normal Modes using Force Appropriation	112
5.2	Application to Nominally Flat Beam	113
5.2.1	Modeling	114
5.2.2	Linear Model Updating	115
5.2.3	Nonlinear Reduced Order Model Updating	116
5.2.4	Nonlinear Finite Element Model Updating	120
5.2.5	Comparing Final Reduced Order Models	121

5.2.6	Discussion	123
5.3	Curved Beam	124
5.3.1	Experimental Data	126
5.3.2	Modeling	126
5.3.3	Linear Model Updating	130
5.3.4	Nonlinear Reduced Order Model Updating	131
5.3.5	Nonlinear Finite Element Model Updating	137
5.3.6	Comparing Final Reduced Order Models	143
5.3.7	Discussion	144
5.4	Exhaust Cover Plate	146
5.4.1	Modeling	147
5.4.2	Linear Finite Element Model Updating	149
5.4.3	Nonlinear Reduced Order Model Updating	152
5.4.4	Discussion	158
5.5	Recap	159
6	Conclusion	159
7	Future Work	161
7.1	Thermal Effects	162
7.2	Updating FE Models to Match Nonlinear Reduced Order Models	163
	Appendices	165
A	Publications of PhD Work	165

A.1 Journal	165
A.2 Conference	165
B Exhaust Plate : Nonlinear Finite Element Model Updating	166
References	168

1 Introduction

1.1 Motivation

In the future it is expected that many advanced spacecraft and aircraft will have a digital twin, or a model that is used to predict life, that is updated as the vehicle ages [1, 2]. A key component of this framework is a structural surrogate model that can accurately and efficiently compute the dynamic response of the vehicle. To ensure accuracy and confidence in the numerical model's predictions, model correlation, updating, and validation are required. Methods already exist for creating and updating linear structural models, but advanced vehicles may contain nonlinear vibration absorbers, joints or thin panels that exhibit nonlinearity. New strategies are needed both to correlate the digital twin to tests on the prototype structure and to update it as the structure ages.

The focus of this work is on structures with geometric nonlinearities, in particular that of large deformations where the material response remains elastic. The thin structural panels on aerospace vehicles [3, 4] are known to exhibit this response. The external panels of high performance aerospace vehicles are excited by large acoustic pressure fluctuations during flight [5, 6]. These large dynamic pressure loads, along with extreme thermal expansion conditions result in large amplitude vibration, sometimes about multiple equilibrium known as snap-through buckling [7, 8]. Another nonlinear phenomena present is panel-flutter in which the system loses stability and enters a limit cycle oscillation [9].

The finite element (FE) method is one analysis technique that is commonly used to simulate the dynamic response of geometrically nonlinear systems. For the particular structures of interest, thin structural panel undergoing large deformation, it has been demonstrated to

be accurate in the environments of interest [10]. While the method is accurate, robust, and is widely used, it does pose a challenge as being a viable tool for simulating the structural response of a digital twin. In particular, the computational cost associated with integrating the nonlinear response of large FE models for the time durations needed is infeasible even with today's computing resources [11].

A feasible alternative for a digital twin structural surrogate is to use a nonlinear modal model, or commonly referred to as a nonlinear reduced order model (ROM). ROMs can be defined as a projection of the physical degree-of-freedom (DOF) down to a smaller subset of DOF, typically through a Galerkin projection. In the case of a nonlinear modal model, the reduced domain DOF are comprised of a subset of the underlying linear normal modes (LNM)s of the system. Typically the number of modes is much less than physical DOF resulting in a more efficient model. The nonlinear modal model is a viable digital twin surrogate because it is able to predict the response of structures accurately [12, 13] with computational costs orders of magnitude less than a nonlinear FE model.

ROMs can be built in a variety of different ways. There are intrusive methods that require access to FE shape functions [14, 15, 16, 17], i.e. the source code is typically not available to users for commercial codes, to create the nonlinear stiffness terms in the modal domain. Alternatively, there are non-intrusive methods that only require outputs returned by a standard nonlinear FE code [13, 10, 18]. Lastly, there are system identification techniques that attempt to make a ROM from experimental data [11].

Regardless of which numerical approach is being used, i.e. a FE model or a ROM, neither numerical model is likely to represent the real structure exactly. Modeling approximations of the FE model such as boundary conditions, imperfections, and pre-stress due to assembly

may introduce inaccuracies. Boundary conditions have shown to have a significant effect on the response of geometrically nonlinear structures [19]. Depending on how the thin panels are assembled, imperfections and pre-stress may occur potentially altering the effective inplane stiffness of the structure, which is known to have a strong influence on the response of the panels. These modeling errors can manifest themselves in the response predictions thus affecting the life predictions of the FE model. Any modeling errors in the FE model will also manifest themselves in the ROM as well.

To ensure accurate life estimations, the model must be correlated, updated and validated with respect to field data at various stages. The first stage would be considered the pre-flight design evaluation stage where an initial model would be validated to ensure that the model's life predictions are accurate. The second stage would be the service stage where flight data is acquired, processed, and used for correlation in addition to more traditional post-flight testing. This data is necessary to ensure that any possible structural changes are incorporated into the models for future life estimations. Procedures like this have been done for linear systems [20, 21] but the inclusion of multi-physics and geometric nonlinearity introduce additional complications.

A difficulty of geometrically nonlinear structures, and nonlinear systems in general, is the amplitude dependence of the response. In contrast to linear systems, the numerical model must be valid not only for a variety of different loading scenarios but also over a wide range of amplitudes. In the context of model updating, this requires acquiring test data at multiple amplitudes, simulating the response at each of these amplitudes, and ensuring consistent response between them. This procedure can be a cumbersome approach to nonlinear model updating.

Linear structural dynamic model validation techniques [22, 23, 24] are commonly used in the aerospace industry. The most popular updating approaches use the linear modal data of the system, i.e. the natural frequencies and mode shapes, as a comparison metric to tune the parameters of a numerical model. This procedure is prominently used because the modal properties dictate the response of the linear system. Furthermore, they are a load independent metric that limits the amount of data needed during updating. However, as the response amplitude increases the fundamental frequencies can be amplitude dependent and nonlinear modal coupling may occur limiting the applicability of test, analysis, and updating procedures based on linear modal analysis.

This work proposes to use nonlinear modal analysis as a medium to correlate, update and validate both geometrically nonlinear FE models and ROMs. Particular emphasis is placed on nonlinear normal modes (NNMs), which are an extension of linear normal modes to nonlinear systems [25]. Nonlinear normal modes represent how the resonant frequencies and mode shapes change as a function of amplitude. Due to NNM's strong theoretical background as the backbones of nonlinear systems [26], their ability to be computed efficiently for both ROMs [27] and FE modes [28] and the ability to be determined experimentally [29, 30, 31] they make a strong medium with which to update nonlinear systems. In particular, this work utilizes the Multi-Harmonic Balance (MHB) as the numerical approach to compute NNMs and identify the design sensitivities of the parameters in the model updating routines greatly accelerating the model updating procedure. A brief outline of previous work on the subject, what this thesis adds to the field is shown in Figure 1.

The primary contribution of this work is the development of a model correlation and updating procedure applied to both FE models and ROMs based upon NNMs computed using

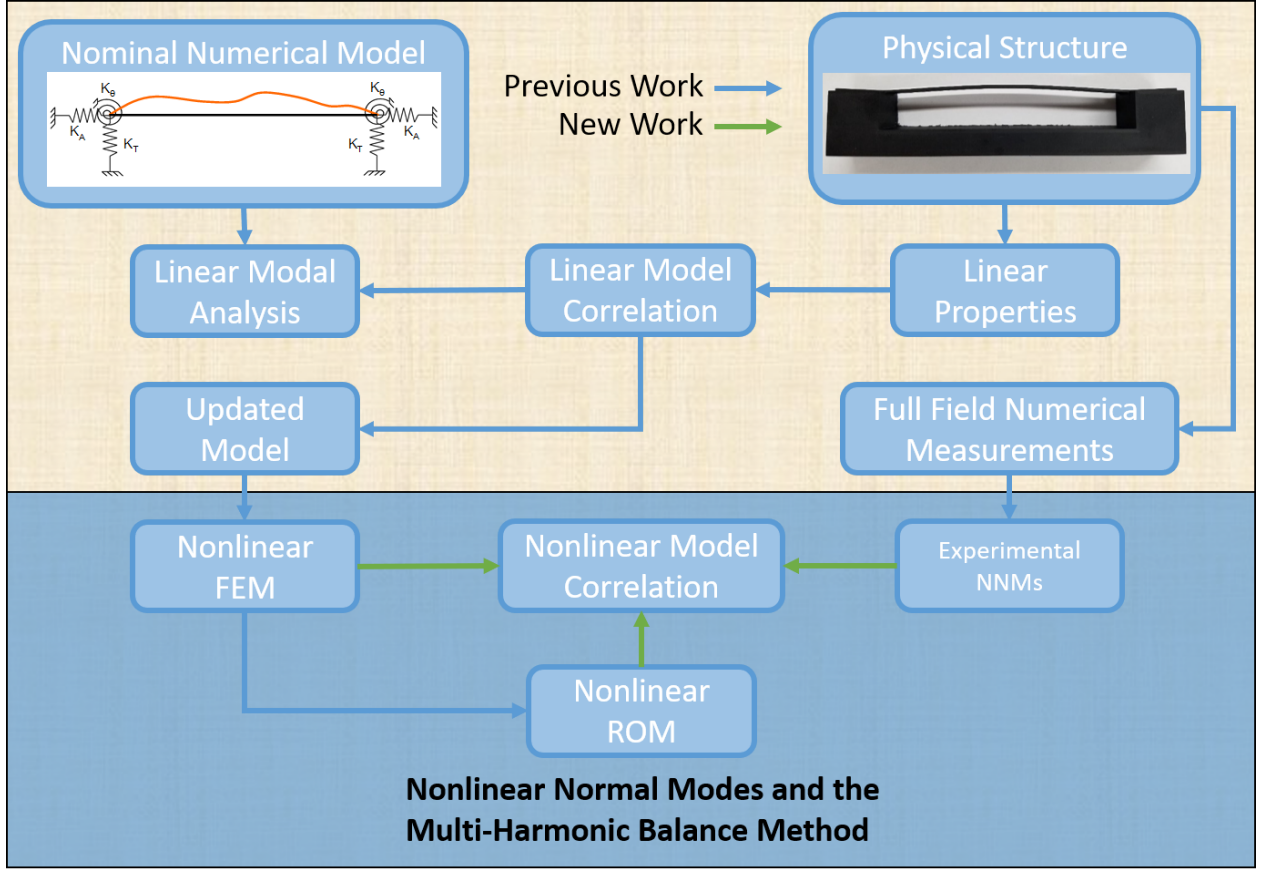


Figure 1: Overview of model updating procedure with previous work and work this thesis contributes to the field.

the MHB method. The two nonlinear systems, nonlinear FE models and nonlinear ROMs, are presented in Section 1.2. Nonlinear modal analysis applied to the nonlinear systems, nonlinear normal modes and the MHB method is discussed in Section 1.3. A literature review is presented of existing methods in nonlinear model correlation, and updating in Section 1.4.

1.2 Nonlinear Systems

Nonlinearity has many forms in structural systems such as geometric nonlinearity [32, 33, 34], damping in joints [35, 36], contact nonlinearity [37, 38], and material nonlinearity [39, 40, 41]. This work focuses on geometrically nonlinear systems, in particular large deformation

geometric nonlinearity that arises in thin-structural components where the material response remains linear elastic. These structural systems are commonly found in aerospace structures such as the skin panels on aircraft [3, 4]. The external excitation in hypersonic flow has a random broadband component [12] and long time durations are required to accurately capture the response statistics so one can predict the life of the structure. Furthermore, thermal expansion may occur in different magnitudes along the vehicle's trajectory making this a path-dependent problem [42].

The finite element method is one of the most commonly used structural simulation tools and can be applied to model the problems at hand accurately. The finite element equation of motion for a linear elastic system with geometric nonlinearity can be expressed as

$$\mathbf{M}\ddot{\mathbf{x}} + \mathbf{C}\dot{\mathbf{x}} + \mathbf{K}\mathbf{x} + \mathbf{f}_{nl}(\mathbf{x}) = \mathbf{f}_{ext}(t) \quad (1)$$

where nonlinearity of these systems is captured by the nonlinear internal force $\mathbf{f}_{nl}(\mathbf{x})$ function which is dependent on the deformation of the structure.

Although the FE method is a versatile, robust and widely used tool, its disadvantage for the structures of interest is the computational cost associated with integrating the dynamics response of large FE models required to represent the aerospace structures accurately. The primary two variants of time integration; explicit and implicit both have drawbacks for large systems that must be integrated for a long duration. Implicit integration and its many forms, see [43], are desirable for linear structural dynamics applications because they can take large time steps. Yet for geometrically nonlinear analysis they have the drawback that at each iteration of each time step the stiffness matrix must be reassembled and re-factored

[43]. Explicit time integration, on the other hand can compute each step efficiently because it does not require assembly or factorization of the global stiffness matrix [43]. The limiting factor for explicit integration is that the scheme must adhere to a conditionally stable time step that is generally orders of magnitude smaller than an implicit step.

An efficient alternative to the integration of the FE model is to use a reduced order model (ROM) to compute the nonlinear dynamic response [12] in a subspace of the original feature space. The reduction procedure uses a Galerkin approach to project the physical response onto a subset of basis vectors. Typically the number of basis vectors is much less than the physical degrees of freedom of the FE model resulting in enormous computational savings. A variety of potential basis vectors may be chosen but in the cases of interest the underlying linear normal modes of the system are used in the basis resulting in a geometrically nonlinear modal model.

The earliest complete work on the subject and development of ROMs dates back to 1977 with work of Nash [14]. This analysis approach has gained a significant amount of attention over the past few decades with numerous review papers [13, 44] and different approaches to the ROM creation procedure. The response of a linear elastic finite element, when using quadratic-strain displacement relations [32], contains a nonlinear restoring force that is quadratic and cubic. The linear properties of the modal model are similar to that of a conventional modal model which are a function of which modes are used in the coordinate transformation. An example of a two-mode ROM is

$$\begin{aligned}
& \begin{bmatrix} 1 & 0 \\ 0 & 1 \end{bmatrix} \begin{Bmatrix} \ddot{q}_1 \\ \ddot{q}_2 \end{Bmatrix} + \begin{bmatrix} 2\zeta_1\omega_1 & 0 \\ 0 & 2\zeta_1\omega_1 \end{bmatrix} \begin{Bmatrix} \dot{q}_1 \\ \dot{q}_2 \end{Bmatrix} + \begin{bmatrix} \omega_1^2 & 0 \\ 0 & \omega_2^2 \end{bmatrix} \begin{Bmatrix} q_1 \\ q_2 \end{Bmatrix} + \dots \\
& \begin{bmatrix} A_{1,1}^{(1)} & A_{1,2}^{(1)} & A_{2,2}^{(1)} \\ A_{1,1}^{(2)} & A_{1,2}^{(2)} & A_{2,2}^{(2)} \end{bmatrix} \begin{Bmatrix} q_1^2 \\ q_1 q_2 \\ q_2^2 \end{Bmatrix} + \begin{bmatrix} B_{1,1,1}^{(1)} & B_{1,1,2}^{(1)} & B_{1,2,2}^{(1)} & B_{2,2,2}^{(1)} \\ B_{1,1,1}^{(2)} & B_{1,1,2}^{(2)} & B_{1,2,2}^{(2)} & B_{2,2,2}^{(2)} \end{bmatrix} \begin{Bmatrix} q_1^3 \\ q_1^2 q_2 \\ q_1 q_2^2 \\ q_2^3 \end{Bmatrix} = \begin{Bmatrix} \phi_1^T \mathbf{f}(t) \\ \phi_2^T \mathbf{f}(t) \end{Bmatrix}
\end{aligned} \tag{2}$$

where the nonlinearities of the model are contained within the coefficients A and B that are the quadratic and cubic polynomial nonlinear stiffness terms of the ROM. These terms are dependent on properties that affect the geometrically nonlinear response of the FE model.

There are two main classes of reduced order modeling for geometrically nonlinear structures; intrusive methods that require the inner workings of the FE code, and non-intrusive methods that utilize the standard nonlinear solution capabilities of the FE software. This work will focus on non-intrusive methods, however for an introduction to intrusive methods the reader is referred to [15].

There are two common non-intrusive approaches to ROM building. The first being the enforced displacement (ED) procedure originally developed by Muravyov and Rizzi [45]. This method has been enhanced by Mignolet [13] for complex structures. The other method, which relies on an applied loads procedure termed Implicit Condensation (IC), was developed by McEwan [46]. It was later enhanced to include accurate predictions of membrane stress in

a method termed Implicit Condensation and Expansion (ICE) [47]. The former is a non-intrusive approach where algebraic operations lead to the determination of ROM parameters whereas the latter is an estimation routine which requires regression analysis.

All of these modeling approaches have been shown to create accurate low order models that can compute the nonlinear dynamic response of structures at a significantly lower cost than the conventional FE method [44, 13]. They have been demonstrated to be accurate for random response, transient response, and steady state.

A computational comparison of the cost to integrate a typical nonlinear system can be given by considering the system in Section 3.5.3. The FE model contains 8734 elements with a total of 53,748 DOF. This FE model is a relatively small in comparison to what would be used for the analysis of an aircraft panel. The integration of the nonlinear system using the implicit and explicit schemes on the full FE model, and using implicit scheme on a few reduced order models is presented in Table 1. ROMs are able to integrate the response of the system orders of magnitude faster than the FE method. Using an implicit scheme with a large numerical damping value, α , results in the fastest FE computation but is not advisable since the numerical damping can tend to damp out high frequency vibrations excited through bending-stretching coupling of the nonlinear structures. It is important to note that there is a computational cost to generate ROMs, this is normally negligible for ROMs with 5 or less modes but for larger ROMs, such as the 25 mode ROM mentioned below, it may take a few hours to create. In those situations it still may be advantageous to create a ROM if one needs to find the response to several loadings.

Table 1: Computational time (minutes) to integrate the nonlinear system described in Section 3.5.3 for a 10 second simulation under random broadband loading with amplitude such that nonlinear response is on order of 2x the structure’s thickness. Computations were performed on a Intel(R) Core(TM) i7-7700K CPU @ 4.20GHz.

FE Model Abaqus ®			ROM				
Implicit		Explicit	1 Mode	3 Mode	5 Mode	10 Mode	25 Mode
$\alpha = -0.1$	$\alpha = -0.01$						
428	783	583	0.05	0.1	0.25	0.5	2.5

1.3 Nonlinear Modal Analysis

Nonlinear modal analysis is aimed at identifying, computing, and understanding the nonlinear periodic response of structures. This work will divide the field into two main categories, the undamped-unforced response and damped-forced response, where the former is related to the concept of a Nonlinear Normal Mode (NNM) which is extensively used in this work.

In the context of structural dynamics, the term nonlinear normal mode was introduced by Rosenberg in 1960 [25] to be defined as the periodic motion of a conservative nonlinear system with symmetric potential function such that each point passes through the equilibrium at the same instant in time, i.e. synchronous vibration. Decades later this definition was relaxed by Vakakis, Kerschen, and others [48, 26] to the case in which the response of an undamped and unforced nonlinear normal mode may be considered as a *not necessarily synchronous periodic response*. This is the definition that will be used in this work. Alternatively, Shaw and Pierre [49, 50] defined the NNM as a two-dimensional invariant manifold in phase space which are tangent to the linear normal modes (LNM)s, which are a plane in phase space, at the equilibrium point. This definition provides an extension of NNMs to non-conservative systems, i.e. damped systems.

An illustrative example of a nonlinear normal mode's importance for a geometrically nonlinear system is demonstrated below. Consider the curved beam shown in Figure 2 with a base excitation and velocity recorded at the center. The structure is excited using a swept-sine base excitation from 120 to 170 Hz at various amplitudes.

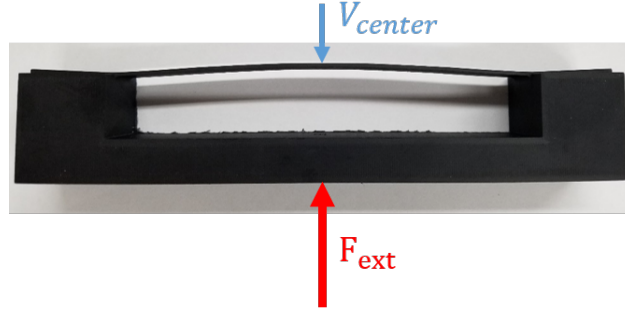


Figure 2: 3D-printed curved beam with base excitation shown and response .

The response of the structure due to the excitation is presented in Figure 3 where the underlying nonlinear normal mode of a curved beam is overlayed on response. As the amplitude of the swept-sine excitation increases the maximum response amplitude occurs at a different frequency. For a linear system, this would not be the case, the maximum amplitude would remain at a constant frequency, i.e. the linear normal mode frequency. Furthermore, notice that the maximum amplitude of the swept-sine response occurs at the frequency where the NNM intersects the response. In other words, the NNM could be used to predict the frequency of the peak response. This example demonstrates that the nonlinear normal mode, defined based upon an unforced-undamped nonlinear system, is the backbone of the damped-forced nonlinear system. Hence, it is an excellent metric to use for model updating.

In addition to the amplitude dependent resonance seen above, nonlinear dynamic systems can have a wide variety of phenomena occur such as internal resonances, bifurcations and

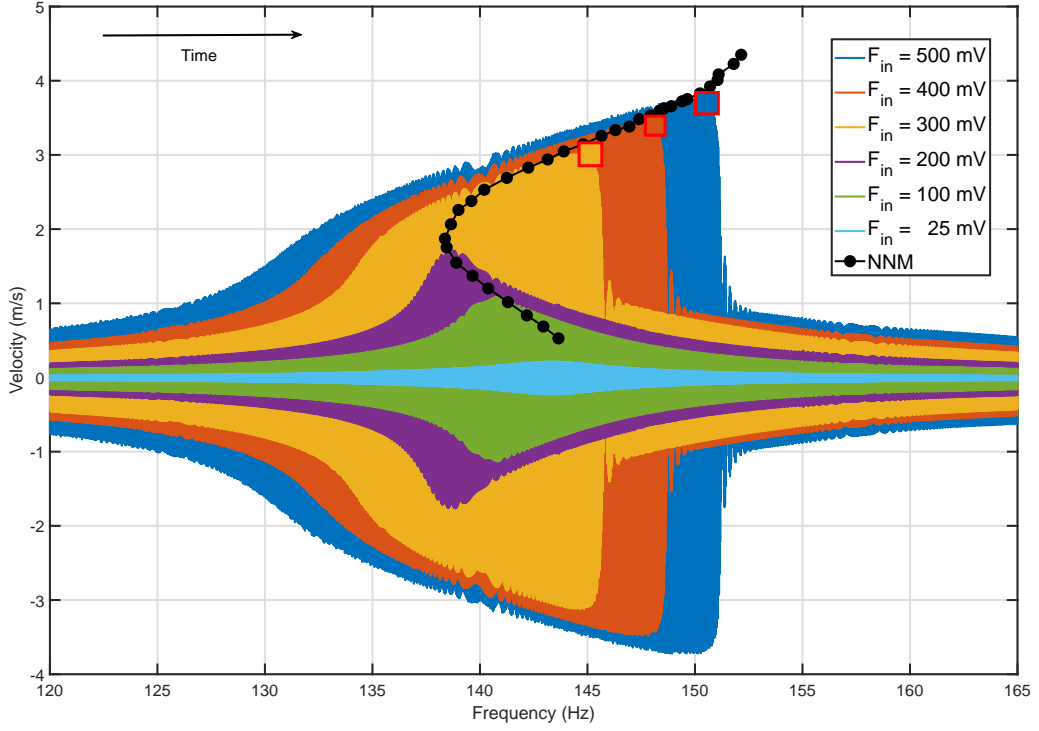


Figure 3: Velocity response at center of curved beam due to swept sine base excitation. The underlying nonlinear normal mode is overlayed on the swept sine response.

super/sub harmonic resonances [51, 52]. Interestingly, Figure 3 shows a beautiful demonstration of a typical bifurcation in geometrically nonlinear systems. The bifurcation points are designated by the squares in Figure (3) and occur for forcing amplitudes of 300, 400, and 500 mV where the velocity suddenly drops after reaching a maximum amplitude. This bifurcation occurs because of multiple solutions to the force-damped nonlinear system.

The other phenomena that are of importance for geometrically nonlinear systems are internal resonances, which have a significant impact on the cost of computing NNMs. Internal resonances are nonlinear modal interactions that occur when integer multiples of the NNMs sum to zero. Internal resonances are demonstrated in Figure 4 which is from [53] where

the Multi-Harmonic Balance (MHB) method was used to filter internal resonances. This numerical approach will be discussed in detail in Section 3, but it relies on approximating the periodic response using a subset of Fourier coefficients thus being able to filter out higher harmonics of the system. As a result it is a computationally efficient approach to computing NNMs for both ROMs and FE models.

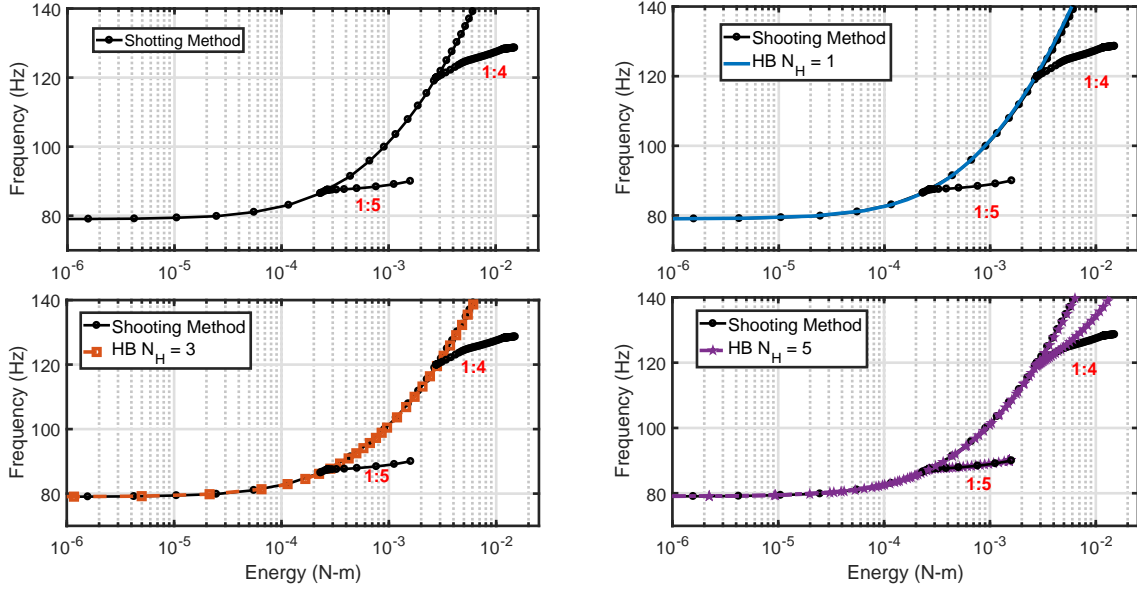


Figure 4: Nonlinear normal mode of a flat steel beam with fixed boundary conditions. The NNMs are computed using a shooting algorithm and the harmonic balance method with different numbers of harmonics, n_H included.

1.4 Nonlinear Model Updating

The model correlation and updating is concerned with the scenario in which the response of the model does not match that of the realistic structure. This process is necessary to ensure that the model is accurate and its predictions can be utilized for simulations when tests are not feasible, such as vehicle life predictions. Slight deviations in the curvature of a structure such as imperfection, pre-stress affecting the stiffness of the structure or non-ideal boundary

conditions may cause a discrepancy between a model's prediction and the structure's actual response.

An illustrative example of the free parameters present in a finite element model is presented in Figure 5 from [54] where the boundary conditions and imperfection of the model are demonstrated. The physical parameters of the structure are explicitly applied to the FE model, which then produces the FE equations of motion shown in Eq (3).

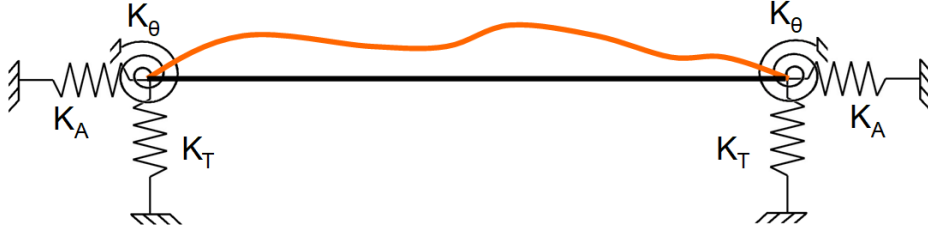


Figure 5: Schematic of a 2D model with input parameters of a finite element model including imperfection/curvature, and boundary stiffness terms.

$$\mathbf{M}(\mathbf{p})\ddot{\mathbf{x}} + \mathbf{C}(\mathbf{p})\dot{\mathbf{x}} + \mathbf{K}(\mathbf{p})\mathbf{x} + \mathbf{f}(\mathbf{p})_{\text{nl}}(\mathbf{x}) = \mathbf{f}_{\text{ext}}(t) \quad (3)$$

In this example the uncertain model parameters are the stiffnesses of the boundary springs and the curvature of the beam. These parameters are uncertain, or may not even be present in the model, for example if the beam was approximated as fixed-fixed rather than modeling the boundary as a spring. Any variability within the FE model will also propagate into the ROM regardless of the approach used to generate it. A 2-DOF ROM created from the finite element model represented in Eq (3) has the following dependency on the free parameters.

$$\begin{aligned}
& \begin{bmatrix} 1 & 0 \\ 0 & 1 \end{bmatrix} \begin{Bmatrix} \ddot{q}_1 \\ \ddot{q}_2 \end{Bmatrix} + \begin{bmatrix} 2\zeta_1\omega_1(\mathbf{p}) & 0 \\ 0 & 2\zeta_1\omega_1(\mathbf{p}) \end{bmatrix} \begin{Bmatrix} \dot{q}_1 \\ \dot{q}_2 \end{Bmatrix} + \begin{bmatrix} \omega_1^2(\mathbf{p}) & 0 \\ 0 & \omega_2^2(\mathbf{p}) \end{bmatrix} \begin{Bmatrix} q_1 \\ q_2 \end{Bmatrix} + \dots \\
& \begin{bmatrix} A_{1,1}^{(1)}(\mathbf{p}) & A_{1,2}^{(1)}(\mathbf{p}) & A_{2,2}^{(1)}(\mathbf{p}) \\ A_{1,1}^{(2)}(\mathbf{p}) & A_{1,2}^{(2)}(\mathbf{p}) & A_{2,2}^{(2)}(\mathbf{p}) \end{bmatrix} \begin{Bmatrix} q_1^2 \\ q_1 q_2 \\ q_2^2 \end{Bmatrix} + \dots \\
& \begin{bmatrix} B_{1,1,1}^{(1)}(\mathbf{p}) & A_{1,1,2}^{(1)}(\mathbf{p}) & A_{1,2,2}^{(1)}(\mathbf{p}) & A_{2,2,2}^{(1)}(\mathbf{p}) \\ B_{1,1,1}^{(2)}(\mathbf{p}) & A_{1,1,2}^{(2)}(\mathbf{p}) & A_{1,2,2}^{(2)}(\mathbf{p}) & A_{2,2,2}^{(2)}(\mathbf{p}) \end{bmatrix} \begin{Bmatrix} q_1^3 \\ q_1^2 q_2 \\ q_1 q_2^2 \\ q_2^3 \end{Bmatrix} = \begin{Bmatrix} \phi_1^T(\mathbf{p})\mathbf{f}(t) \\ \phi_2^T(\mathbf{p})\mathbf{f}(t) \end{Bmatrix} \quad (4)
\end{aligned}$$

The first three matrices contain the linear properties of the system identified from linear modal analysis and as such can be updated with linear updating techniques. The last two matrices, containing the A and B terms, represent the nonlinear terms of the ROM which are also dependent on the parameterization of the FE model.

Linear modal analysis is commonly used within the aerospace industry to correlate a numerical model with experimental data. There are review papers [23] and books [24, 22] describing the multitude of different approaches to model correlation, updating and validation. Within the field of structural dynamics, i.e. relatively low frequency dynamics, the most common correlation and updating procedure is to use the linear modal properties of the system, the linear frequencies and mode shapes. Nearly every commercial FE software is capable of extracting linear modal properties, experimental identification of modal properties

are well established and there is even automated model updating software available.

A natural extension of model updating using linear modal techniques is to use nonlinear normal modes as a model updating metric. There is a strong foundational theory and relation to linear normal modes. Nonlinear normal modes are load independent, thus reduce the number of scenarios which must be tested and simulated. They can be computed efficiently for both FE models [28, 55] and ROMs [53]. Non-destructive test procedures have been developed to extract them from physical structures [29, 31, 30].

There has been a recent surge in the field of nonlinear model updating due to increased interest in nonlinear designs, especially in the context of FE model updating. The first one to introduce the concept of using nonlinear normal modes in model updating was Peeters et al. [56] who used least squares regression to minimize the residual difference between FE predictions and experimental data. Following that Hill et al. [57] implemented a probabilistic Bayesian approach to identify the parameters of the model based on analytical backbone curves computed using a second-order normal forms technique. This approach is limited to weakly nonlinear systems and the analytical approach introduces additional errors. In subsequent work Wang [58] used an analytical backbone curve formulated using the normal forms method to update nonlinear elements of a FE model. That approach lacked the ability to model structures with strong nonlinearities.

In a very recent work, Song [59] updated FE models based on NNMs using both a deterministic approach and a Bayesian approach. In that work NNMs were computed using a shooting method which requires numerical gradients of the NNM curves, adding significant computational cost to the procedure as well as potentially following internal resonance branches if present. The Bayesian approach utilized Markov chain Monte-Carlo simulations

to generate the joint probability distribution between the model's NNM and measured target NNM.

In the context of ROM updating, Denis [60] tuned dimensionless nonlinear coefficients of a ROM, found using analytic equations of motion of circular plates, to match experimentally identified NNMs. In that work they utilized the normal forms procedure to isolate a ROM for each NNM. When using the normal forms procedure it assumes a single-degree of freedom response and as a result is unable to capture strong modal coupling if present along the NNM.

This work investigates two approaches to updating nonlinear models using NNMs; the first approach considers updating the parameters of a finite element model directly to match the experimental data whereas the second approach updates the nonlinear stiffness parameters of a ROM. Updating parameters of the FE model directly has the advantage of being able to have a strong physical intuition of the parameters, i.e. using springs to represent a boundary condition or the modulus of elasticity of the component. A drawback of updating the FE model directly is the computational cost of computing NNMs for large models which slows down the updating procedure.

Updating the coefficients of a ROM, on the other hand, has the advantage of being computationally cheap even for ROMs with many DOF. The downside of updating ROM coefficients is the lack of physical intuition into the parameters since they are represented as sums of quadratic and cubic coefficients. Since the goal is to obtain an accurate nonlinear model, the flexibility of tuning the ROM coefficients to capture the nonlinear response of a structure is appealing.

The multi-harmonic balance method is used in this work to compute NNMs of the nonlin-

ear systems because of its low computation cost, ability to filter internal resonances [61, 53] and because it allows one to compute the gradients of a geometrically nonlinear model analytically (i.e. rather than using finite differences) [27]. A graphical depiction of the model updating procedure is presented in subplot (a) of Figure 6 along with the procedural flow diagram in subplot (b). The theory is developed, studied on numerical cases, and finally applied to experimental examples which are presented in Section 5.

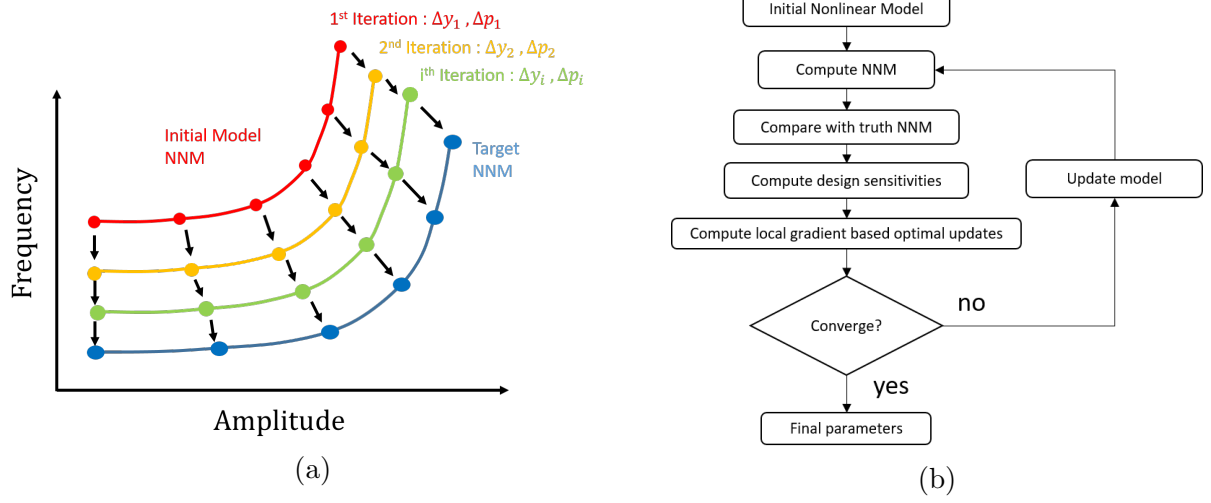


Figure 6: Representation of the model updating procedure: (a) graphical representation. (b) procedural flow-diagram.

2 Geometrically Nonlinear Systems

2.1 Nonlinear Finite Element Models

The geometrically nonlinear elastic FE equations of motion for an n DOF system can be written as

$$\mathbf{M}\ddot{\mathbf{x}} + \mathbf{C}\dot{\mathbf{x}} + \mathbf{K}\mathbf{x} + \mathbf{f}_{nl}(\mathbf{x}) = \mathbf{f}(t) \quad (5)$$

where \mathbf{M} , \mathbf{C} , and \mathbf{K} are the $(n \times n)$ mass, damping, and linear stiffness matrices respectively. \mathbf{x} , $\dot{\mathbf{x}}$, and $\ddot{\mathbf{x}}$ are the $n \times 1$ displacement, velocity, and acceleration vectors. The nonlinear restoring force $\mathbf{f}_{nl}(\mathbf{x})$ is a function of the displacement only. The $n \times 1$ external force vector $\mathbf{f}(t)$ can be random in both space and time. The nonlinear internal force vector can be written as

$$\mathbf{f}_{nl}(\mathbf{x}) = [\mathbf{K}_1(\mathbf{x}) + \mathbf{K}_2(\mathbf{x}, \mathbf{x})] \mathbf{x} \quad (6)$$

where \mathbf{K}_1 is the quadratic nonlinear stiffness matrix (linear function of displacements) and \mathbf{K}_2 is the cubic nonlinear stiffness matrix (quadratic function of displacements).

2.2 Nonlinear Reduced Order Models

The first step in reducing the system in Eq (5) is to identify the set of basis vectors used to span the ROM. Neglecting the damping, external force, and the nonlinear restoring force from Eq (5), the underlying linear modes shapes are found by solving eigenvalue problem in Eq (7)

$$(\mathbf{K} - \omega_r^2 \mathbf{M}) \boldsymbol{\varphi}_r = 0 \quad (7)$$

where $\boldsymbol{\varphi}_r$ is the r^{th} linear mode shape and ω_r is the linear natural frequency associated with the r^{th} mode. A coordinate transformation is used to express the physical displacement in terms of a subset of m linear modal coordinates as

$$\mathbf{x}(t) = \boldsymbol{\varphi}_m \mathbf{q}(t) \quad (8)$$

where $\boldsymbol{\varphi}_m$ is the $n \times m$ mass normalized mode matrix composed of the m mode shape vectors in the reduced basis set and \mathbf{q} is the $m \times 1$ vector of time dependent modal displacements. The modes included within the reduced basis set should be only those that contribute significantly to the response of the system. Substituting the coordinate transformation from Eq (8) back into Eq (5) and pre-multiplying by $\boldsymbol{\varphi}_m^T$, where $()^T$ is the transpose operator, the r^{th} nonlinear modal equation becomes

$$\ddot{q}_r + c_r \dot{q}_r + \omega_r^2 + \theta_r(q_1, q_2, \dots, q_m) = \varphi_r^T \mathbf{f}(\mathbf{x}, \mathbf{t}) \quad (9)$$

The nonlinear restoring force, θ_r , is a function of the modal displacements as follows:

$$\theta_r(\mathbf{q}) = \varphi_r^T \mathbf{f}_{nl}(\boldsymbol{\varphi}_m \mathbf{q}) \quad (10)$$

In [12] it was shown that the nonlinear restoring force for a linear elastic system with only geometric nonlinearities can be accurately approximated with quadratic and cubic terms as

$$\theta_r(q_1, q_2, \dots, q_m) = \sum_{i=1}^m \sum_{j=i}^m A_r(i, j) q_i, q_j + \sum_{i=1}^m \sum_{j=i}^m \sum_{k=j}^m B_r(i, j, k) q_i, q_j, q_k \quad (11)$$

where A_r and B_r are the quadratic and cubic nonlinear stiffness terms respectively. Additionally, the terms α_{ij} and β_{ijk} at times are used to reference the nonlinear quadratic and cubic coefficients denoted $A(i, j)$ and $B(i, j, k)$ respectively throughout this work. There are a few approaches to estimating the nonlinear coefficients of a ROM but in this work the focus is on the applied loads procedure termed Implicit Condensation as will be discussed in the following sections.

2.2.1 Generating Static Force - Displacement Data

When using the IC procedure estimating the nonlinear stiffness terms requires applying a series of static forces in the shapes of the modes to the full FE model. Each static load case consists of combinations of the m underlying linear mode shapes up to order three. For example, a multi-mode force is the combination of the individual eigenvectors with associated scale factor, \hat{f}_r , represented as

$$\mathbf{F}_c = \mathbf{M}(\hat{f}_1\boldsymbol{\varphi}_1 + \hat{f}_2\boldsymbol{\varphi}_2 + \dots \hat{f}_m\boldsymbol{\varphi}_m) \quad (12)$$

The scale factor for each mode can be computed by prescribing a desired displacement of a certain DOF of the model with the following equation

$$\hat{f}_r = \frac{\omega_r^2}{\boldsymbol{\varphi}_r^T \boldsymbol{\varphi}_r} \frac{x_c}{\boldsymbol{\varphi}_{r,c}} \quad (13)$$

where ω_r is the frequency of the mode of interest, x_c is the desired displacement magnitude of the DOF of interest, and $\boldsymbol{\varphi}_{i,c}$ is the entry of the DOF of interest in the mode shape considered. From [12, 62] it was found that displacements on the order of the thickness are sufficient to excite the nonlinearity of the system. For flat structures a single load case would typically suffice but for curved structure multiple amplitudes are required typically. In this work, the load scaling values are generated from a multivariate normal distribution with prescribed mean and standard deviation represented as μ and Σ . Once the load cases have been solved the displacement from the nonlinear static solutions are then projected onto the reduced domain using the basis set as

$$q_r = \boldsymbol{\varphi}_r^T \mathbf{M} \mathbf{x} \quad (14)$$

Since the nonlinear stiffness coefficients of the ROM are represented as polynomial terms, the training data for the regression problem can be transformed to a linear regression problem through a polynomial kernel method. The training matrix can be formed as

$$\mathbf{G} = \begin{bmatrix} q_1^2[1] & q_1 q_2[1] & \cdots & q_m^2[1] & q_1^3[1] & q_1^2 q_2[1] & \cdots & q_m^3[1] \\ q_1^2[2] & q_1 q_2[2] & \cdots & q_m^2[2] & q_1^3[2] & q_1^2 q_2[2] & \cdots & q_m^3[2] \\ & & \cdots & & & & \cdots & \\ q_1^2[N] & q_1 q_2[N] & \cdots & q_m^2[N] & q_1^3[N] & q_1^2 q_2[N] & \cdots & q_m^3[N] \end{bmatrix} \quad (15)$$

where $[\cdot]$ represents the sample number from one of the nonlinear static load cases within the total number of cases N . If multiple load levels are used in the training then the total number of cases which consist of several sub-cases of data of size N_L which would define enough load cases to create a single ROM as described in [12]. The nonlinear portion of the modal internal force, for each modal equation, is computed by removing the linear contribution to the internal force as

$$\mathbf{b}_{r,nl} = \begin{bmatrix} b_r[1] - \omega_r^2 q_r[1] \\ b_r[2] - \omega_r^2 q_r[2] \\ \vdots \\ b_r[N] - \omega_r^2 q_r[N] \end{bmatrix} \quad (16)$$

The regression problem to identify the parameters for the r^{th} mode can then be written

in the following form

$$\mathbf{G}\Theta_r = \mathbf{b}_{r,nl} \quad (17)$$

where Θ_r is the vector containing the unknown nonlinear stiffness coefficients A_r and B_r . Note that the same modal displacement matrix is used for each regression problem to identify the parameters for a given mode. For a given system the number of nonlinear coefficients, N_{Θ} , is a function of the number of modes m in the reduced linear basis set given by

$$N_{\Theta} = m \left(m + {}_m C_2 + m^2 + {}_m C_3 \right) \quad (18)$$

where ${}_m C_k = \frac{m!}{(m-k)!k!}$ [12]. Clearly, the number of nonlinear terms that must be found scales as $\mathcal{O}(m^3)$. For large basis sets the number of terms becomes extremely large with many possibly unimportant terms. In the context of model updating for ROMs this poses a complication because it results in a large number of terms to include in the updating procedure potentially adding significant computational time to the procedure.

2.2.2 Least Squares Estimator

Least squares regression is the approach used in most recent works (e.g.[12, 62]) to estimate the nonlinear stiffness coefficients. The least squares approach is proven, straight forward, and readily available in most scientific computing packages. For a set of observations, least squares finds the solution that minimizes the mean squared error on the L_2 norm as

$$\min_{\Theta_r} \|\mathbf{G}\Theta_r - \mathbf{b}\|_2^2 \quad (19)$$

The nonlinear stiffness terms from the least squares regression problem can be found via a closed form expression known as the normal equations as

$$\Theta_r = (\mathbf{G}^T \mathbf{G})^{-1} \mathbf{G}^T \mathbf{b}_r \quad (20)$$

or if the system size is large, this can be solved iteratively using a gradient descent approach or one of its many variants [63].

2.2.3 Least Absolute Shrinkage and Selection Operator (LASSO)

Even though ROMs significantly reduce the number of DOF in a given system, the number of parameters of the ROM can still be exceptionally large. Another drawback of computing ROMs using least squares regression is that there is no metric for determining which nonlinear stiffness terms contribute most to the dynamic response. This section of work explored the use of least absolute shrinkage and selection operator (LASSO) to identify sparse sets of of ROM nonlinear stiffness coefficients during regression to reduce the number of parameters in the ROM.

In essence the goal is to find a set of model coefficients, Θ_r , that minimizes the squared error and also that minimizes the number of terms in Θ_r , or its L_0 norm, as mentioned earlier. These are two competing objectives, so one would have to determine a weighting between them that produces the best results - i.e. the smallest model that has acceptable accuracy. In practice, it proves difficult to use the L_0 norm, however, an algorithm from the machine learning community known as LASSO is able to solve a similar problem.

For a set of observations, LASSO determines the solution that minimizes the mean

squared error on the l_2 norm *as well* as well as the l_1 norm of the coefficient vector. LASSO adds a penalty term to the least squares optimization function that is proportional to the l_1 norm, where a penalty of zero is simply least squares regression. LASSO, then minimizes the following optimization function

$$\min_{\Theta_r} ||\mathbf{G}\Theta_r - \mathbf{b}_r||_2^2 + \lambda ||\Theta_r||_1 \quad (21)$$

where λ is a regularization term associated with the LASSO procedure. The solutions become more sparse as this parameter is increased. There is no closed form solution of Eq (21) but it is still a convex optimization problem and can be solved iteratively using a coordinate descent algorithm [64], or the method of alternating direction method of multipliers [65]. In this work the Matlab $\text{\textcircled{R}}$ function *lasso* is utilized which uses the coordinate descent algorithm.

2.2.4 Repeated k-Fold Cross-Validation and Hyper-parameter Selection

Cross-validation is used in this work to provide an up-front identification of the accuracy of a ROM and to identify the optimal regularization term, λ . In this work we are using k-fold cross validation, although other forms are available such as exhaustive-, leave-p-out-, and leave-one-cross validation among many more [66]. k-Fold cross validation is a simple form of cross validation in which the set of available data is split into two portions; the training set and the validation set, with the number k referring to the number of groups the data is split into to. A graphical representation is demonstrated in Figure 7 The procedure is enhanced by including additional Monte Carlo repetitions for the cross validation. The Monte-Carlo repetitions, if desired, reshuffle the data randomly over the repetitions and the final result

can be averaged over each run. This is not required of the procedure but is used in this work to ensure shuffling of the data.

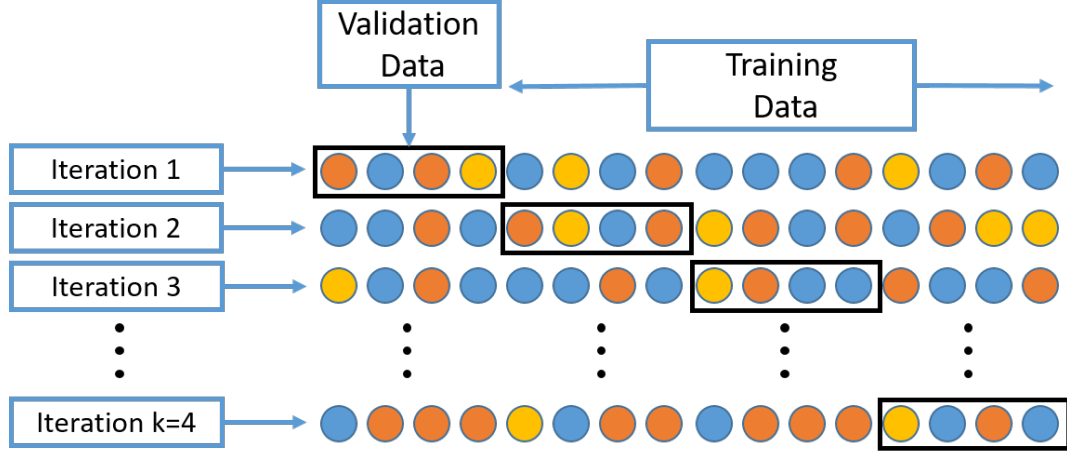


Figure 7: Graphical depiction of k-Fold cross validation with 4 folds.

The error function used is

$$E_k(\lambda) = \sum_{i \in k} (b_{r,i} - \mathbf{G}_i \Theta_{r,i}(\lambda))^2 \quad (22)$$

where the matrix \mathbf{G}_i consists of a subset of the polynomial coefficient matrix from Eq (15) and the vector $b_{r,i}$ consists of the a subset of the nonlinear modal forces corresponding to the validation set as defined by the k-fold cross validation procedure. The polynomial coefficients $\Theta_{r,i}(\lambda)$, are the polynomial coefficients subset of the coefficients estimated using the training set as defined by the k-fold cross-validation. The total error during cross-validation is found as

$$CV(\lambda) = \frac{1}{K} \sum_{k=1}^K E_k(\lambda) \quad (23)$$

Once the scores are retained from the cross-validation stage, one is able to select the

hyper-parameter, the lasso regularization parameter λ in this work, that provides the most accurate model. In the context of this work, the most accurate model is represented by the model which has the lowest MSE during cross validation.

2.2.5 Discussion on Computational Cost

One disadvantage of such an approach is that it tends to require a larger number of non-linear static load cases for a given ROM size. However, this cost is offline and completely parallelizable, each static load case can be computed independently of the others.

Another advantage of LASSO is its ability to help a model generalize when the number of observations is actually smaller than the number of prediction variables [67]. The reasoning behind such is that by providing the regularization term it prevents the regression from over-fitting to the provided data. This may be the case when it is too expensive to generate large amounts of data for large FE models or when a ROM with a large basis set is required. In this scenario LASSO may provide a model that generalizes better and is more accurate over a range of loading. This case is not considered in this work but might be interesting to address in future works.

2.3 Application to Flat Clamped-Clamped Beam

The first numerical study is a flat clamped-clamped beam in which geometric nonlinearity is accounted for. This beam has been used in numerous previous studies [12, 68] for evaluating ROM building procedures. The beam has a length, of 228.6mm (9 in), a width of 12.7 mm (0.5 in), a thickness of 0.7874 mm (0.031 in), a modulus of elasticity of $E = 2.0684 \times 10^5$ N/mm² (2.97×10^7 lb/in²), a density of $\rho = 7.8 \times 10^{-6}$ kg/mm³ (7.36×10^{-4} lb · s²/in⁴),

and Poisson's ratio $\nu = 0.29$. The beam was modeled with 40 2-node beam elements and restrained to in-plane motion resulting in a total of 117 DOF. In this case a 2-DOF ROM is considered consisting of the modes 1 and 3 of the flat beam. The ROM contains 7 nonlinear stiffness terms per modal DOF, 3 quadratic and 4 cubic, resulting in 14 total terms.

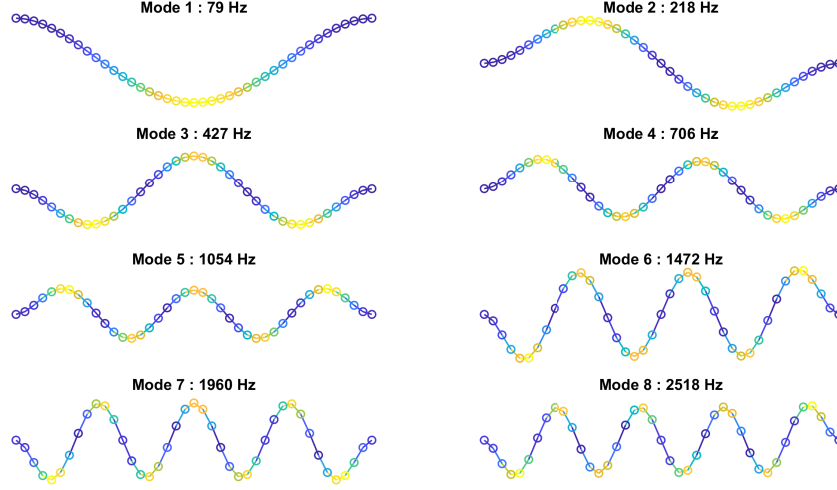


Figure 8: Linear normal modes of the flat beam. Modes 1 and 3 are used within the base set.

2.3.1 Rom Training and Nonlinear Stiffness Terms

The training data for the flat beam ROM consisted of 10 separate sets of load case data, each of which was complete in that it contained all of the typical permutations of the modal loadings [12] and thus could have been used to obtain a single ROM with the conventional approach. The load scaling values for the forces used to excite the model were created from a normal distribution with a mean of $\mu = 0.5 \times \text{thk}$ and $\sigma = 0.05 \times \text{thk}$ where thk is the thickness of the beam (0.031 in). The cross-validation training results for the ROMs are presented in Figure 9. The MSE is plotted as a function of the regularization parameter. In

both cases it was found that the optimal penalty term and corresponding number of terms, per modal DOF, was found to be 4 corresponding to the cubic terms of the model. The actual decrease in MSE relative to the LS solution is less than 1% in both cases. The nonlinear stiffness coefficients of the 2-DOF ROM identified via LASSO are presented in Figure 10. In each plot the nonlinear stiffness coefficients are normalized to the values identified using least squares regression. For the first modal equation, the terms that are removed first are the the quadratic ones. Following that, the $\beta_{1,1,2}$ is removed but shortly after comes back into the solution as $\beta_{2,2,1}$ is removed. Then at a value of $\lambda = 3.28$ the only term to remain is the $\beta_{1,1,1}$ term. The sparse predictor models created via LASSO for the first modal equation correspond well with what is known about the beam. The first being that quadratic terms are negligible and that the most important term is the $B_{1,1,1}$ parameter. For the second modal equation the same trend is found with regards to the quadratic terms being removed early on and again the last term remain within the predictor model, is the cubic value associated with the second modal terms $\beta_{2,2,2}$.

2.3.2 Dynamic Accuracy Evaluation

To evaluate the accuracy of the ROMs created using LASSO the models were compared with the least squares model. The metric used to compare the numerical models are NNMs which were introduced in Section 1.3 and will be discussed in more detail in Section 3. The NNMs serve as a strong metric to define nonlinear dynamical systems [68, 26]. The nonlinear normal modes define the amplitude-frequency dependence of a nonlinear system. The first two NNMs, represented as frequency energy plots (FEPs) of the numerical models are plotted in Figure 11. The NNMs were computed using the Multi-Harmonic Balance (MHB) method

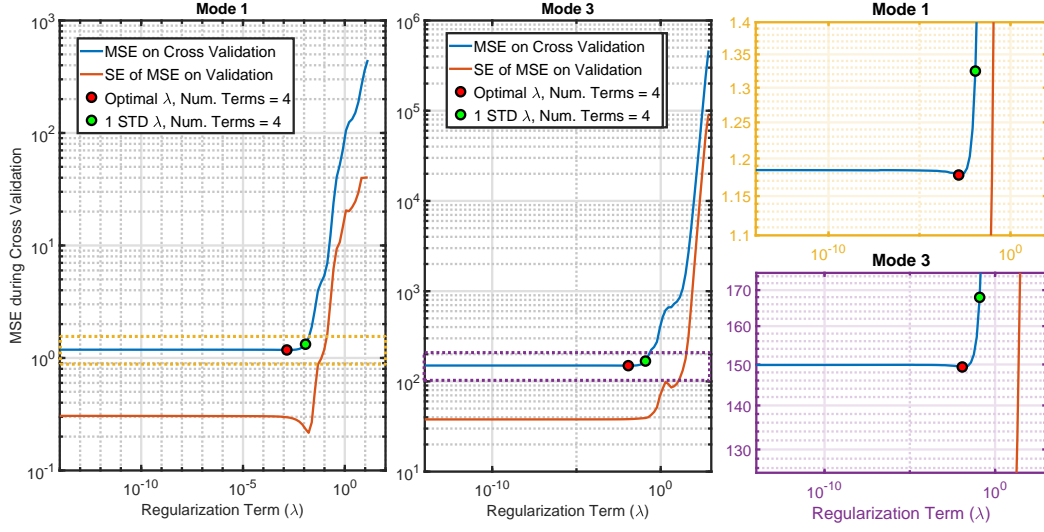


Figure 9: Mean squared error (MSE) and standard error (SE) of 1,3 Mode ROM when using k-Fold cross validation for each λ value. The two subplots on the right are zoomed in portions of the the plots on the left and center.

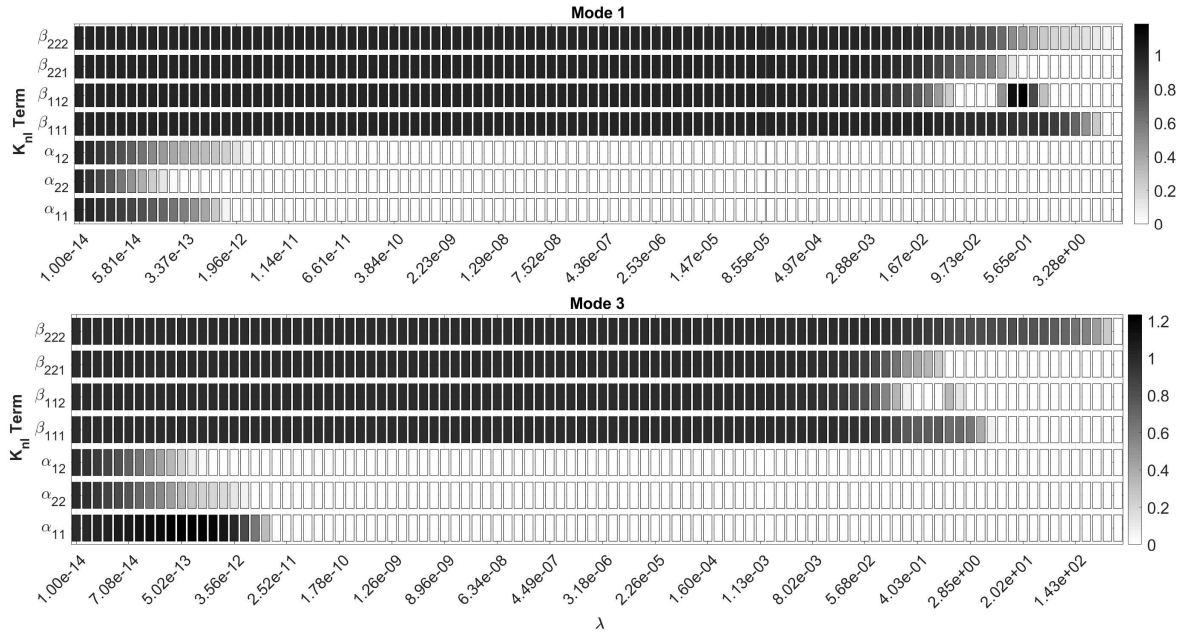


Figure 10: Nonlinear stiffness coefficients of the 1st and 3rd modal equations versus the LASSO regularization parameter λ . The nonlinear stiffness coefficients are normalized with respect to the values estimated from least squares estimation.

with 3 harmonics included within the solution for the ROMs based on [53]. The plot on the left represents the 1st NNM of the flat beam and the plot on the right represents the 3rd NNM.

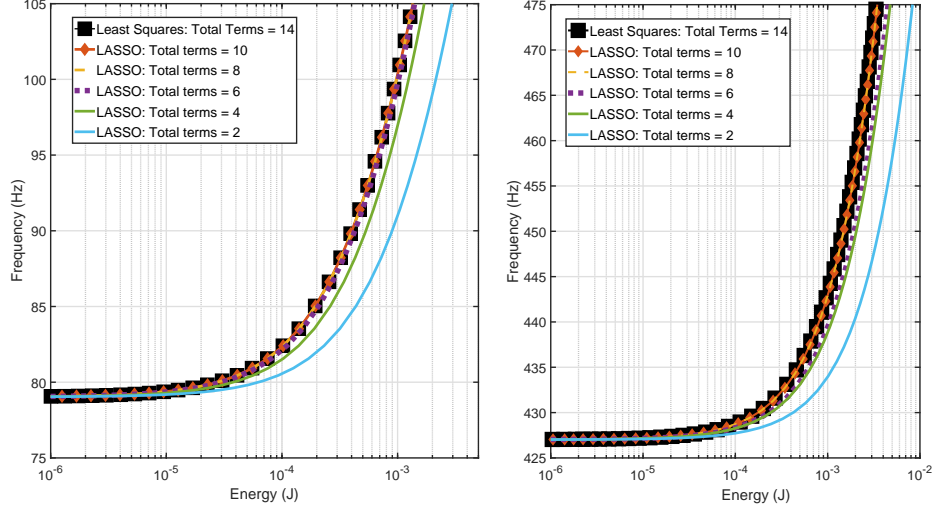


Figure 11: Frequency energy plot of the 1st and 3rd NNM of the flat beam for ROMs creating using least squares and using lasso with various penalty terms.

The ROMs made using LASSO were comparable with the NNM computed from the LS ROM. The LASSO ROMs remained accurate compared to the LS ROM for the 1st NNM when it was reduced down to 6 terms, a (0.43%) sparsity value. For the 2nd NNM the LASSO ROMs maintained accuracy when reduced down to 8 nonlinear stiffness terms (0.57%) sparsity value. After less than 8 terms were retained within the ROM the NNM starts to lose accuracy. This is expected because from Figure 9 the MSE during cross-validation increases after removing more than optimal number of terms, 3 per modal DOF resulting in 6 total removed. This simple example has shown that LASSO with cross-validation can identify those terms in a simple ROM that are most important, and that it produces results that agree with our expectations based on the physics of the problem. The next section

tackles a more challenging problem.

2.4 Curved Panel

The second numerical study is on a curved panel, originally presented in [69] and also studied in [12]. The panel is 247.65 mm (9.75 in) by 400.05 mm (15.75) in along the curved direction which has a radius of curvature of 2540 mm (100 in). The panel has fixed boundary conditions along all sides. The finite element of the panel is shown in Figure 12 consisting of 63 elements along the curved direction and 24 along the flat direction. The panel is made of stainless steel with a modulus of elasticity of $E = 204.8 GPa$ ($28,500 ksi$), poisson's ratio of $\nu = 0.3$, and a density of $\rho = 7,870 kg / m^3$ ($7.48 \times 10^{-4} lb \cdot s^2 / in^4$).

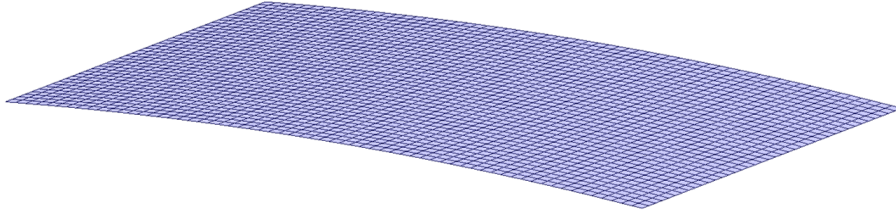


Figure 12: Finite element model of the curved panel.

Based on insights in previous work [12] the panel requires a significant number of the symmetric bending modes within the basis set in order to accurately capture the response of the structure to a uniform excitation of the system. The basis set for largest reduced order model used in this work for this structure consists of the modes (1, 2, 3, 4, 5, 8, 10), seven modes in total. The linear modes of the structure used within the basis set are presented in Figure 13. This 7 mode ROM will be used in the evaluation of accuracy section to follow but due to the size of the ROM (112 stiffness terms per modal DOF resulting in 784 nonlinear

stiffness terms total) it is difficult to portray the nonlinear stiffness terms and training results as was done in the previous section. For each ROM made, the load cases consisted of 10 observations of loading such that each case contains enough information to generate a single ROM. The scaling factors of each of the 10 observations were again sampled from a normal distribution with a mean of 1x the plate's thickness and a standard deviation of 0.1x the thickness. Before showing those results, a 4-mode ROM consisting of modes (1, 2, 3, 4) will be used to demonstrate the training and nonlinear stiffness parameter identification.

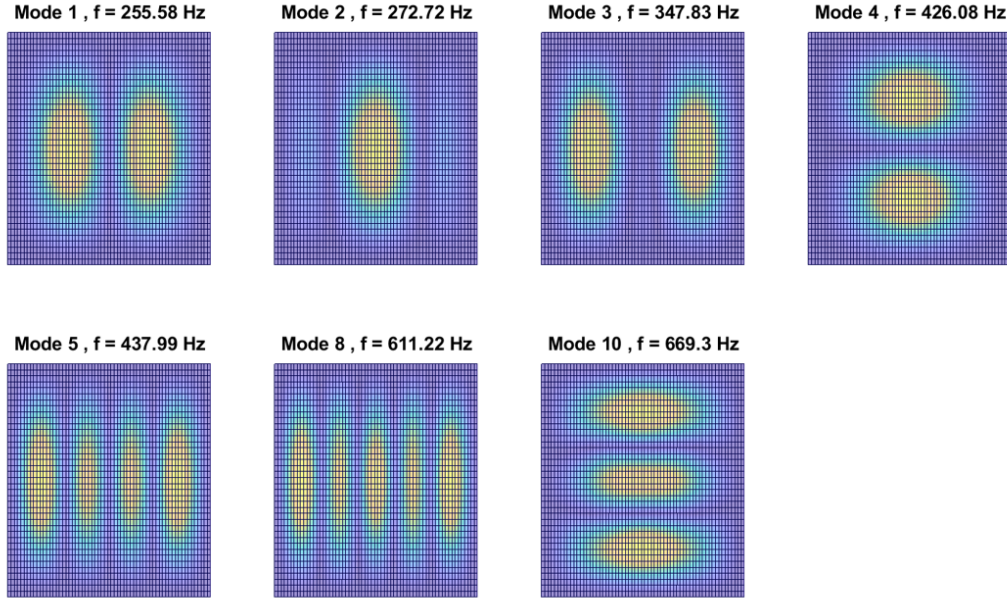


Figure 13: Linear mode shapes included within the basis set for the ROM used in this study.

2.4.1 Training and Nonlinear Stiffness Identification

The cross-validation results when generating the a 4-mode ROM are presented in Figure 14 for each mode included within the ROM. The MSE of the k-Fold cross validation is presented

along with the standard error (SE) of the MSE for each value of λ . Furthermore, the optimal lambda is presented for each case. For each case the MSE is relatively constant from low values of lambda, corresponding to near least squares solutions, up until the optimal values for each mode. For modes 1, 3 and 4 the optimal λ values were near 1. For mode 2, the primary bending mode, the optimal λ corresponded to a $\lambda = 0$ or a least squares solution. For modes 1, 3 and 4 the optimal regularization coefficient occurs right before significant error in the model is present, as too many coefficients are removed.

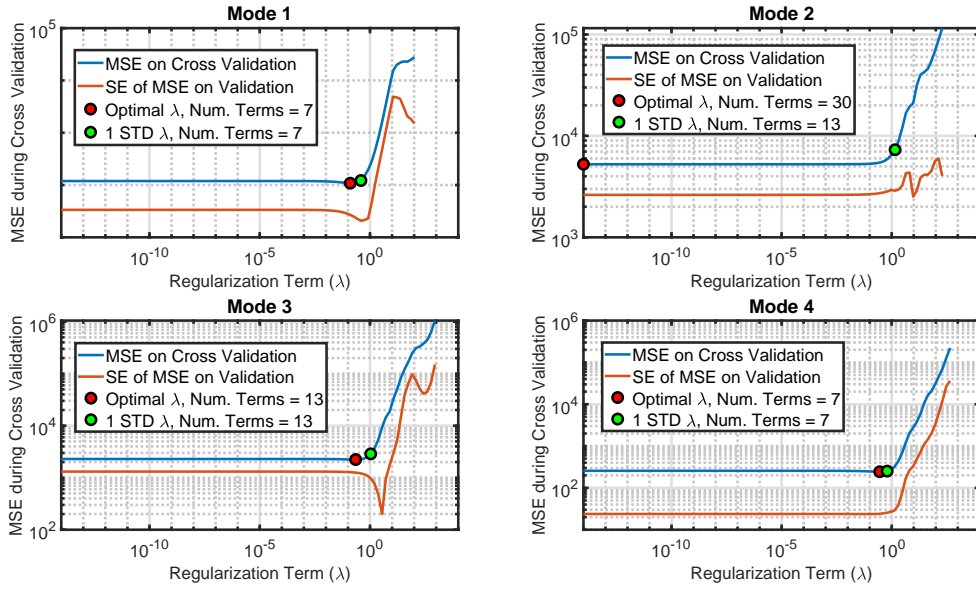


Figure 14: Mean squared error (MSE) and standard error (SE) of k-Fold cross validation for each λ value.

Three sparsity plots are shown in Figure 15, showing the terms that would be retained and their relative magnitudes for three cases: 1.) The Least Squares solution (all terms retained), 2.) the optimal solution identified via cross-validation, and 3.) a solution in which terms with the smallest magnitude are removed. The later is used to demonstrate that lasso does not simply remove the lowest magnitude prediction variables; the magnitude

selection procedure removes different parameters from the model than the LASSO does, and furthermore, if one were to perform a procedure in this manner, the parameters that are retained in the model would not be changed from the initial LS estimate and may not be optimal.

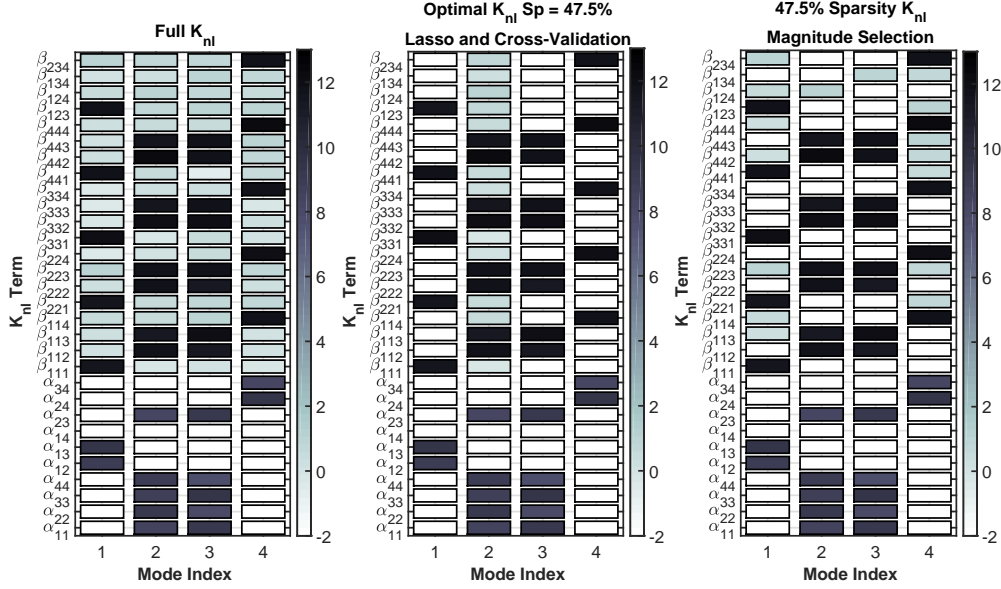


Figure 15: Nonlinear stiffness coefficient matrices for three different sets of sparsity approaches 1.) The Least Squares solution (all terms shown would be retained), 2.) the optimal solution identified via cross-validation (terms in white are eliminated), and 3.) a solution in which terms with the smallest magnitude are removed (terms in white are eliminated).

The same procedure was applied to ROMs from single mode up to the 7 mode ROM with modes (1,2,3,4,5,8,10) as described earlier, and the resulting sparsities for the optimal model and 1-standard deviation error models are presented in Figure 16. The sparsity parameter, S_p , is the ratio of non-zero coefficients retained in the model to the number of total coefficients of the LS model. In each case the LASSO procedure identifies an optimal model, in terms of MSE during cross-validation, that is sparse. In many of the cases the $1 - \sigma$ error model produces a similar sparsity model as the optimal.

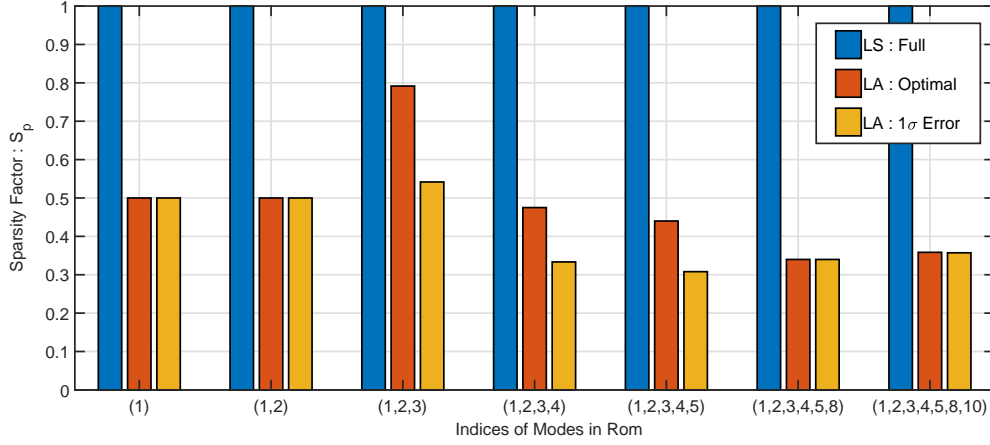


Figure 16: Bar plot depicting the sparsity factors for various orders of ROMs .

2.4.2 Dynamic Accuracy Evaluation

For this structure the dynamic accuracy was evaluated by computing NNMs of the ROM using the multi-harmonic balance method [53], projecting the response to the physical domain via the basis set to obtain an initial displacement, \mathbf{x}_0 , and integrating the response over one period. The accuracy is then determined by the periodicity of the response, which takes the form

$$\epsilon = \frac{||\mathbf{x}_T - \mathbf{x}_0||}{||\mathbf{x}_0||} \quad (24)$$

where \mathbf{x}_T is the displacement at the end of the integration over the period. This metric provides a measure of how well the NNM of the ROMs capture the true NNM of the full FE model. The first two nonlinear normal modes of the curved panel are presented in Figure 17 in subplots (a) and (b) respectively. For both NNMs there is little discrepancy between the curves for each of the numerical models.

The displacements along the NNM at the points described in subplot(b) of Figure 17 for

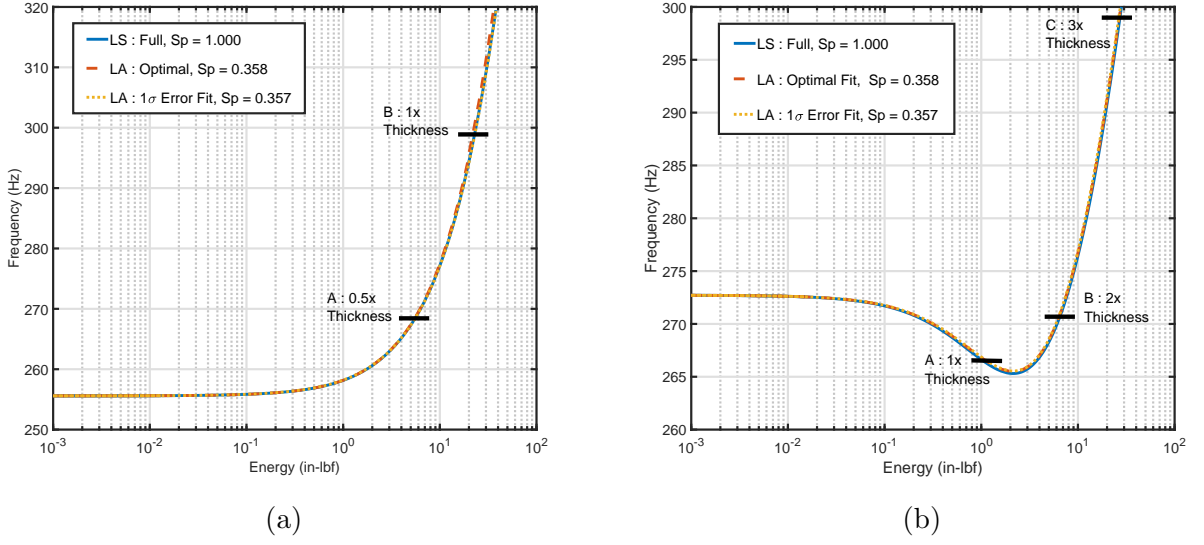


Figure 17: Nonlinear normal modes of the curved panel computed from ROM with Modes (1,2,3,4,5,8,10) included within the basis set. Subplot (a) NNM of first mode. Subplot(b) NNM of the second mode. NNMs were computed using the MHB method with 5 harmonics included.

each model are presented Figure 18. The displacement fields, although they look similar, contain slight differences that have a strong influence on the accuracy of the NNM solution and thus the validity of the ROM.

The periodicity results for the points designated in Figure 17 for the 2nd NNM are presented in Table 2 for each model. Additionally the periodicity values from a model using a single set of load cases is presented to compare with previous ROM building approaches. The LS model performs better than the LASSO models at all three points B and C along the NNM. The LASSO model with optimal MSE, at a sparsity value of 0.358, is slightly more inaccurate than the LS model at points A and B. The $1 - \sigma$ model has considerably larger error than the other two. At point C, where the maximum response amplitude is 3x the thickness of the structure, all the models become somewhat inaccurate. The NA in at point C for the LS model generated with only 1x thickness is because the NNM did not compute

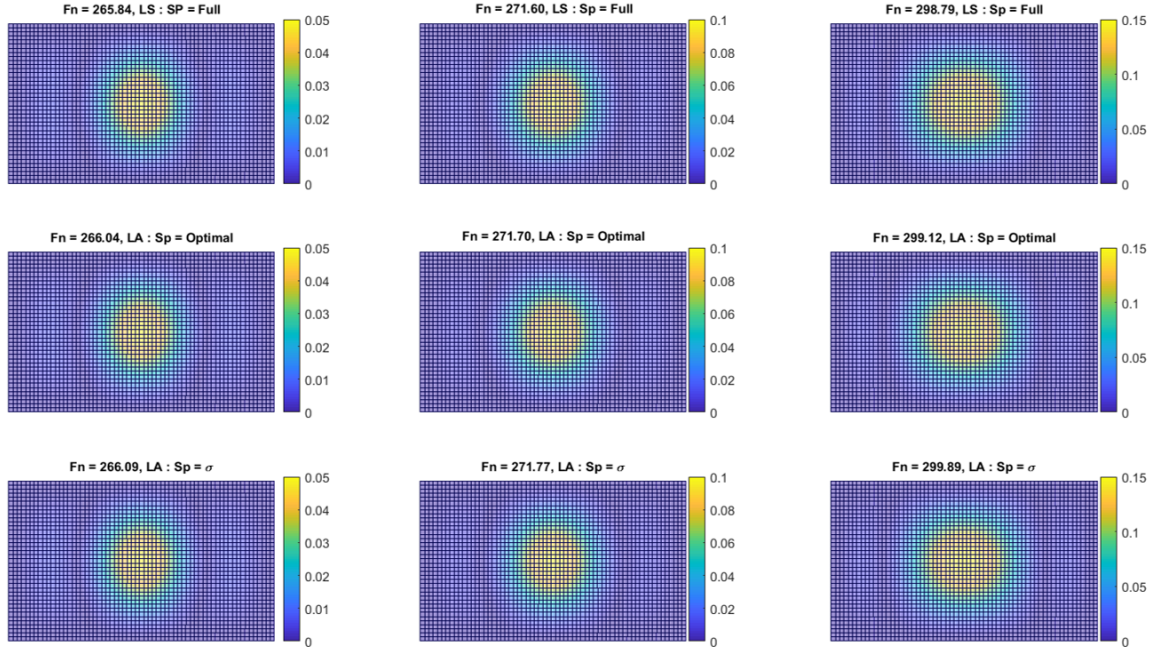


Figure 18: Full FE model displacements at the NNM solutions designated in Figure 17 for each model.

Table 2: Periodicity values, ϵ as defined in Eq 24, for the NNM solutions presented in subplot (b) of Figure 17.

Point	A	B	C
LS : All Load Cases	0.0059	0.0070	0.0463
LS : Single Load 1xThk	0.0079	0.0191	NA
LA : All Load Cases - Optimal	0.0063	0.0075	0.0513
LA : All Load Cases - 1σ error	0.0093	0.0108	0.1074

up to that high of a deformation.

In this case study the number of terms in the 7-DOF ROM was able to be reduced down to only 35.8% of the original parameters with negligible loss in accuracy of the NNM prediction.

2.5 Recap

The use of LASSO is able to produce ROMs with significantly less parameters than that of the original ROM as detailed in the numerical case studies with reductions as much as 66% without noticeable loss of accuracy. In the context of nonlinear model updating for ROMs this can greatly reduce the number of free variables included within the optimization routines used to update the models. This is especially true in the case in which finite difference routines are required to compute sensitivities as it requires many additional function evaluation which slows the model updating procedure.

3 Nonlinear Modal Analysis

3.1 Introduction

This section discusses the identification of periodic orbits of a nonlinear system, in particular systems with geometric nonlinearity. There are a multitude of methods available to compute periodic orbits, including analytical perturbation techniques [70, 71], shooting methods [72, 55], and discretization approaches. The two most popular approaches for structural dynamics of complex and realistic structures are shooting methods and the harmonic balance method. Shooting methods look to identify the periodic orbit of the nonlinear system by solving a two-point boundary value problem, including the period of oscillation and the state variables; displacement and velocity [26, 72]. The harmonic balance method is a discretization approach in which the response is projected onto a finite Fourier basis set resulting in a nonlinear algebraic system of equations to be solved.

Original works on this research topic used the shooting method described in [72] to compute the periodic orbits of the structures of interest [73]. Two main disadvantages were noted (1) the computational expense of computing the periodic orbits and (2) the occurrence of internal resonances that halted the continuation routine. For low-order systems the computational cost is fairly limited, but as the system size approaches even 5 or 10 DOF, the method becomes computationally inefficient. Furthermore, since the shooting method implicitly contains all of the harmonics of the system the continuation routine tends to deviate onto internal resonances, and typically manual control is required to remain on the main branch. These drawbacks makes it difficult to include within an automated updating routine that must compute many NNMs without manual control.

Due to the computational setbacks of the shooting method, the harmonic balance method was sought to compute the periodic orbits of the systems. The advantage of the harmonic balance method is that it has a significantly lower computational cost, gradients are known in a closed form and it has the ability to filter internal resonances [61]. The drawback of the method is that the accuracy is dependent on the number of Fourier terms retained within the basis set.

3.2 Harmonic Balance Method

The harmonic balance method is a powerful tool used across many disciplines including electrical engineering for analyzing nonlinear circuits [74], fluid dynamics for analyzing periodic flows [75], and structural dynamics for nonlinear vibration problems. Krylov and Bogliubov [76] were the first to coin the term "harmonic balance" in their book where they

linearized a nonlinear system. There are many variants on the HB method including the classical HB [77], incremental harmonic balance method (IHB) [78, 79, 80], multi-harmonic balance (MHB), higher-dimensional multi-harmonic balance (HDMHB) [81, 82], stochastic multi-harmonic balance (STMHB) [83]. In particular this work utilizes the multi-harmonic balance method, in which higher order harmonics are able to be included within the solution versus the conventional harmonic balance which only retains the fundamental harmonic terms.

3.2.1 Frequency Domain Formulation

The periodic motion of the original equation in the time domain can be solved efficiently by representing the response as a Fourier series and solving the resulting nonlinear algebraic equation. The derivation will be presented for physical system modeled by the FE method, the method applies in the same manner to a ROM. The setup of the MHB method in this work will follow similarly to that of [52]. Assuming that the response, $\mathbf{x}(t)$, and the combination of external and nonlinear force, $\mathbf{f}(\omega, t, \mathbf{x}) = \mathbf{f}_{ext}(\omega, t) - \mathbf{f}_{nl}(\mathbf{x})$, are periodic, they can be represented as a sum of Fourier coefficients truncated to the N_H^{th} harmonic as

$$\mathbf{x}(t) = \mathbf{z}_0 + \sum_{h=1}^{N_H} \left(\mathbf{z}_s^{(h)} \sin\left(\frac{h\omega t}{\nu}\right) + \mathbf{z}_c^{(h)} \cos\left(\frac{h\omega t}{\nu}\right) \right) \quad (25)$$

$$\mathbf{f}(t) = \mathbf{F}_0 + \sum_{h=1}^{N_H} \left(\mathbf{F}_s^{(h)} \sin\left(\frac{h\omega t}{\nu}\right) + \mathbf{F}_c^{(h)} \cos\left(\frac{h\omega t}{\nu}\right) \right) \quad (26)$$

where ω is the frequency of oscillation, h is the order of the harmonic, and ν is the subharmonic multiplier. Typically ν is used to represent subharmonic resonance for an excited

system, in this work ν was set to 1. The new state variables of the system are represented as a vector of Fourier coefficients

$$\mathbf{z} = \left[(\mathbf{z}_0)^T \ (\mathbf{z}_s^1)^T \ (\mathbf{z}_c^1)^T \ (\mathbf{z}_s^2)^T \ (\mathbf{z}_c^2)^T \ \dots \ (\mathbf{z}_s^{N_H})^T \ (\mathbf{z}_c^{N_H})^T \right]^T \quad (27)$$

$$\mathbf{F} = \left[(\mathbf{F}_0)^T \ (\mathbf{F}_s^1)^T \ (\mathbf{F}_c^1)^T \ (\mathbf{F}_s^2)^T \ (\mathbf{F}_c^2)^T \ \dots \ (\mathbf{F}_s^{N_H})^T \ (\mathbf{F}_c^{N_H})^T \right]^T \quad (28)$$

where the subscripts c and s refer to cosine and sine terms of the Fourier coefficients respectively. The transformation from the frequency domain to the time domain shown in Eq (25) and Eq (26), can be represented in matrix form as

$$\mathbf{x}(t) = (\mathbf{Q}(t) \otimes \mathbf{I}_n) \mathbf{z} \quad (29)$$

$$\mathbf{f}(t) = (\mathbf{Q}(t) \otimes \mathbf{I}_n) \mathbf{F} \quad (30)$$

where \mathbf{I}_n is a $n \times n$ identity matrix and $\mathbf{Q}(t)$ has the form

$$\mathbf{Q}(t) = \begin{bmatrix} 1 & \sin\left(\frac{\omega t}{\nu}\right) & \cos\left(\frac{\omega t}{\nu}\right) & \dots & \sin\left(N_H \frac{\omega t}{\nu}\right) & \cos\left(N_H \frac{\omega t}{\nu}\right) \end{bmatrix} \quad (31)$$

The velocity and acceleration terms in Eq (1) can be represented as

$$\dot{\mathbf{x}}(t) = \left(\dot{\mathbf{Q}}(t) \otimes \mathbf{I}_n \right) \mathbf{z} = (\mathbf{Q}(t) \nabla \otimes \mathbf{I}_n) \mathbf{z} \quad (32)$$

$$\ddot{\mathbf{x}}(t) = \left(\ddot{\mathbf{Q}}(t) \otimes \mathbf{I}_n \right) \mathbf{z} = (\mathbf{Q}(t) \nabla^2 \otimes \mathbf{I}_n) \mathbf{z} \quad (33)$$

where ∇ and ∇^2 represent the first and second gradients respectively of the frequency transformation with respect to the current frequency, and are given as

$$\nabla = \begin{bmatrix} 0 & & & & \\ & \ddots & & & \\ & & \nabla_h & & \\ & & & \ddots & \\ & & & & \nabla_{N_H} \end{bmatrix} \quad (34)$$

$$\nabla^2 = \begin{bmatrix} 0 & & & & \\ & \ddots & & & \\ & & \nabla_h^2 & & \\ & & & \ddots & \\ & & & & \nabla_{N_H}^2 \end{bmatrix} \quad (35)$$

with each individual term having the form

$$\nabla_h = \begin{bmatrix} 0 & -(h\frac{\omega}{\nu}) \\ (h\frac{\omega}{\nu}) & 0 \end{bmatrix} \quad (36)$$

$$\nabla_h^2 = \begin{bmatrix} -(h\frac{\omega}{\nu})^2 & 0 \\ 0 & -(h\frac{\omega}{\nu})^2 \end{bmatrix} \quad (37)$$

Inserting the equations (29-30) and (32-33) into Eq (1) and performing the algebraic operations described in [52] the time dependent harmonic balance equation becomes

$$((\mathbf{Q}(t)\nabla^2) \otimes \mathbf{M}) \mathbf{z} + ((\mathbf{Q}(t)\nabla) \otimes \mathbf{C}) \mathbf{z} + (\mathbf{Q}(t) \otimes \mathbf{K}) \mathbf{z} = (\mathbf{Q}(t) \otimes \mathbf{I}_n) \mathbf{F} \quad (38)$$

To remove the time dependency in Eq (38) a Galerkin approach is used to project the system onto the trigonometric basis defined by Eq (31). This is done by premultiplying each term in Eq (38) by $\frac{2}{T} \int_0^T \mathbf{Q}(t) dt$ and integrating over the period that results in

$$(\nabla^2 \otimes \mathbf{M}) \mathbf{z} + (\nabla \otimes \mathbf{C}) \mathbf{z} + (\mathbf{I}_{(2N_H+1)} \otimes \mathbf{K}) \mathbf{z} = \mathbf{F} \quad (39)$$

or in a more compact form and including the dependence on the Fourier coefficients

$$\mathbf{h}(\mathbf{z}, \omega) = \mathbf{A}(\omega)\mathbf{z} - \mathbf{F}(\mathbf{z}) = \mathbf{0} \quad (40)$$

in which the linear dynamics are contained within the term, $\mathbf{A}(\omega)$

$$\mathbf{A}(\omega) = \nabla^2 \otimes \mathbf{M} + \nabla \otimes \mathbf{C} + \mathbf{I}_{(2\mathbf{N}_H+1)} \otimes \mathbf{K} \quad (41)$$

and the nonlinear term , $\mathbf{F}(\mathbf{z})$, is presented in the next section.

3.2.2 Determination of Nonlinear Terms and Derivatives

The final harmonic balance equation presented in Eq (40) is nonlinear and so an iterative scheme must be used to solve it; in this work the Newton-Rhapson procedure will be used, and so the gradient with respect to the state variables, ω and \mathbf{z} is required. The gradients with respect to frequency have a simple form by taking the derivative with respect to the linear dynamic matrix presented in Eq (41) which is a function of ∇_h^2 and ∇_h such that

$$\frac{\partial \nabla_h}{\partial \omega} = \nabla_h = \begin{bmatrix} 0 & -\frac{h}{\nu} \\ \frac{h}{\nu} & 0 \end{bmatrix} \quad (42) \quad \frac{\partial \nabla_h^2}{\partial \omega} = \begin{bmatrix} -2h^2 \frac{\omega}{\nu^2} & 0 \\ 0 & -2h^2 \frac{\omega}{\nu^2} \end{bmatrix} \quad (43)$$

in which the resulting gradient of the linear dynamic matrix becomes

$$\frac{\partial \mathbf{h}}{\partial \omega} = \frac{\partial \mathbf{A}(\omega)}{\partial \omega} \mathbf{z} = \left(\frac{\partial \nabla^2}{\partial \omega} \otimes \mathbf{M} + \frac{\partial \nabla}{\partial \omega} \otimes \mathbf{C} \right) \mathbf{z} \quad (44)$$

The evaluation of the nonlinear terms and gradients have a more complex form. For low order systems, with only a few harmonics closed form expressions for the nonlinear terms can be obtained, but for multi-DOF systems this process becomes cumbersome. An alternative, originally developed by [84] termed the alternating frequency/time-domain (AFT), could be used to evaluate the nonlinearities in the frequency domain. The method relies on taking inverse FFTs and FFTs of data to switch between the time and frequency domain to evaluate $\mathbf{F}(\mathbf{z})$ and compute the Jacobian via finite differences. This approach comes with computational overhead and the possible introduction of errors due to the step size used in the finite difference method.

Instead of using the AFT approach based on FFT transformations, the AFT can be formulated as a set of linear operations in which the inverse Fourier transformation can be represented as a matrix operator $\Gamma(\omega)$. This method was first introduced by [85] and then later implemented into the harmonic balance formulation in [86]. The truncated inverse Fourier transformation in matrix form can be represented as

$$\tilde{\mathbf{x}} = \Gamma(\omega)\mathbf{z} \tag{45}$$

which, upon expanding, can be written as the following $nN \times (2N_H + 1)n$ sparse matrix.

$$\mathbf{\Gamma}(\omega) = \begin{bmatrix} \mathbf{I}_n \otimes \begin{bmatrix} 1 \\ 1 \\ \vdots \\ 1 \end{bmatrix} & \mathbf{I}_n \otimes \begin{bmatrix} \sin\left(\frac{\omega t_1}{\nu}\right) \\ \sin\left(\frac{\omega t_2}{\nu}\right) \\ \vdots \\ \sin\left(\frac{\omega t_N}{\nu}\right) \end{bmatrix} & \mathbf{I}_n \otimes \begin{bmatrix} \cos\left(\frac{\omega t_1}{\nu}\right) \\ \cos\left(\frac{\omega t_2}{\nu}\right) \\ \vdots \\ \cos\left(\frac{\omega t_N}{\nu}\right) \end{bmatrix} & \dots \\ \mathbf{I}_n \otimes \begin{bmatrix} \sin\left(N_H \frac{\omega t_1}{\nu}\right) \\ \sin\left(N_H \frac{\omega t_2}{\nu}\right) \\ \vdots \\ \sin\left(N_H \frac{\omega t_N}{\nu}\right) \end{bmatrix} & \mathbf{I}_n \otimes \begin{bmatrix} \cos\left(N_H \frac{\omega t_1}{\nu}\right) \\ \cos\left(N_H \frac{\omega t_2}{\nu}\right) \\ \vdots \\ \cos\left(N_H \frac{\omega t_N}{\nu}\right) \end{bmatrix} & & \end{bmatrix} \quad (46)$$

where N is the number of time samples used to discretize the periodic response. The displacement time series vector in Eq (45) has the following form

$$\tilde{\mathbf{x}} = \begin{bmatrix} \mathbf{x}_1(t_0) & \dots & \mathbf{x}_1(t_N) & \mathbf{x}_2(t_0) & \dots & \mathbf{x}_n(t_N) \end{bmatrix} \quad (47)$$

in which the subscript denotes the specific DOF of the system. To transform the time series data back to the frequency domain, the direct Fourier transformation is needed. This is obtained by computing the Moore-Penrose pseudo inverse

$$\mathbf{\Gamma}^+ = \mathbf{\Gamma}^T (\mathbf{\Gamma} \mathbf{\Gamma}^T)^{-1} \quad (48)$$

The Fourier coefficients of the external and nonlinear force, $\mathbf{f}(t, \omega, \mathbf{x})$, with dependence on t , ω and \mathbf{x} assumed can be computed using

$$\mathbf{F}(z) = \mathbf{\Gamma}(\omega)^+ \tilde{\mathbf{f}} \quad (49)$$

where the force vector, has the same format as Eq (47) resulting in

$$\tilde{\mathbf{f}} = \begin{bmatrix} \mathbf{f}_1(t_0) & \cdots & \mathbf{f}_1(t_N) & \mathbf{f}_2(t_0) & \cdots & \mathbf{f}_n(t_N) \end{bmatrix} \quad (50)$$

Similarly, the Fourier coefficients of the response $\mathbf{x}(t)$ are

$$\mathbf{z} = \mathbf{\Gamma}(\omega)^+ \tilde{\mathbf{x}} \quad (51)$$

The Jacobian of the harmonic balance equation with respect to the Fourier coefficients was found analytically in [87] as

$$\mathbf{h}_{\mathbf{z}} = \frac{\partial \mathbf{h}}{\partial \mathbf{z}} = \mathbf{A} - \frac{\partial \mathbf{F}}{\partial \mathbf{z}} = \frac{\partial \mathbf{F}}{\partial \tilde{\mathbf{f}}} \frac{\partial \tilde{\mathbf{f}}}{\partial \tilde{\mathbf{x}}} \frac{\partial \tilde{\mathbf{x}}}{\partial \mathbf{z}} = \mathbf{A} - \mathbf{\Gamma}^+ \frac{\partial \tilde{\mathbf{f}}}{\partial \tilde{\mathbf{x}}} \mathbf{\Gamma} \quad (52)$$

Now that the gradients with respect to frequency and Fourier coefficients have been formulated they can be used to minimize Eq (40). Solving the system of algebraic equations representing the harmonic balance procedure only yields a single periodic solution of the system. To obtain a branch of solutions the MHB is coupled with a continuation routine to be discussed in the next section.

3.3 Continuation Routine

The harmonic balance method is aimed at computing a single periodic orbit at a time. To be useful for model correlation, multiple solutions must be computed to evaluate the system over multiple amplitudes. In this work, numerical continuation is used to identify the branches of periodic orbits. Numerical continuation has a well established history, first being presented

by Riks [34] in which it was used to identify unstable static equilibriums paths for structures undergoing snap-through. Since then the method has been expanded to a wide range of other problems from bifurcation tracking, nonlinear frequency response curves, nonlinear normal modes, and others. A large class of numerical continuation routines consists of predictor-corrector (PC) methods. As the name implies the first step of the procedure is to predict a new solution based upon a previously known solution. The predictor is followed by the corrector step, which is used to drive the state variables to a solution.

3.3.1 Predictor Step

The prediction step uses information from the last solution $\mathbf{z}_{(j)}, \omega_{(j)}$ along with the tangent information \mathbf{t}_j , estimated from the gradients at the previous solution, to predict the next solution. The tangent operator at the j^{th} solution can be found by solving the linear system of equations

$$\mathbf{t}_j = \begin{bmatrix} \mathbf{h}_z & \mathbf{h}_\omega \\ \mathbf{t}_{(j-1)}^T \end{bmatrix}^{-1} \begin{bmatrix} \mathbf{0} \\ 1 \end{bmatrix} \quad (53)$$

The harmonic balance method is augmented with another equation, that ensures that the prediction is tangent to the current solution point. The continuation routine uses a linear predictor

$$\begin{bmatrix} \mathbf{z}_{(j+1)} \\ \omega_{(j+1)} \end{bmatrix} = \begin{bmatrix} \mathbf{z}_{(j)} \\ \omega_{(j)} \end{bmatrix} + \Delta s \mathbf{t}_{(j)} \quad (54)$$

where Δs is the step size of the prediction. The continuation routine uses an adaptive

step-size scheme based on convergence histories of the previous solution.

3.3.2 Corrector Step

The predictor step is only used to estimate where the next solution may lie. To find the state variables that satisfy the algebraic equation, a correction scheme is needed. Nearly all corrector steps consist of some gradient based approach; in this work the correction is performed using Newton's Method with Moore-Penrose corrections [88]. Newton's method requires the gradients of the system which have been presented in Section 3.2.2.

Now using the subscript $()_i$ to denote the i^{th} iteration of the correction stage, the change in variables via Newtons method is

$$\begin{bmatrix} \delta \mathbf{z}_{(i,j)} \\ \delta \omega_{(i,j)} \end{bmatrix} = \begin{bmatrix} \mathbf{h}_z(\mathbf{z}_{(i,j)}, \omega_{(i,j)}) & \mathbf{h}_\omega(\mathbf{z}_{(i,j)}, \omega_{(i,j)}) \\ & \mathbf{v}_{(j)}^T \end{bmatrix}^{-1} \begin{bmatrix} \mathbf{h}(\mathbf{z}_{(i,j)}, \omega_{(i,j)}) \\ 0 \end{bmatrix} \quad (55)$$

$$\begin{bmatrix} \delta \mathbf{t}_{\mathbf{z}(i,j)} \\ \delta \mathbf{t}_{\omega(i,j)} \end{bmatrix} = \begin{bmatrix} \mathbf{h}_z(\mathbf{z}_{(i,j)}, \omega_{(i,j)}) & \mathbf{h}_\omega(\mathbf{z}_{(i,j)}, \omega_{(i,j)}) \\ & \mathbf{t}_{(i,j)}^T \end{bmatrix}^{-1} \begin{bmatrix} \mathbf{R}_{(i)} \\ 0 \end{bmatrix} \quad (56)$$

where

$$\mathbf{R}_{(i)} = \begin{bmatrix} \mathbf{h}_z(\mathbf{z}_{(i,j)}, \omega_{(i,j)}) & \mathbf{h}_\omega(\mathbf{z}_{(i,j)}, \omega_{(i,j)}) \end{bmatrix} \mathbf{h}_{(i)} \quad (57)$$

The state variables are updated as

$$\begin{bmatrix} \mathbf{z}_{(i+1,j)} \\ \omega_{(i+1,j)} \end{bmatrix} = \begin{bmatrix} \mathbf{z}_{(i)} \\ \omega_{(i)} \end{bmatrix} - \begin{bmatrix} \delta \mathbf{z}_{(i,j)} \\ \delta \omega_{(i,j)} \end{bmatrix} \quad (58)$$

and the current prediction vector is updated as

$$\begin{bmatrix} \delta \mathbf{t}_{\mathbf{z}(i+1,j)} \\ \delta \mathbf{t}_{\omega(i+1,j)} \end{bmatrix} = \begin{bmatrix} \delta \mathbf{t}_{\mathbf{z}(i,j)} \\ \delta \mathbf{t}_{\omega(i,j)} \end{bmatrix} - \begin{bmatrix} \delta \mathbf{t}_{\mathbf{z}(i,j)} \\ \delta \mathbf{t}_{\omega(i,j)} \end{bmatrix}. \quad (59)$$

The correction scheme continues until the norm residual of the harmonic balance equation is satisfied

$$||\mathbf{h}(\mathbf{z}_{(i,j)}, \omega_{(i,j)})|| < \epsilon \quad (60)$$

Once the nonlinear algebraic equation is solved, the final prediction vector during the correction stage, $\begin{bmatrix} \mathbf{t}_{\mathbf{z}(i,j)} & \mathbf{t}_{\omega(i,j)} \end{bmatrix}^T$, can be used for the next prediction step.

3.4 Nonlinear Normal Mode Formula

The harmonic balance has been previously presented for the case in which there is damping included within the system and potentially an external force. A nonlinear normal mode as defined earlier is a conservative motion for the underlying undamped-unforced nonlinear system. For a geometrically nonlinear system represented by Eq (5) this results in the following system.

$$\mathbf{M}\ddot{\mathbf{x}} + \mathbf{K}\mathbf{x} + \mathbf{f}_{nl}(\mathbf{x}) = \mathbf{0} \quad (61)$$

To use the harmonic balance method to find the periodic solutions of the Eq (61), simply set the damping, \mathbf{C} , and forcing, \mathbf{f}_{ext} , to zero in Eq (40). The resulting linear dynamics matrix becomes

$$\mathbf{A}(\omega) = \nabla^2 \otimes \mathbf{M} + \mathbf{I}_{(2N_H+1)} \otimes \mathbf{K} \quad (62)$$

and the nonlinear force in the frequency domain, $\mathbf{F}(\mathbf{z})$, is only a function of the nonlinear restoring force. The continuation of a nonlinear normal mode is typically initiated from the frequency of the underlying linear normal mode, with the initial guess for the amplitude set in the shape of the corresponding linear mode.

3.5 Application to Nonlinear Finite Element Models

3.5.1 Flat Clamped-Clamped Beam

The multi-harmonic balance method is first demonstrated on a clamped-clamped flat beam, which has been extensively studied [12, 55]. The nonlinear normal modes of the beam have been previously studied in [55] where the NNMs were computed using the Applied Modal Force (AMF) algorithm which is a shooting method approach. The beam was 9 in. (22.9 cm) long, 0.5 in. (1.3 cm) wide and 0.031 in. (0.79 mm) thick. It was constructed of structural steel with a Young's modulus of 29,700 ksi (204.8 GPa), shear modulus of 11,600 ksi (80.0 GPa) and mass density of $7.36 \times 10^4 \text{ lb} - \text{s}^2/\text{in}^4$ ($7870 \text{ kg}/\text{m}^3$). The beam was modeled with 40 two node beam elements restricted to in-plane motion resulting in a total of 246 DOF and 117 free DOF. For reference the first six linear normal modes are displayed in Figure 19 where the symmetric modes of the system correspond with the odd number modes and anti-symmetric with even mode numbers. This model is restrained to in-plane motion only.

The 1st NNM of the beam computed using the AMF algorithm and the MHB method is presented in Figure 20. The NNM has a purely hardening response, i.e. increase of

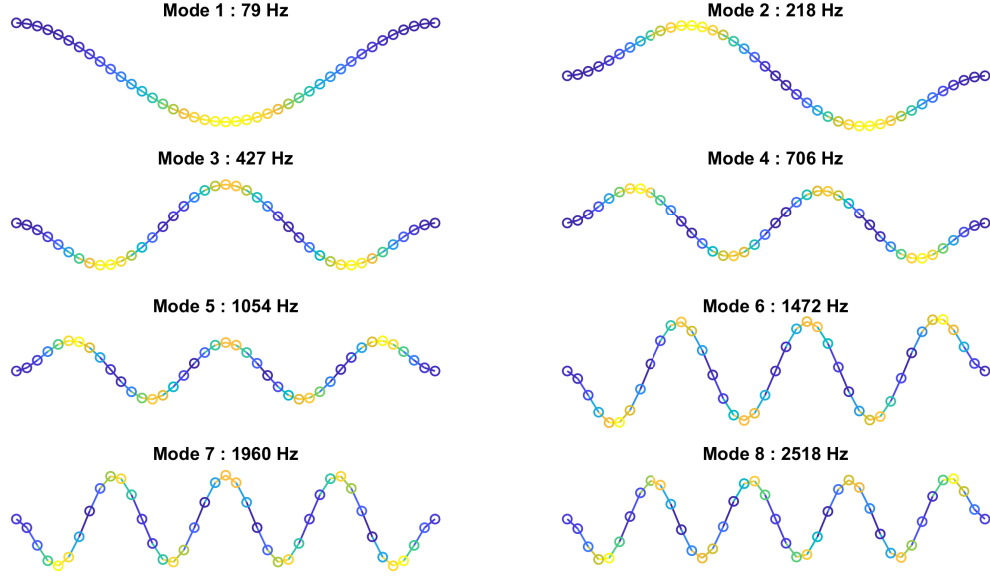


Figure 19: First six linear normal modes of a flat clamped-clamped beam

frequency with amplitude, that is depicted by all solutions. The MHB method with a single harmonic included demonstrates the same trend as the AMF results but underestimates the displacement along the curve. When including up to the 3rd harmonic within the solution the MHB and AMF solutions are indistinguishable. The solution remains accurate when the 5th harmonic is added.

A 1:5 internal resonance branch is present along the backbone at a frequency of 87 Hz. This is captured by the AMF algorithm because it implicitly contains all the harmonics of the system. The MHB method is able to predict the internal resonance as well when including 5 harmonics within the solution. The single and three harmonic solution solutions describe the backbone accurately but do not predict the internal resonance, this is an example of the filtering property of the MHB method.

The deformation at the points depicted in Figure 20 is plotted in subplot(a) of Figure 21,

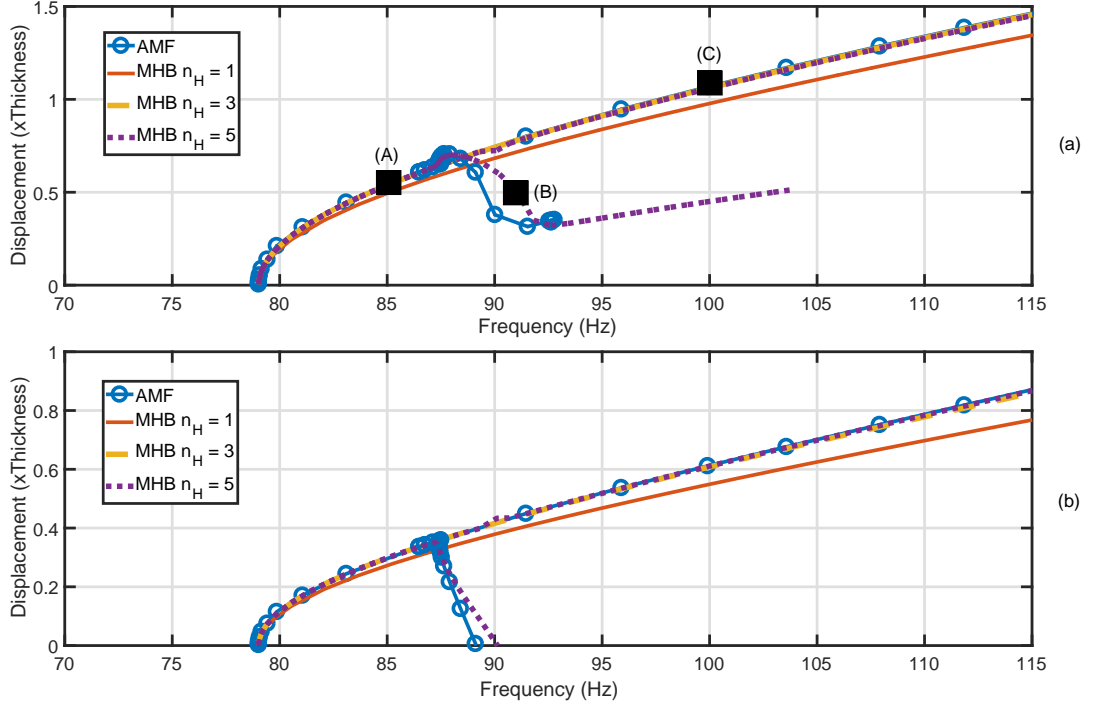


Figure 20: Comparison of Applied Modal Force algorithm from [55] with the multi harmonic balance method. Subplot (a) center node vertical displacement versus frequency. Subplot (b) quarter span node vertical displacement versus frequency.

and the modal amplitudes are shown with a bar graph in subplot(b). The modal amplitudes are found by projecting the physical displacement response onto the modal coordinates using the linear normal modes of the system. The response along the backbone is predominately in the first modal coordinate, but as the amplitude increases there is some contribution from the 3rd mode. The contribution of the 3rd mode is more noticeable along the internal resonance branch, denoted by point (B). At point (D) there starts to be slight contribution from the 5th modal coordinate although it is still orders of magnitude less than the primary mode. Neither of the anti-symmetric modes, mode 2 and mode 4, contribute to the response.

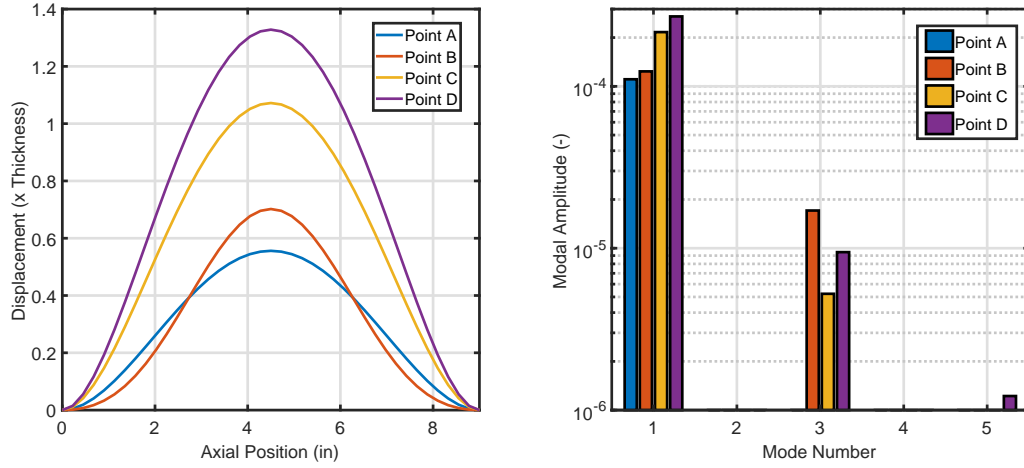


Figure 21: (a) Deformation of the beam at the points along NNM taken from Figure(20. (b) Modal amplitudes of the system taken from Figure 20.

The response across one period of oscillation of the MHB method with 5 harmonics is shown in Figure 22 for various points along the NNM branch depicted in Figure 20. These histories were found by integrating the finite element model from the initial conditions found by the harmonic balance method at those solution points. At points (A) and (C) the response is nearly all within the 1st mode of the system. At point (B), along the 1:5 internal resonance, there is a modal interaction with the 3rd NNM. This is noticeable in the physical response but can be identified more rigorously in the modal domain. In the modal coordinates the internal resonance is demonstrated by the large amplitude of mode 3 across the period with a frequency 5 times that of the fundamental harmonic.

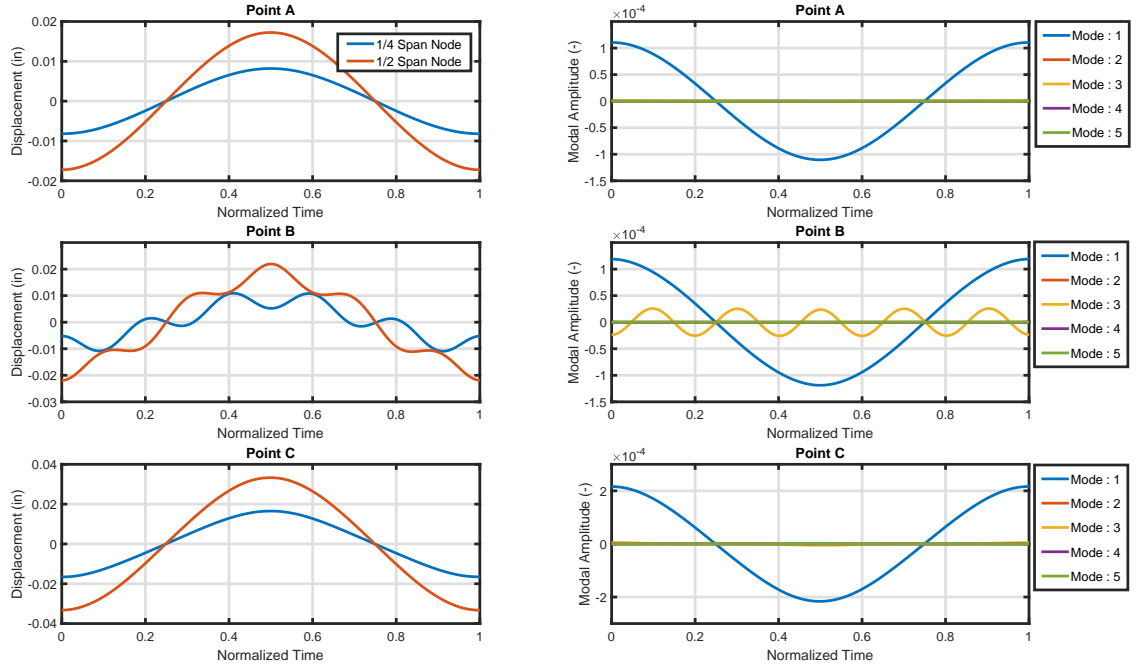


Figure 22: Dynamic response over one period of oscillation at the points along NNM taken from Figure(20). Plots on the left represent the vertical displacement of center and quarter node. Plots on the right are the modal amplitudes along the orbit.

The computational cost of using the harmonic balance method for this system is compared with that of the AMF algorithm in Table 3. It is important to mention that the FE computations of the AMF algorithm were done in Abaqus, whereas the MHB computations are all performed within Matlab. Additionally, the AMF algorithm suffers from read and write to disk overhead due to the need to communicate between Matlab and Abaqus.

Table 3: Computational time (minutes) to compute nonlinear normal mode backbone branch of the flat clamped clamped beam. Computation were done on a Intel(R) Core(TM) i7-7700K CPU @ 4.20GHz.

AMF	MHB			
	$N_H = 1$	$N_H = 3$	$N_H = 5$	$N_H = 7$
120	3.67	4.2	5.8	5.45

3.5.2 Curved Clamped-Clamped Beam

Calculating the NNMs of curved beams has been previously studied in [89, 73] and those works have shown that it can prove difficult to obtain the NNMs using a shooting method approach. The beam's geometry is presented in Figure 23 which has a radius of curvature, R , of 11430 mm (450 inches) resulting in a maximum rise, h , of 1.016 mm (0.04 inches). The beam has a slight asymmetry in the curvature to avoid the singularity that can arise when seeking to buckle a perfectly symmetric beam. The beam has a length, A , of 304.8 mm (12 in) , a width of 12.7 mm (0.5 in), a thickness of 0.508 mm (0.02 in), a modulus of elasticity of $E = 2.0684 \times 10^5 \frac{N}{mm^2}$ ($2.97 \times 10^7 \frac{lb}{in^2}$), a density of $\rho = 7.8 \times 10^{-6} \frac{kg}{mm^3}$ ($7.36 \times 10^{-4} \frac{lb \cdot s^2}{in^4}$), and Poisson's ratio $\nu = 0.29$. The beam was modeled with 400 shell elements resulting in a total of 3030 DOF. The beams are clamped on both ends as depicted in Figure 23 resulting in a total of 2970 free DOF.

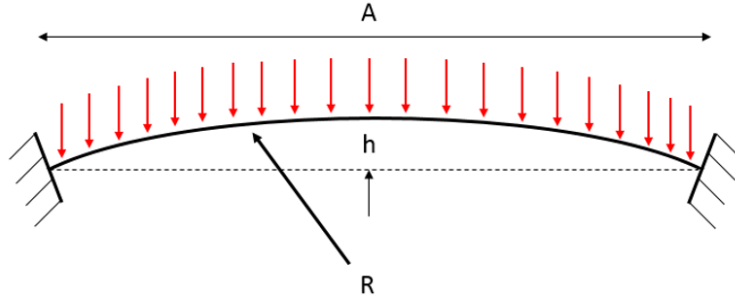


Figure 23: Geometry of curved beam.

The first four linear modes of the shallow curved beam are shown in Figure 24 for reference along with the mesh of the beam.

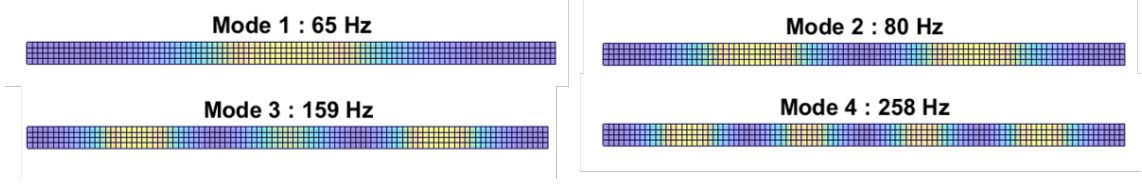


Figure 24: First four linear modes of the shallow curved beam.

The first nonlinear normal mode of the curved beam is depicted in Figure 25 for various numbers of harmonics included within the solution. All of the NNMs depict an initial softening of the system, a decrease in frequency with amplitude, followed by hardening. The single harmonic solution evolves smoothly due to its filtering property, which eliminates the prediction of any internal resonance branches. As the number of harmonics included within the solution increases, the branch becomes more difficult to compute because more internal resonance branches are identified.

All of the solutions contain similar predictions up to approximately 58 Hz, or prior to the identification of an internal resonance branch. Following the internal resonance branch the solutions with 3 or more harmonics deviate from the single harmonic during the softening. Further down the path during softening, the higher harmonic solutions deviate from each other near the turning point. As the NNM starts to harden again, the harmonic balance solutions start to coincide again near the point labeled C in Figure 25.

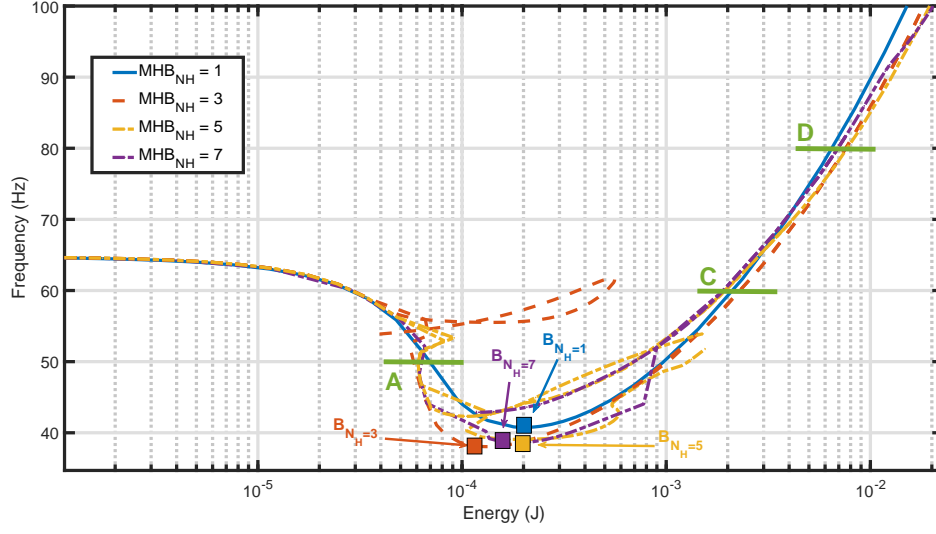


Figure 25: Nonlinear Normal Mode frequency-energy plot for the Shallow Curved Beam, computing using the harmonic balance method with varying number of harmonics. The NNM was originated from the first linear mode.

The initial displacements of the structure at each of the points marked by letters in Figure 25 are plotted in Figure 26 along with the undeformed geometry of the beam. At point A each solution has a similar deformation and a peak displacement near 1.5x the thickness of the beam. The one, three and five harmonic solutions at point B show an un-snapped state of deformation while the seven harmonic solution is snapped through. Moving to point C all the of the solutions are at the snapped state, although the shape found evolves significantly as the number of harmonics increased. This is true for point D as well.

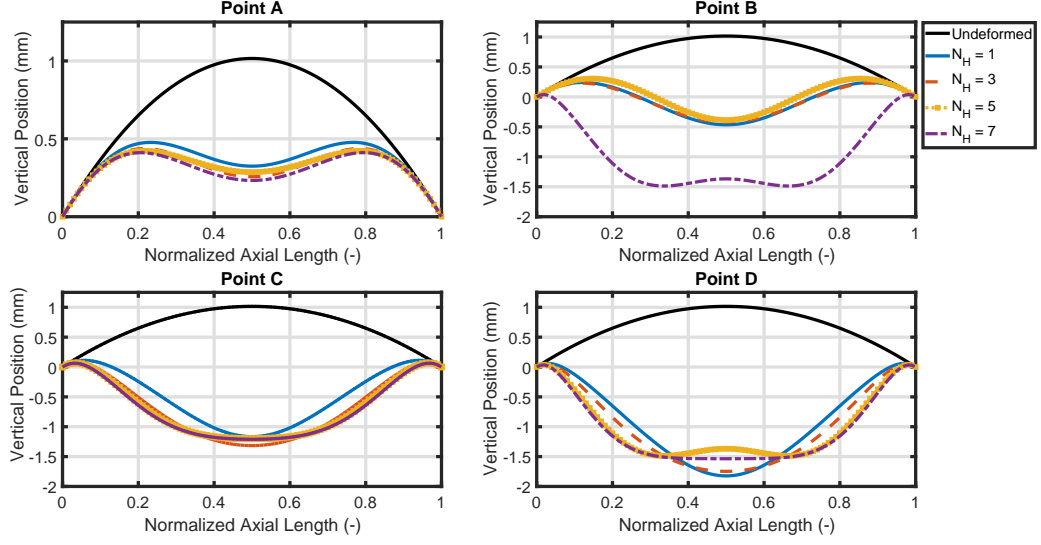


Figure 26: Initial deformation of the Shallow Curved Beam at the points along the NNM branch designated A, B, C and D in Figure 25.

To quantify these results, the accuracy of the harmonic balance solutions was evaluated at each of these points. Using the initial deformations shown in Fig. 26, the NNM solutions were integrated over the period and the periodicity, ϵ , was calculated using

$$\epsilon = \frac{\|\mathbf{x}(T) - \mathbf{x}(0)\|}{\|\mathbf{x}(0)\|} \quad (63)$$

The results are presented in Table 4. At point A, approximately a displacement of $1.5 \times$ the thickness of the beam, each of the harmonic balance solutions has a marginally periodic response with max error of 0.055 for the single harmonic model. At the turning point of the branch, the single harmonic and three harmonic solutions show considerable error. Increasing the solution to include five harmonics increases the accuracy of the solution. The five and seven harmonic solutions maintain periodicity at point C wherein the displacement reaches $4 \times$ the beam thickness at a value of 2.03 mm. Up to a displacement of approximately 2.54

mm, the five and seven harmonic solutions maintain a fairly periodic response. Interestingly, the solution with three harmonics is once again quite adequate at point D, or beyond the snap through point.

Pt	Approx. Displacement ($\times \text{Thk}$)	$N_H = 1$	$N_H = 3$	$N_H = 5$	$N_H = 7$
A	1.5	0.055	0.049	0.006	0.004
B	3	0.127	0.191	0.062	0.008
C	4	0.255	0.128	0.009	0.002
D	5	0.280	0.074	0.048	0.037

Table 4: Comparison of periodicity (values of ϵ) of harmonic balance solutions from NNM solution points depicted in Figure 25.

To understand why the various models show errors in periodicity, the difference between the vertical displacement at the initial state, $\mathbf{x}(0)$, and final state $\mathbf{x}(T)$ is plotted in Figure 27 for the points extracted from the NNM plot. The plots coincide with those presented in Table 4 in which the seven harmonic solution is able to maintain a strong periodicity for each point.

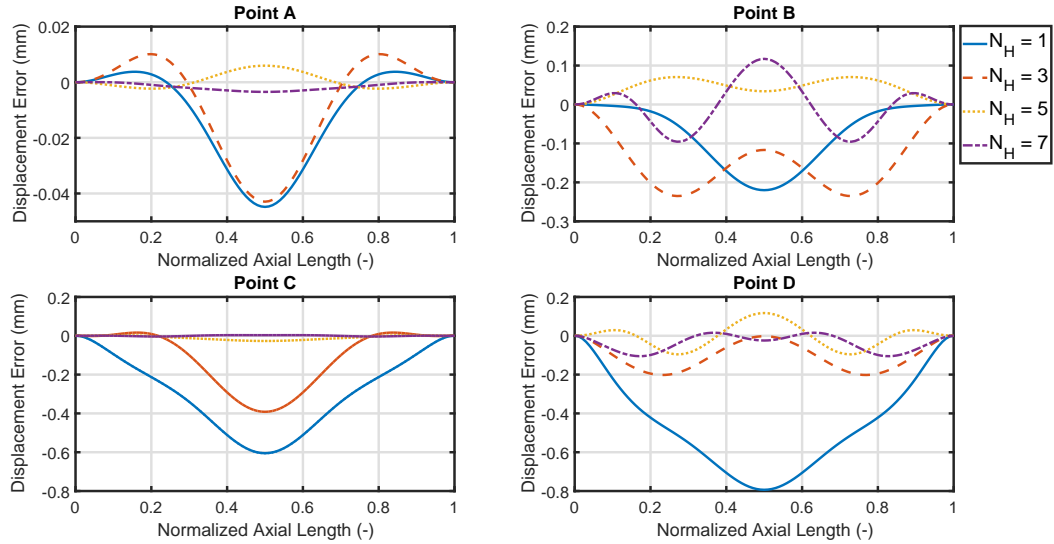


Figure 27: Displacement error, $\mathbf{x}(T) - \mathbf{x}(0)$, or the difference in vertical displacement between the initial displacement of the NNM solutions from Figure 25 and the final displacement after numerically integrating the FE model over the period.

3.5.3 Discovery Experimental Panel

The last numerical study on the application of the multi-harmonic balance method for non-linear finite element models is on the Discovery Experimental Panel (DEP) from [90] shown in Figure 28. This case study is used to show that the method can be applied to large scale systems to compute the periodic response efficiently. The model contains 8267 shell elements with a total of 52,734 DOF with titanium material properties. The panel is constructed of titanium 6Al-2Sn-4Zr-2Mo (Ti-6242) with uniform thicknesses of 50 mil (1.27 mm). The material properties used are defined in Table 5.

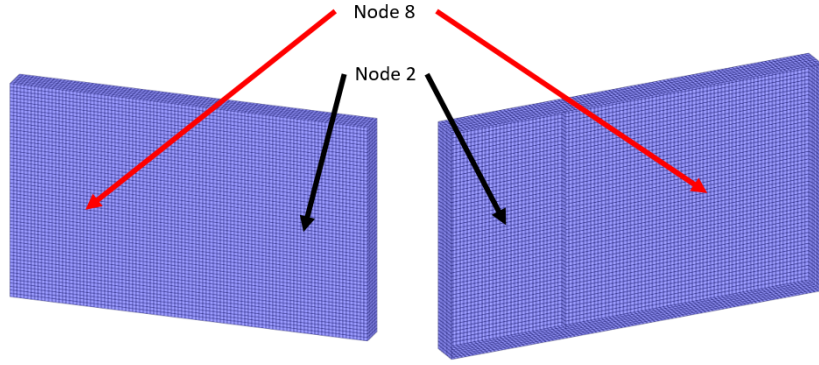


Figure 28: The finite element model used to represent the box panel. The left view is from the top of the panel and the right view is from the bottom of the panel displaying the stiffener along the inside.

Table 5: Material properties of the Discovery Experimental Panel

Modulus of Elasticity	Poisson's Ratio	Density
114.1 GPa	0.32	4,428 kg/m^3

The first 4 linear normal modes of the panel are displayed in Figure 29. In Figure 30 the first nonlinear normal mode is shown for the MHB method when using a single harmonic, two harmonic and three harmonic solution. As with the previous case there is no shooting method

data to compare to so the accuracy of the harmonic balance method must be evaluated by a single numerical integration of the FE model. This is done by computing the periodicity value, ϵ , defined earlier in Eq (63).

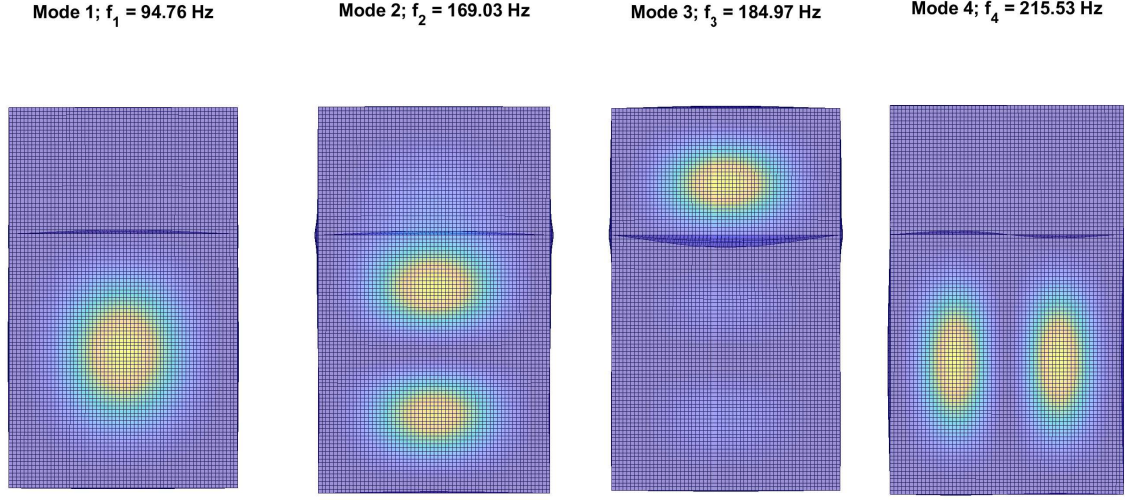


Figure 29: First four linear normal modes of the box panel.

The periodicity values at 100 Hz, 110 Hz, and 120 Hz are given in Table 6 for each harmonic balance solution. At each point, as the number of harmonics are increased, the periodicity value decreases as expected showing that the solution obtained comes closer to satisfying the full FE model. All three models have a reasonable periodicity at point 100 Hz, but at 110 Hz, and 120 Hz there is still some inaccuracy present. If more harmonics were added to the solution the periodicity would presumably decrease but the model was unable to be solved with more than 3 harmonics included in the solution with computing resources available.

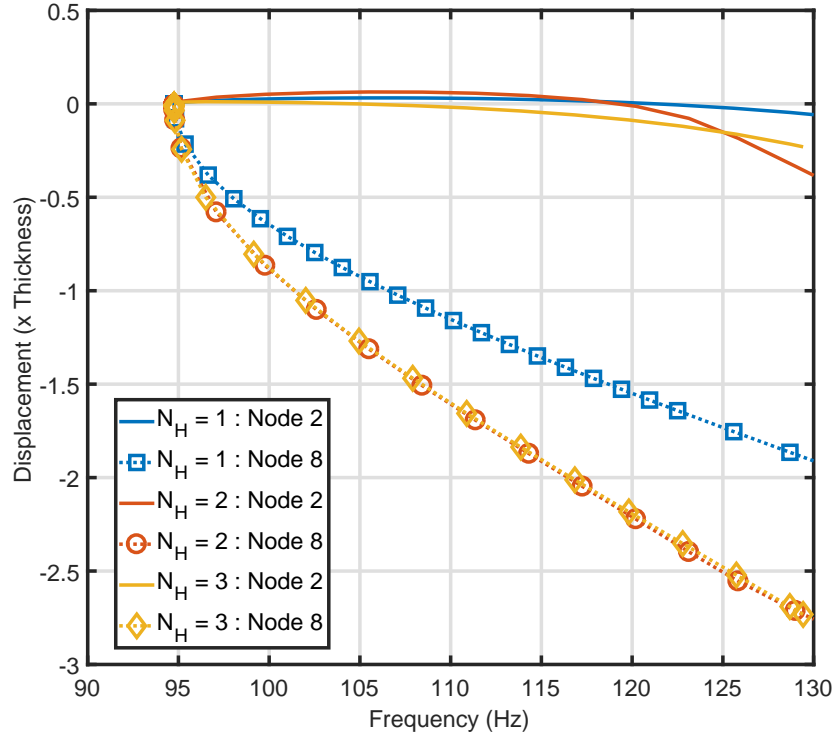


Figure 30: Displacement of nodes 2 and 8 versus frequency depicting NNM of DEP computed using the harmonic balance method.

Table 6: The periodicity values ϵ of the harmonic balance solutions at various frequencies along the 1st NNM depicted in Figure 30.

n_H	100 Hz	110 Hz	120 Hz
1	0.019	0.110	0.124
2	0.012	0.063	0.098
3	0.007	0.047	0.070

3.5.4 Scaling Analysis

In addition to being a robust tool for calculating the NNM's of curved beams, it is now shown that high performance computing can be used to significantly increase the computational efficiency of the MHB method. By parallelizing the calculation of the nonlinear internal force and the nonlinear Jacobian, the MHB method can be applied to much larger FE models,

which have typically been avoided in the literature. For both the nonlinear internal force and the nonlinear Jacobian, the computational cost scales independent of the number of harmonics used within the solution. Furthermore, the scaling is governed only by the cost associated with the discretization of the periodic orbit. While it is typically not a concern for models with smooth nonlinearities and a small number of harmonics, it is important to note that the number of time samples must satisfy the Nyquist condition as the number of harmonics is increased.

The three models included a 10x10 element mesh, a 25x25 mesh model, and a 50x50 mesh model of a flat plate with fixed boundary conditions. Figure 31 shows the total simulation time required to compute each NNM up to twice the linear natural frequency. The time required for the computations was found to fit a similar scaling law for each FE model, and these were compared by fitting a second order power law of the form $y = ax^b + c$ where y is the simulation time, x is the number of cores, and the parameters a , b , and c are coefficients estimated from the fit. The primary coefficient of interest is the power law exponent, b , which dictates the scaling law as the number of cores increases. For the 10×10 mesh, doubling the number of cores from 2 to 4 provided only a 30% reduction in computation time. It is likely that when using a small number of cores for relatively small models the low work to communication ratio presents a more significant bottleneck. For the largest model the computational time was able to be reduced by 40%.

It has been noted in the literature [91] that the major disadvantage of the MHB method is that the system size, and thus the Jacobian, increases linearly with the number of harmonics. This has a negligible effect on the nonlinear force and nonlinear Jacobian generation but does indeed have a significant effect on using a Newton-Raphson correction routine, which requires

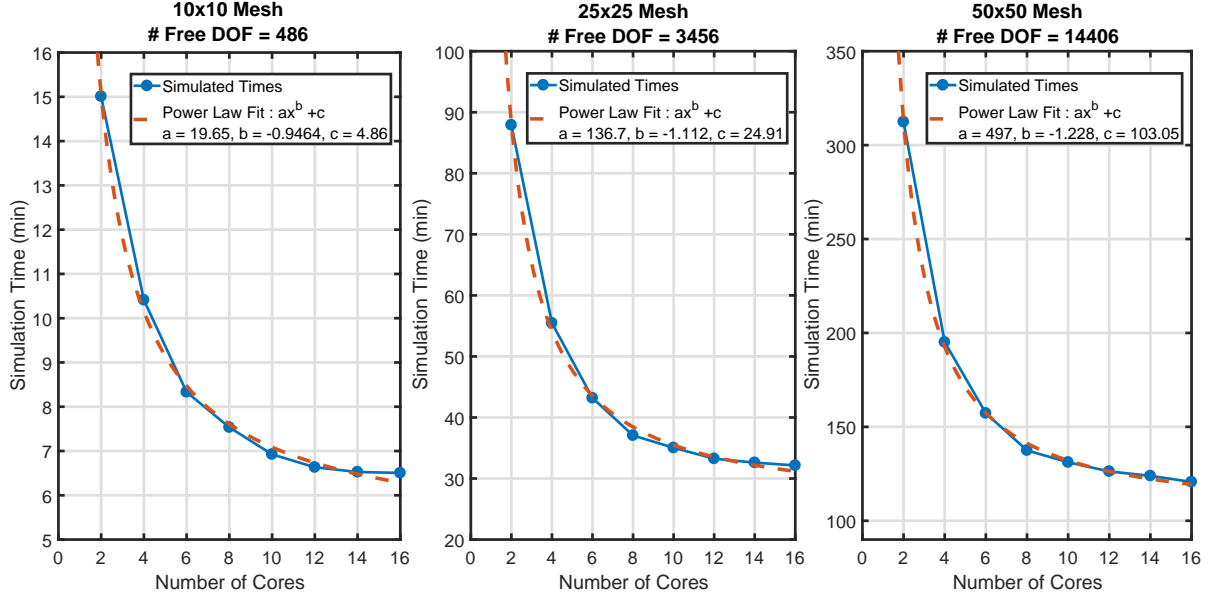


Figure 31: Scaling of total computational time with number of cores for calculation of the NNM up to a 2x frequency shift. Three models are presented: 10x10 mesh, 25x25 mesh, and a 50x50 mesh.

the solution of a system of linear equations. The time required for the solution of the linear system that is solved at each step of the Newton-Rhapson routine is presented in Table 7. For reference, the time required to generate the nonlinear internal force using a serial execution, denoted NL_{Fun} , is also presented. As the number of harmonics increases, the solution of the system starts to dominate the total computational time of the procedure. The method utilized to solve the linear system was back substitution on the sparse matrices, and no parallelization was utilized to accelerate this portion of the algorithm.

Mesh Size	#DOF	NL_{Fun}	$N_H = 1$	$N_H = 3$	$N_H = 5$	$N_H = 7$
10x10	486	6.22	0.21	0.81	2.60	5.94
25x25	3456	37.98	2.70	14.92	56.54	106.50
50x50	14408	155.31	21.44	89.92	522.29	1208.6

Table 7: Comparison of time (seconds) required to solve the linear system of equations generated for the three different sized models versus the number of harmonics included in the solution. The time required to compute nonlinear internal force vector in serial, denoted NL_{Fun} , is also presented for reference.

Even though the increase in Jacobian size burdens the efficiency of the MHB method as the number of harmonics increases, the method still proves more efficient for large scale problems than shooting methods, in particular, the AMF Algorithm [55]. This is demonstrated by comparing the time required to trace a $2\times$ frequency shift of the flat plate's first NNM between the AMF algorithm and the MHB method with an increasing number of harmonics. Parallelization was not used in either case. For each model size the MHB method significantly outperforms the shooting method approach when including up to seven harmonics.

Mesh Size	#DOF	AMF	$N_H = 1$	$N_H = 3$	$N_H = 5$	$N_H = 7$
10x10	486	1202.02	15.01	15.56	17.20	20.26
25x25	3456	8801.45	87.91	98.30	133.67	176.14
50x50	14408	30050*	312.4	361.47	671.34	1163.20

Table 8: Comparison of time (minutes) required to compute the NNM backbone using the AMF Algorithm [55] and the MHB method for the three different models and as the number of harmonics included in the solution is varied. The entries with the symbol (*) denotes an estimated time of simulation; it was not possible to allow the AMF algorithm to run for 20 days to see if it could complete the solution to a $2x$ shift in frequency.

There are a few different approaches that could be considered to address the bottleneck issue of solving the system of linear equations. The first possibility is to switch to an iterative sparse solver, but for the case at hand the Jacobian matrix is not symmetric making the solution difficult at times. The other option would be to investigate the use of the higher dimensional harmonic balance method which computes corrections in the time domain, alleviating the large matrix operation [82].

3.5.5 Discussion

The harmonic balance method has been demonstrated to be an accurate and efficient approach to compute nonlinear normal modes of geometrically nonlinear finite element models. In particular it was applied to complex structures such as the curved beam case which has proven difficult in the past. It was also applied to larger scale structures such as the box panel, where the backbone curve was still able to be computed within a reasonable time frame using up to three harmonics.

3.6 Application to Nonlinear Reduced Order Models

The following sections present material from [53] in which the harmonic balance method was applied to nonlinear reduced order models of geometrically nonlinear structures.

3.6.1 Flat Clamped-Clamped Beam

The first numerical study is a clamped-clamped flat beam with geometric nonlinearity present. This is the same beam as introduced in Section 3.5.1 but now a reduced order model is used to compute the nonlinear normal modes. The reduced order model consists of the first 4 symmetric modes of the system, (1, 3, 5, 7). This ROM is known to be accurate based on work from [62].

The first NNM of the beam was computed using the shooting method in [72] in order to compare the harmonic balance method's accuracy. The computed NNMs are presented in Figure 32. The NNM computed using only one harmonic does not capture any of the internal resonances as expected but traces the primary backbone computed using shooting

method. When including the first three harmonics of the system the NNM also does not identify any of the internal resonances.

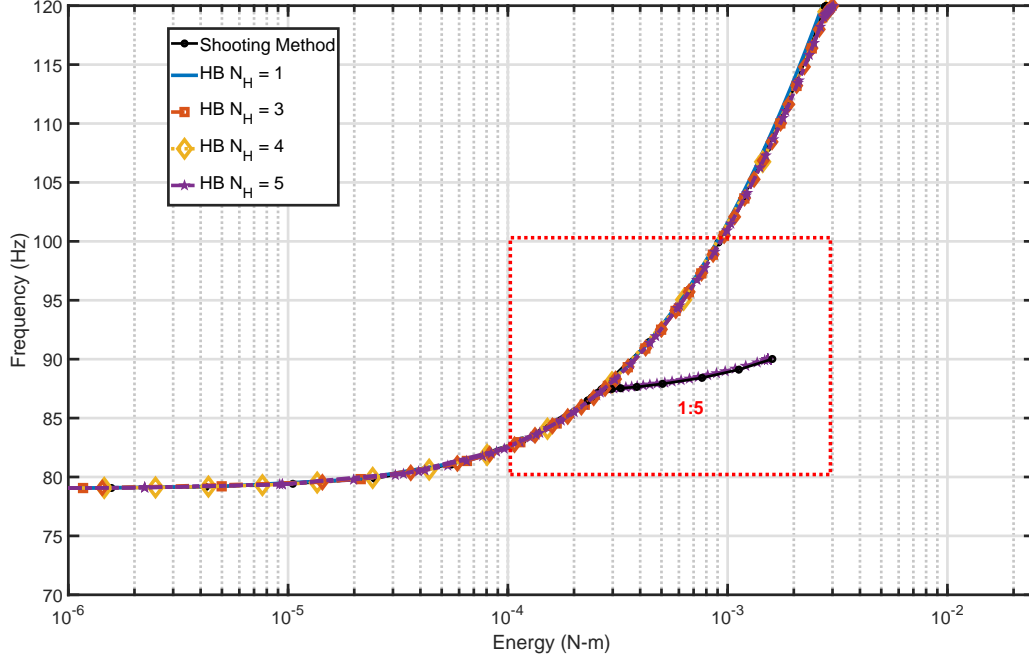


Figure 32: Comparison of 1st NNM of clamped-clamped beam computed using a shooting method and using the HB method with varying numbers of harmonics.

Once the fifth harmonic is added to the system, the 1:5 internal resonance is captured at 88 Hz. Figure 33 shows this internal resonance in detail, and that it is very accurately tracked by the 5 harmonic HB method. The reader can refer to Section 3.5.1 to see how the periodic motion looks in the physical and modal domain.

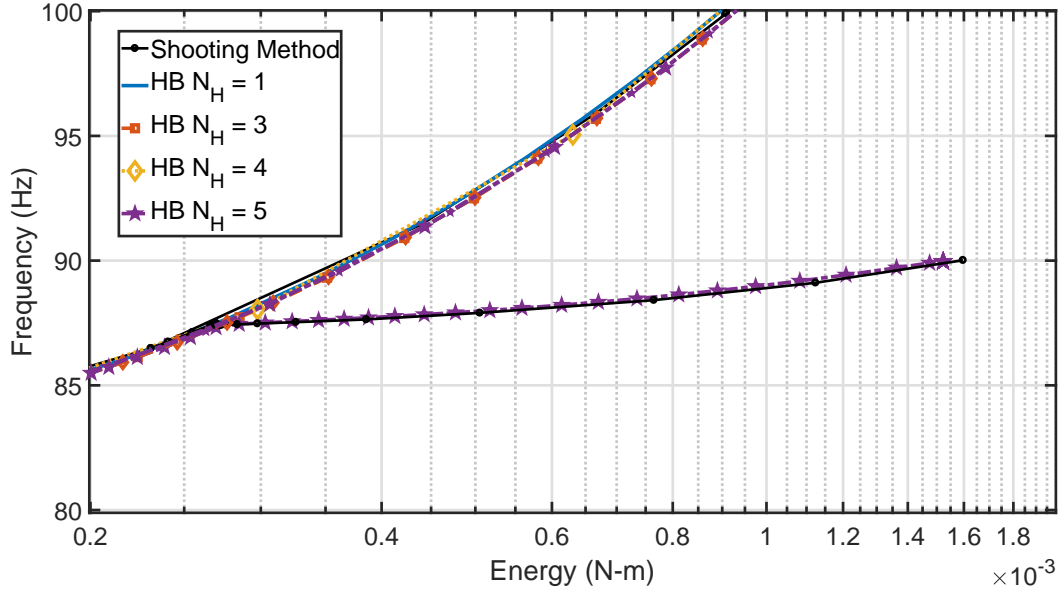


Figure 33: Zoomed in portion of Figure 32 showing 1:5 Internal Resonance.

In order to understand how the accuracy of the harmonic balance solution changes with the number of harmonics the primary backbone solutions were isolated to compare with the shooting method. The primary backbones computed by each algorithm are presented in Figure 34, revealing that the curves are nearly indistinguishable. The horizontal lines on Figure 34 represent the point along the NNM backbone at which the structure has displacements of 1x-, 2x-, 4x the beams thickness. To quantify the accuracy more rigorously, at a certain set of frequencies the error in the energy was calculated. The errors in energy were then calculated for each frequency value and are presented on the right hand side of Figure 34 as a grouped bar plot. The error between the one term harmonic balance and the shooting method increases as the NNM increases in frequency but only contains an error of 4.9% at 107 Hz with a displacement of 2x the thickness and 12.36% at 180 Hz with a displacement of over 4x the thickness. For the 3-,4- and 5-harmonic models the error throughout the NNM curve up to 140 Hz remains below 2%. As the number of harmonics included increases the

accuracy of the method is increased in comparison with the shooting method, this is shown looking at the error in energy at 180 Hz.

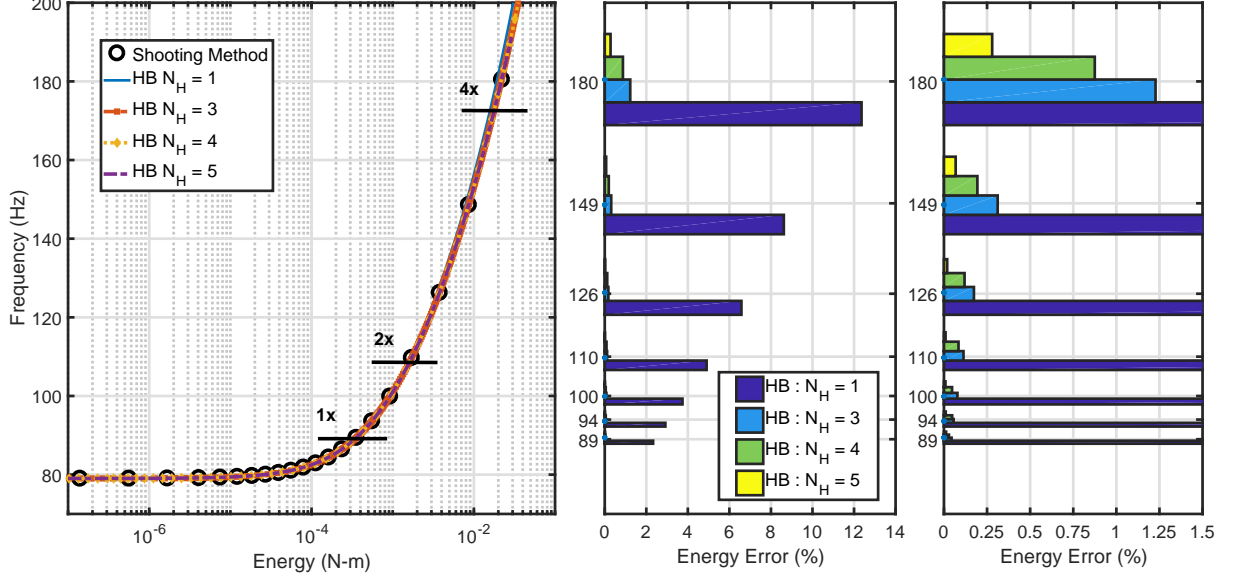


Figure 34: (a) Comparison of 1st NNM isolating only the primary backbone. (b) Relative errors in energy of the HB algorithm with the shooting method at interpolated solution points. (c) Zoomed in portion of errors in energy highlighting the 3-, 4-, and 5-harmonic model values.

3.6.2 Discovery Experimental Panel

The second example is a significantly larger FE model with more complex geometry, it demonstrates the computational advantage of using a ROM. The discovery experimental panel (DEP) FE model was introduced earlier in Section 3.5.3. The DEP finite element model was reduced to a 6 mode ROM using the IC method including modes 1, 2, 3, 5, 8 and 11 to compute the NNMs. The linear modes of the DEP used as basis vectors within the ROM are given in Table 9.

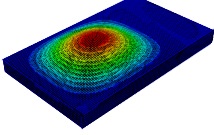
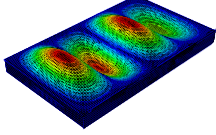
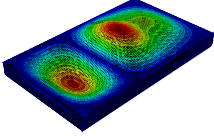
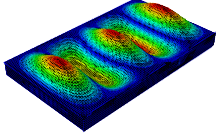
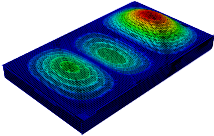
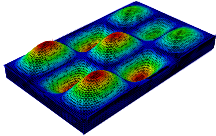
Mode	Frequency (Hz)	Plot	Mode	Frequency (Hz)	Plot
1	96.44		5	291.59	
2	166.57		8	390.74	
3	183.73		11	478.71	

Table 9: The linear modes of DEP used within ROM showing the frequency and shape

The first NNM of the DEP, as computed using the HB method with various number of harmonics, is presented in Figure 35 along with the NNM computed using the shooting method. The NNM contains an internal resonance branch at 98 Hz with a ratio of 1:4 with the 8th mode of the system.

The harmonic balance solution with only 1 harmonic included computes only the primary backbone branch of the NNM. When including harmonics 1-5, the system identifies and tracks the 1:4 internal resonance branch. A closer look at 1:4 internal resonance branch is provided in Figure 36 in which the HB method traces the internal resonance branch accurately. As the number of harmonics included increased to 7 the system showed the same characteristics.

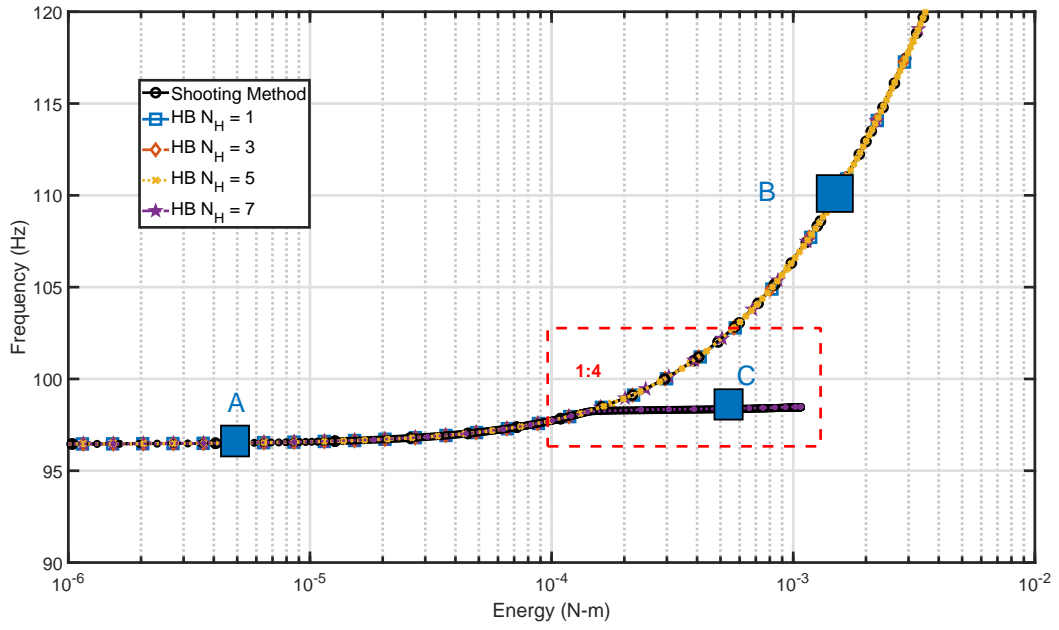


Figure 35: First NNM of DEP computed using the harmonic balance method with increasing harmonics included and the shooting method

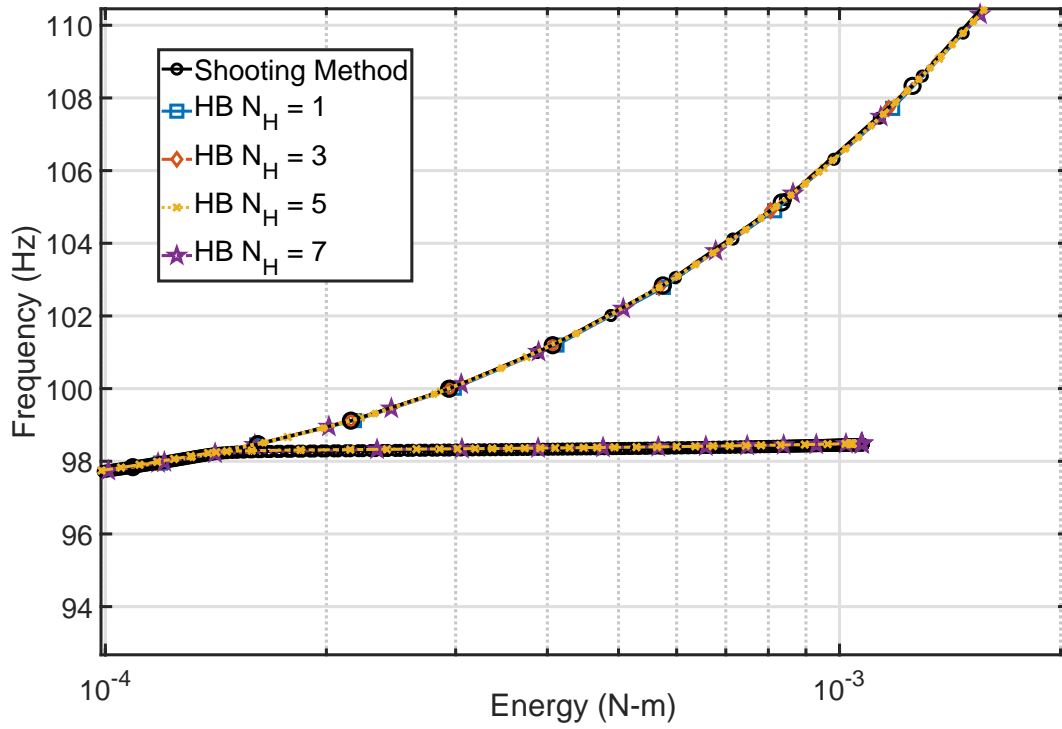


Figure 36: Zoomed in portion of 1st NNM of DEP depicted in 35 highlighting the 1:4 internal resonance branch.

To depict how the shape of deformation of the panel changes throughout the NNM, the deformation shapes at the points labeled in Figure 35 are presented in Figure 37. Points along the primary backbone and along the internal resonance branches are shown. For reference, point B along the primary backbone branch is when the panel deflects 1x the thickness of the structure.

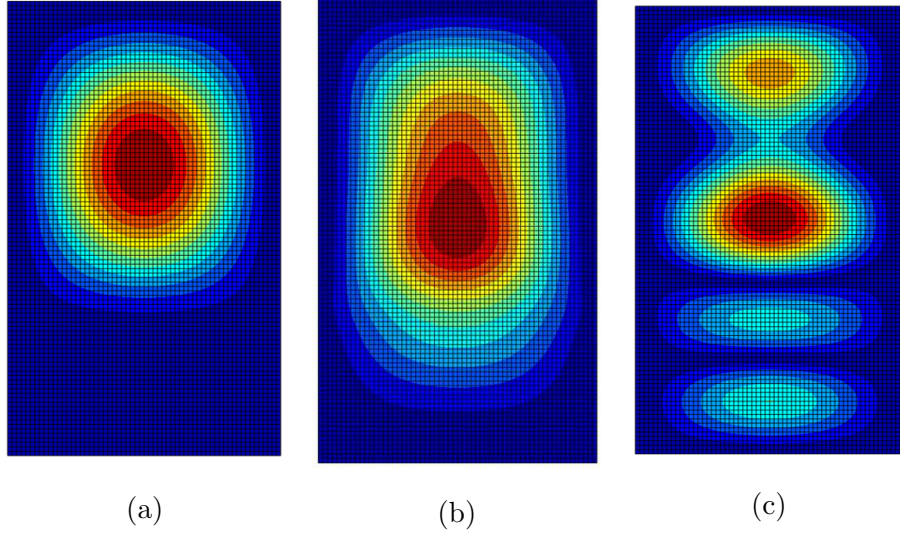


Figure 37: Deformation of DEP at solution points identified in Figure 35 along the NNM for the 5-term harmonic balance model (a) Deformation at NNM1 Solution Point A along the primary backbone branch (b) Deformation at NNM1 Solution Point B along the primary backbone branch (c) Deformation at NNM1 Solution Point C along the 1:4 Internal Resonance Branch.

As was done for the flat beam, the accuracy of the backbone for each HB model was quantified by computing their error relative to the Shooting Method solution. The primary backbone of the NNM of the DEP system is presented on the left hand side of Figure 38 in which each model appears to provide similar results. The errors in energy for each interpolated frequency value are presented on the right hand side of Figure 38. As was seen with the flat beam, the error in the one term harmonic balance solution is seen to increase as the energy of the system increases. The energy error of the 1-term harmonic balance method

reaches a maximum of 10% at 354 Hz at which point it has a maximum displacement of 2x the thickness of the structure. Similarly, for the 3-, 5- and 7-term harmonic balance solutions, the error throughout the NNM curve up to 360 Hz also continues to increase. For each HB solution, the maximum error over the computed NNM portion decreases as the number of harmonics included increases, with the 7-term model having a maximum error of less than 2%.

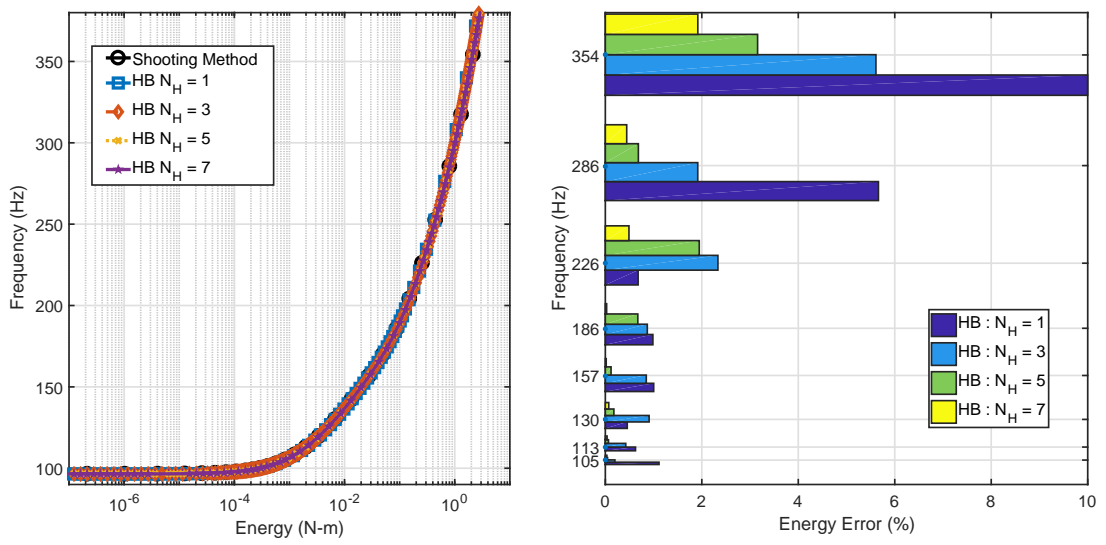


Figure 38: (a) Comparison of 1st NNM isolating only the primary backbone. (b) Relative Errors in energy of the HB algorithm with the shooting method at interpolated solution points.

A computational comparison between computing the nonlinear normal modes of the panel structure using the FE method versus using a reduced order model is presented in Table 10. The time required to compute the NNMs of the ROMs is order is orders of magnitude less than when computing them using a FE model. For ROMs of this size the computational time to generate them is negligible as well but there is the hidden cost of an analyst's time to ensure that the ROM is accurate.

Table 10: Computational time (minutes) to compute nonlinear normal mode of the panel structure when using a finite element model and a reduced order model.

N_H	FE	ROM		
		1 Mode	3 Mode	6 Mode
1	122	<1	1.1	2.1
3	368	<1	2.1	3.8
5	NA	2.2	4.5	6.3

3.6.3 Curved Clamped-Clamped Beam

The last numerical example presented in this work is a curved beam model in which the system dynamics have proved to be more complex than the previously studied flat structures [89]. The general geometry of the curved beam was presented in Figure 23, but this beam has different dimensions. The beam has a radius of curvature of 22860 mm (900 in) resulting in a maximum height of 0.508 mm (0.02 in) which is equal to the thickness of the beam, a thickness of (0.02) inches, a length of 12 (in) and a width of 0.5 inches. It has steel material properties as described earlier. The curved beam was reduced down to a 11-mode ICE ROM with linear modes [1-5, 7, 9, 11, 12, 14, 16] included within the basis set; this was determined to be accurate in [89].

The 1st NNM of the curved beam is presented in Figure 39, in which it exhibits a softening behavior followed by hardening as the deflection approaches one thickness. The single harmonic model shows some error in describing the softening behavior, but is still quite accurate as the frequency error is only 2.5% at the lowest frequency that the NNM reaches. When at least 3 harmonics are included the softening is accurately captured. Additionally this systems contains complex internal resonance branches which become difficult to fully trace out as the number of harmonics increases. The shooting algorithm was unable to

continue past the second internal resonance branch and took many restarts to get past the first branch.

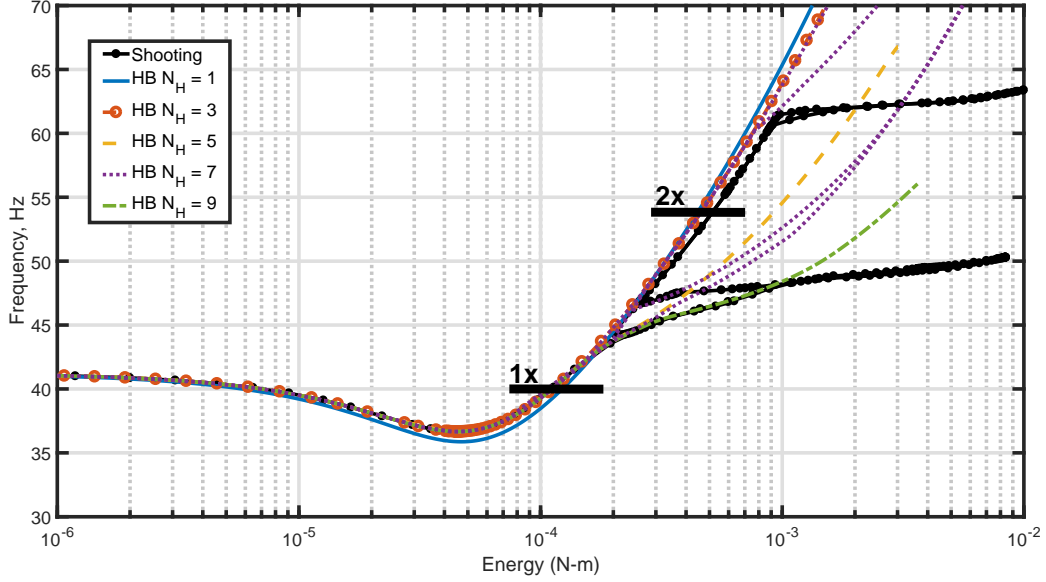


Figure 39: First NNM of the curved beam computed using shooting (truth solution) and using the harmonic balance method with an increasing number of harmonics included.

The harmonic balance method also has difficulties continuing past some of the internal resonances when enough harmonics are included to identify them. Because of these difficulties, it becomes challenging to compare the shooting and harmonic balance solutions over the full range of frequency and energy that is of interest. Additionally, because the backbones are our primary interest, it does not seem wise to invest a lot of effort into computing complicated internal resonance branches simply to be able to compare those sections of the NNM along the backbone.

One benefit of the harmonic balance method is that the primary backbone is able to be computed, excluding any internal resonances, and then higher harmonic solutions are able to be restarted at desired points. This allows one to tailor the accuracy of the solution at

specific frequencies or energies of interest. Convergence is identified by looking at the change in the predicted solution value with increasing number of harmonics at a specific frequency.

Figure 40 presents the convergence of a NNM solution for an increasing number of harmonics started from 55 Hz and 100 Hz respectively from a 1-harmonic solution. The change in the energy of the solution is plotted as the harmonic order increases, for example with 1-3 indicating the change in energy between the 3-harmonic solution and the 1-harmonic solution. In each case there is a large change in energy from the 1 harmonic model to the 3 harmonic model. Once three harmonics are included within the system the percent energy change remains below 1%. Going from 13 to 15 harmonics the energy change goes to zero in both cases.

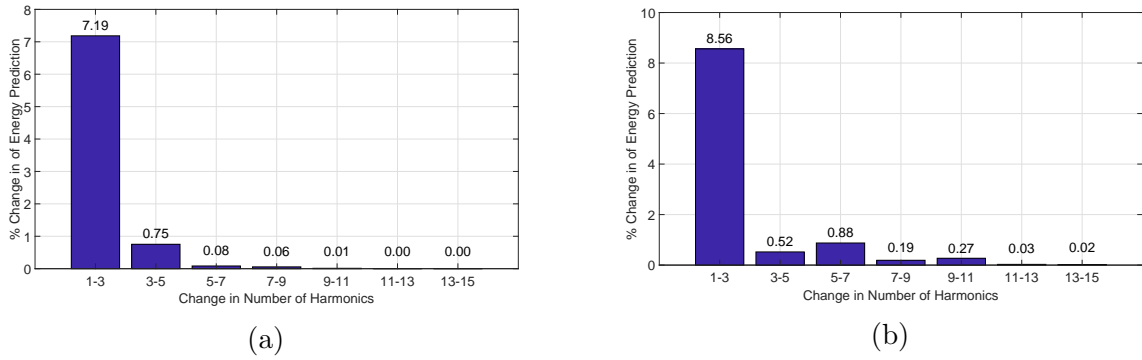


Figure 40: Convergence of NNM solution energy values started from single harmonic solutions (a) Relative energy error computed at 55 Hz with respect to 15 harmonic model (b) Relative energy error computed at 100 Hz with respect to 15 harmonic model

3.6.4 Discussion

The harmonic balance method has been demonstrated to be an efficient and robust method to computing periodic solutions of nonlinear modal methods generated from IC method. For low order ROMs the computation of a single NNM solution is less than a minute even when including up to 7 harmonics, which typically provides accurate estimates of the primary

backbone curve.

4 Nonlinear Model Updating Procedure

This portion of the paper presents the model updating procedure including an overview of the algorithm, the determination of semi-analytical gradients, and application to some sample nonlinear systems of interest. The formulation is presented in terms of a FE model, and comments will be detailed when portions specific to ROMs deviates from the FE model derivation.

4.1 Algorithm Overview

The method used in this work utilizes all of the NNM information at once in order to update the nonlinear system at each of the optimization routine iterations. The procedure is presented graphically in Figure 41. First, the entire NNM branch is computed up to a specified frequency, amplitude or energy level by applying the MHB method to the initial model of the structure. Then, a state vector is formed which includes either the full displacement field or modal displacements at different time instants within the fundamental period at each point along the NNM paired with the frequency of the NNM solution. An optimization algorithm is then used to update the model parameters and its corresponding NNM and state vector using an objective function to iteratively converge upon an objective NNM and its state vector within some tolerance. An outline of the algorithm is presented in Figure 41.

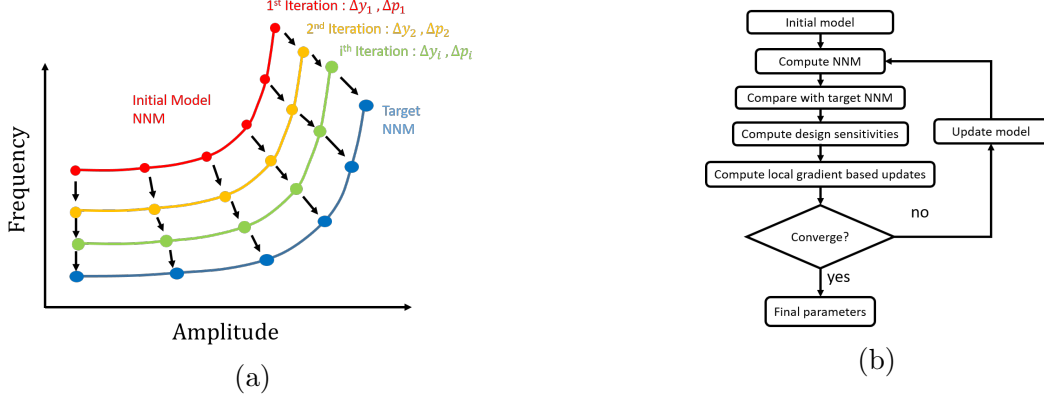


Figure 41: Representation of the proposed model correlation procedure: (a) graphical representation. (b) flow chart.

4.2 Gradient Based Optimization Routine Setup

The objective function, Π , selected for this work is the scalar quadratic function shown in Eq (64), which accounts for both the error in the state variables and the change to the design parameters. This type of objective function is frequently used in model updating because it drives the routine to search for the smallest changes in parameters (i.e. assuming they are reasonably accurate initially or so they stay within physically reasonable bounds), while also seeking the greatest accuracy in fitting the measurements.

$$\Pi = \Delta \mathbf{y}^T \mathbf{W}_s \Delta \mathbf{y} + \gamma \Delta \mathbf{p}^T \mathbf{W}_p \Delta \mathbf{p} \quad (64)$$

The difference between the current and target state variables, $\Delta \mathbf{y}$, is a vector of size $[N_s \times 1]$, where N_s is the number of state variables (i.e. points on the NNM curves), while $\Delta \mathbf{p}$ is the vector of changes to the design variables, whose size is $[N_p \times 1]$, where N_p is the number of design parameters. The objective function equation also contains three weighting matrices: \mathbf{W}_s , a diagonal matrix of state variable weights, \mathbf{W}_p , a diagonal matrix of design

variable weights, and the scalar term, γ , which balances the importance of the state variable term (i.e. the level of agreement of the model) with the changes to the design parameters. In order to improve the performance of the optimization routine it is important to compute the gradient of the objective function, which is found to be

$$\nabla \Pi = 2\mathbf{D}^T \mathbf{W}_s \Delta \mathbf{y} + 2\gamma \mathbf{W}_p \Delta \mathbf{p} \quad (65)$$

where \mathbf{D} represents the gradient of the state variable error with respect to the design variables such as $\partial \Delta \mathbf{y} / \partial \mathbf{p}$. The state variable errors are the euclidean norms of the difference between each measured (or target) NNM solution and the numerical model's NNM solution in displacement-frequency space, denoted as

$$\Delta \mathbf{y} = \begin{bmatrix} \Delta s_1 & \Delta s_2 & \cdots & \Delta s_{N_{nnm}} \end{bmatrix} \quad (66)$$

where $\Delta \mathbf{s}$ is the residual vector at each NNM solution and N_{nnm} is the number of points along the NNM branch that have been measured. The form of $\Delta \mathbf{y}$ depends on the data available from the experimental test, the vector may contain either physical displacement(s), modal amplitude(s), or the Fourier coefficient of the NNM solutions along the NNM branch. For example, the euclidean norm vector when using displacement at a single time point along

the periodic orbit for the k^{th} solution along the NNM branch would be

$$\Delta s_k = \left\| \begin{bmatrix} x_1 \\ x_2 \\ \vdots \\ x_n \\ \omega \end{bmatrix}^{(target)} - \begin{bmatrix} x_1 \\ x_2 \\ \vdots \\ x_n \\ \omega \end{bmatrix}^{(model)} \right\|_{(k)} \quad (67)$$

This can be extended to be evaluated at multiple points along the periodic orbit or to the case where the Fourier coefficients of the periodic response are used as state variables. The state variables that are directly computed from MHB are the Fourier coefficients and frequencies at the NNM solutions. However, these can be converted to actual physical displacements at instants in time, the euclidean norm distance, etc.

The optimization algorithm that is utilized to minimize the objective function is the Interior-Point algorithm [92, 93], a gradient based method, which is implemented in the Matlab [®] optimization toolbox function *fmincon*. It is important to note that since this model updating approach utilizes gradient based optimization routine that the once the objective function is minimized via the optimization algorithm only a local minimum can be achieved. In the sense of model updating this means that we cannot prove that the parameters identified are the "true" parameters. Instead all that can be provided about the final parameters are that they improve the accuracy of the model.

4.3 Computation of NNM Design Sensitivities within Harmonic Balance Framework

The design sensitivities, \mathbf{D} or $\partial\Delta\mathbf{y}/\partial\mathbf{p}$, could be computed numerically with finite difference methods for each of the state variables presented. However, this is not advisable as it can introduce errors into the analysis and adds significant computational overhead; to use finite differences, N_p additional NNMs would have to be computed at each iteration of the optimization routine. For a ROM, the computation of each NNM is relatively inexpensive but as the number of modes retained in the ROM increases the number of parameters in the model updating routine, the nonlinear stiffness coefficients, increases on the order of cubic requiring many additional NNM computations. For a finite element model, on the other hand, the number of parameters may be small, but each NNM computation is significantly more expensive due to the large number of DOF required to model the structures accurately.

In the authors' original work [27] a procedure based upon the Implicit Function Theorem was utilized to identify the gradients of the frequency and Fourier coefficients with respect to design parameters independently. In that formulation some coupling between frequency and the Fourier coefficients was not captured resulting in less accurate gradients for systems with strong nonlinearities. In this work a total derivative approach is utilized to identify the design sensitivities of the NNM solutions with respect to the design parameters. This procedure is better able to capture the coupling, determined by comparing with gradients computed using the finite difference method, but requires a minimum-norm solution to an underdetermined system of equations which will be discussed later in the section.

The sensitivity of the frequency with respect to the design parameters is denoted $\mathbf{D}_\omega =$

$\partial\omega/\partial\mathbf{p}$ while the sensitivity of the Fourier coefficients is $\mathbf{D}_{\mathbf{z}} = \partial\mathbf{z}/\partial\mathbf{p}$. The harmonic balance equation shown in Eq (40) cannot be used to directly compute the design sensitivities because it is only a function of \mathbf{z} and ω . It is also implicitly a function of the design parameters, \mathbf{p} , which for the study at hand are the nonlinear stiffness terms. The first step is to explicitly incorporate the design variables as free parameters of the solution.

$$\mathbf{h}(\mathbf{z}, \omega, \mathbf{p}) = \mathbf{A}(\omega, \mathbf{p})\mathbf{z} + \mathbf{F}(\mathbf{z}, \mathbf{p}) \quad (68)$$

This allows the relation between the ω , \mathbf{z} , and \mathbf{p} to be found which in turn can be used to identify relationships between their derivatives e.g. the design parameter sensitivities. The dependence on ω , \mathbf{z} , and \mathbf{p} will be dropped from here forward for brevity. The Jacobian of Eq (68) with respect to the the Fourier coefficients, $\partial\mathbf{h}/\partial\mathbf{z}$, and the Jacobian with respect to the frequency $\partial\mathbf{h}/\partial\omega$ have the same form as presented in Section II.A.2. The gradient with respect to the free parameters, $\partial\mathbf{h}/\partial\mathbf{p}$, is

$$\frac{\partial\mathbf{h}(\mathbf{z}, \omega, \mathbf{p})}{\partial\mathbf{p}} = \frac{\partial\mathbf{A}(\omega, \mathbf{p})}{\partial\mathbf{p}}\mathbf{z} - \frac{\partial\mathbf{F}(\mathbf{z}, \mathbf{p})}{\partial\mathbf{p}} \quad (69)$$

where the influence of the parameters on the linear dynamics of the system is captured in the first term, and the influence on the nonlinear portion are determined in the second. The sensitivity of the first term, assuming the nonlinear normal mode formula in which damping is neglected, is found as

$$\frac{\partial\mathbf{A}(\omega, \mathbf{p})}{\partial\mathbf{p}} = \nabla^2 \otimes \frac{\partial\mathbf{M}}{\partial\mathbf{p}} + \mathbf{I}_{2n_h+1} \otimes \frac{\partial\mathbf{K}}{\partial\mathbf{p}} \quad (70)$$

which requires sensitivities of the linear matrices with respect to the design parameters. For a finite element model the parameters included within the model updating routine, may alter both the mass and stiffness matrices. The gradient terms can be identified via sensitivity analysis, i.e. finite difference methods, which is commonly done in linear model updating routines and found in commercial software. In this work since the model updating is performed in an in-house finite element code in Matlab the gradients are computed using the complex step method [94] to reduce potential errors associated with small step size choices in the finite difference routine. The method has been used in many works and across many fields [19, 95, 96, 97] and relies on taking the perturbation step in the complex domain. For example if the gradient of the mass matrix with respect to the j^{th} parameter is desired it can be computed via the complex step method by first perturbing the j^{th} parameter in the complex domain as

$$p_j = p_j + i\Delta s \quad (71)$$

where i here is to denote the complex part of the equation and Δs denotes the step size. The gradient is then found by first assembling the mass matrix with the complex values followed by taking the imaginary portion of the matrix and dividing by the step-size as shown below

$$\frac{\partial \mathbf{M}}{\partial p_j} = \frac{\text{imag}(\mathbf{M})}{\Delta s} \quad (72)$$

this procedure is also applied to the linear stiffness gradient procedure and the nonlinear stiffness gradient procedure for the FE model presented in the following section.

For a reduced order model, the mass term \mathbf{M} is replaced by an identity matrix of size

$[m \times m]$ since the ROM is typically mass normalized and thus it will not be dependent on the free parameters of the system. The only free linear parameters of the linear dynamic matrix of a ROM are the natural frequencies which dictate the linear stiffness of the model as $\Lambda = \text{diag} \left(\begin{bmatrix} \omega_1^2 & \dots & \omega_i^2 & \dots & \omega_m^2 \end{bmatrix} \right)$. For the ROMs these will typically be held constant during the model updating procedure based on linear modal analysis results. As a result for a ROM in this work the linear dynamic gradient, $\partial \mathbf{A}(\omega, \mathbf{p}) / \partial \mathbf{p}$, is zero.

The computation of the nonlinear internal force gradient with respect to the design parameters follows similarly to that of determining the gradient of the internal force with respect to the Fourier coefficients from Section 3.2.2. The Fourier transformation operator is used to transform the time domain gradients, computed at each point along the orbit, to the frequency domain. Since the parameters themselves are not time dependent this equation does not have to be post-multiplied by the inverse Fourier transformation and the gradient are found via

$$\frac{\partial \mathbf{F}}{\partial \mathbf{p}} = \frac{\partial \left(\mathbf{\Gamma}(\omega)^+ \tilde{\mathbf{f}} \right)}{\partial \mathbf{p}} = \mathbf{\Gamma}(\omega)^+ \frac{\partial \tilde{\mathbf{f}}}{\partial \mathbf{p}} \quad (73)$$

where $\partial \tilde{\mathbf{f}} / \partial \mathbf{p}$ is a $[nN \times N_p]$ matrix which represents the sensitivity (gradient) of each solution along the assumed periodic orbit with respect to the design parameters. For discrete nonlinear systems, such as reduced order models, this is known analytically at each point, as is demonstrated in Section 4.3.1. For a finite element model, closed form expressions are usually not available but still a computationally efficient generation procedure is presented in Section 4.3.2.

Now that all of the Jacobian terms have been identified, the design sensitivities can be

obtained by taking the total derivative of Eq (68) with respect to the design parameters as

$$\frac{\partial \mathbf{h}}{\partial \mathbf{p}} + \frac{\partial \mathbf{h}}{\partial \omega} \frac{\partial \omega}{\partial \mathbf{p}} + \frac{\partial \mathbf{h}}{\partial \mathbf{z}} \frac{\partial \mathbf{z}}{\partial \mathbf{p}} = 0 \quad (74)$$

which can be reorganized into matrix form as

$$\frac{\partial \mathbf{h}}{\partial \mathbf{p}} + \begin{bmatrix} \frac{\partial \mathbf{h}}{\partial \mathbf{z}} & \frac{\partial \mathbf{h}}{\partial \omega} \end{bmatrix} \begin{bmatrix} \frac{\partial \mathbf{z}}{\partial \mathbf{p}} \\ \frac{\partial \omega}{\partial \mathbf{p}} \end{bmatrix} = 0 \quad (75)$$

The design sensitivities are solved for by moving $\partial \mathbf{h} / \partial \mathbf{p}$ to the other side and taking the pseudo-inverse of the matrix containing the harmonic balance gradients with respect to the Fourier coefficients and frequency. The matrix to be inverted is $[(2N_H + 1)n \times (2N_H + 1)n + 1]$ which is not full row rank resulting in a null-space of dimension one. The rank deficiency of the matrix thus requires the pseudo-inverse to obtain a minimum norm solution of the system.

$$\begin{bmatrix} \frac{\partial \mathbf{z}}{\partial \mathbf{p}} \\ \frac{\partial \omega}{\partial \mathbf{p}} \end{bmatrix} = - \begin{bmatrix} \frac{\partial \mathbf{h}}{\partial \mathbf{z}} & \frac{\partial \mathbf{h}}{\partial \omega} \end{bmatrix}^+ \frac{\partial \mathbf{h}}{\partial \mathbf{p}} \quad (76)$$

Replacing the right hand side terms in Eq (76) with those terms derived previously, we obtain,

$$\begin{bmatrix} \mathbf{D}_z \\ \mathbf{D}_\omega \end{bmatrix} = \begin{bmatrix} \frac{\partial \mathbf{z}}{\partial \mathbf{p}} \\ \frac{\partial \omega}{\partial \mathbf{p}} \end{bmatrix} = - \begin{bmatrix} \mathbf{A} + \Gamma^+ \frac{\partial \tilde{\mathbf{f}}}{\partial \tilde{\mathbf{q}}} \Gamma & \frac{\partial \mathbf{A}}{\partial \omega} \mathbf{z} \end{bmatrix}^+ \left[\left(\nabla^2 \otimes \frac{\partial \mathbf{M}}{\partial \mathbf{p}} + \mathbf{I}_n \otimes \frac{\partial \mathbf{K}}{\partial \mathbf{p}} \right) \mathbf{z} + \Gamma(\omega)^+ \frac{\partial \tilde{\mathbf{f}}}{\partial \mathbf{p}} \right] \quad (77)$$

The result is a $[(2N_H + 1)n \times N_p]$ matrix for $\partial \mathbf{z} / \partial \mathbf{p}$ and a $[1 \times N_p]$ vector representing $\partial \omega / \partial \mathbf{p}$. The solution to Eq (77) as stated can be computed using a pseudo-inverse to obtain

a minimum normal solution of the system of equations. In this work, the pseudo-inverse is computed using the Complete Orthogonal Decomposition (COD) within the Matlab function *lsqminnorm*. One of the reasoning for this choice is that Matlab's default pseudo-inverse function, *pinv*, which relies on a singular value decomposition does not work well for large sparse systems which is required for FE models. Alternatively, one could also use the Moore-Penrose pseudo inverse, but this is not as efficient as the COD method.

To obtain the displacement design sensitives, the Fourier coefficient gradients can be transformed to the time domain using

$$\mathbf{D}_{\mathbf{x}} = \frac{\partial \mathbf{x}}{\partial \mathbf{p}} = (\mathbf{Q}(t) \otimes \mathbf{I}_n) \frac{\partial \mathbf{z}}{\partial \mathbf{p}} \quad (78)$$

where $\mathbf{Q}(t)$ is defined previously in Eq (31), and produces a $[nN \times N_p]$ matrix of design sensitivities of displacements solutions along the periodic orbit with respect to the design parameters. This information can be reduced to a smaller set of $[n \times N_p]$ by limiting the state variable at each NNM solution to a single point along the periodic orbit, consisting of all physical DOF.

Similarly, if updating a ROM to obtain the modal amplitude design sensitives, the Fourier coefficient gradients can be transformed to the time domain using

$$\mathbf{D}_{\mathbf{q}} = \frac{\partial \mathbf{q}}{\partial \mathbf{p}} = (\mathbf{Q}(t) \otimes \mathbf{I}_m) \frac{\partial \mathbf{z}}{\partial \mathbf{p}} \quad (79)$$

which produces a $[mN \times N_p]$ matrix of design sensitivities of modal displacements solutions along the periodic orbit with respect to the nonlinear stiffness coefficients. This information

can be reduced to a smaller set of $[m \times N_p]$ by limiting the state variable at each NNM solution to a single point along the periodic orbit, consisting of all modal DOF. Furthermore this can be expanded to physical displacements if desired by

$$\mathbf{D}_x = \frac{\partial \mathbf{x}}{\partial \mathbf{p}} = \boldsymbol{\varphi} \mathbf{D}_q = \boldsymbol{\varphi} \frac{\partial \mathbf{q}}{\partial \mathbf{p}} \quad (80)$$

which is just a linear transformation from the modal space to the physical space using the basis vectors in the ROM, $\boldsymbol{\varphi}$.

4.3.1 Reduced Order Model Nonlinear Internal Force Gradient

The gradient of $\frac{\partial \tilde{\mathbf{f}}}{\partial \mathbf{p}}$ from Eq (73) is presented here for a 1-DOF ROM with polynomial nonlinearities. Consider the SDOF system where the nonlinear internal force is a function of displacement along the periodic orbit and the polynomial nonlinear stiffness terms as

$$\tilde{\mathbf{f}} = \begin{bmatrix} \alpha x(t_0)^2 + \beta x(t_0)^3 \\ \alpha x(t_1)^2 + \beta x(t_1)^3 \\ \vdots \\ \alpha x(t_N)^2 + \beta x(t_N)^3 \end{bmatrix} \quad (81)$$

where the design parameters are the quadratic and cubic coefficients, α and β . The gradient of the response with respect to those parameters is simply

$$\frac{\partial \tilde{\mathbf{f}}}{\partial \mathbf{p}} = \begin{bmatrix} \frac{\partial \tilde{f}}{\partial \alpha} & \frac{\partial \tilde{f}}{\partial \beta} \end{bmatrix} = \begin{bmatrix} x(t_0)^2 & x(t_0)^3 \\ x(t_1)^2 & x(t_1)^3 \\ \vdots & \vdots \\ x(t_N)^2 & x(t_N)^3 \end{bmatrix} \quad (82)$$

This above approach can be easily extended to multi-DOF systems and is computationally efficient. A graphical demonstration of the gradients of a SDOF system with pure hardening response is presented in Figure 42. Subplot (a) displays the gradients of the displacement at each point along the NNM branch with respect to the two parameters, while subplot (b) presents how the frequency changes with respect to a unit change in the design variables. The cubic nonlinearity has a hardening affect on the NNM while the quadratic term has a softening effect. This is somewhat well known for these SDOF systems but for multi-modal systems it is difficult to interpret the influence of the parameters on the NNMs making this a powerful tool.

Further demonstration is shown in Figure 43, where the gradients are overlayed onto the NNM, represented as first harmonic cosine term versus frequency. The NNMs after perturbing the polynomial terms of the SDOF system are plotted as well. In subplot (a) the perturbation is with respect to the quadratic term, α . The increase in the value of alpha results in an added softening effect of the NNM most noticeably seen by the solution with α perturbed by 500%. This softening is accurately estimated by the gradients computed from the theory developed in the preceding sections. Subplot (b) contains the perturbation with respect to the cubic term, β , where an increase in the parameter has a hardening effect. Once again this is predicted by the gradients developed in the preceding section.

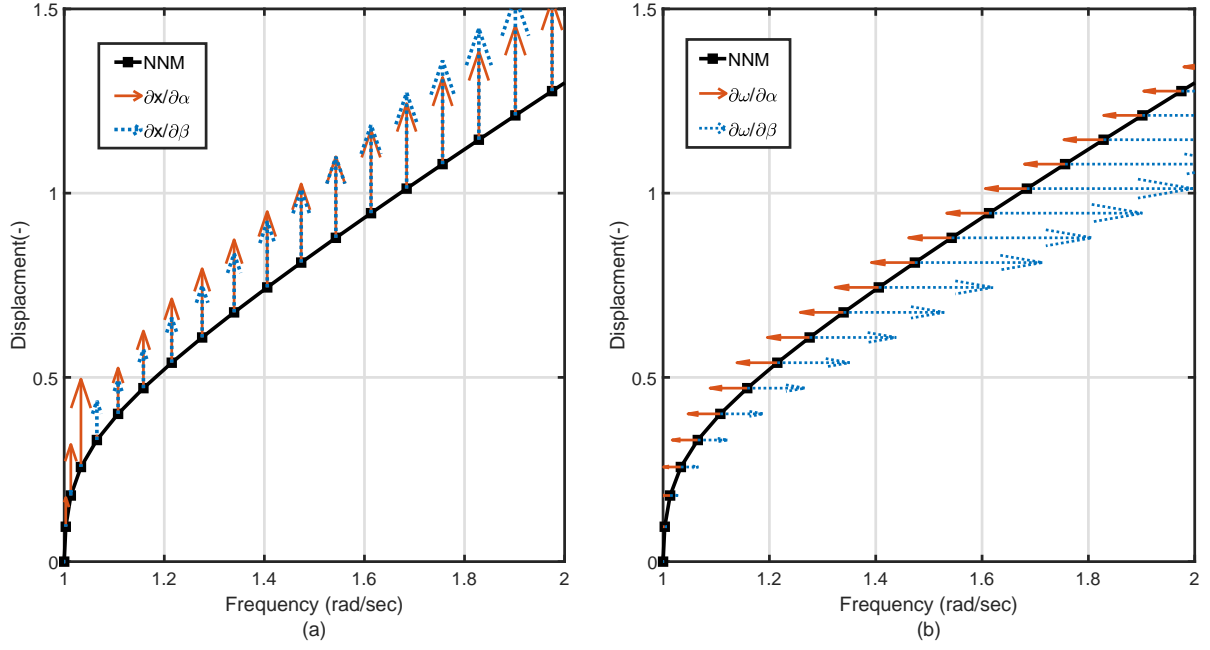


Figure 42: Nonlinear Normal Modes of Case 1 : (a) gradients of the displacement of NNM solutions with respect to ROM polynomial parameters (b) gradient of the frequency of the NNM solutions with respect to the ROM polynomial parameters

Comparison of the gradients of an SDOF duffing oscillator, gradients estimated from finite difference methods and gradients from an analytical single harmonic model are presented in Figure 44. A single harmonic analytic solution of the duffing oscillator is

$$\omega = \left(k + \frac{3}{4}\beta z^2 \right)^{1/2} \quad (83)$$

and taking the derivative with respect to β the gradient of the frequency with respect to the cubic parameter is

$$\frac{\partial \omega}{\partial \beta} = \frac{3}{8} z^2 \left(k + \frac{3}{4}\beta z^2 \right)^{-1/2} \quad (84)$$

Similarly, one can find the gradient of the Fourier coefficient with respect to the nonlinear

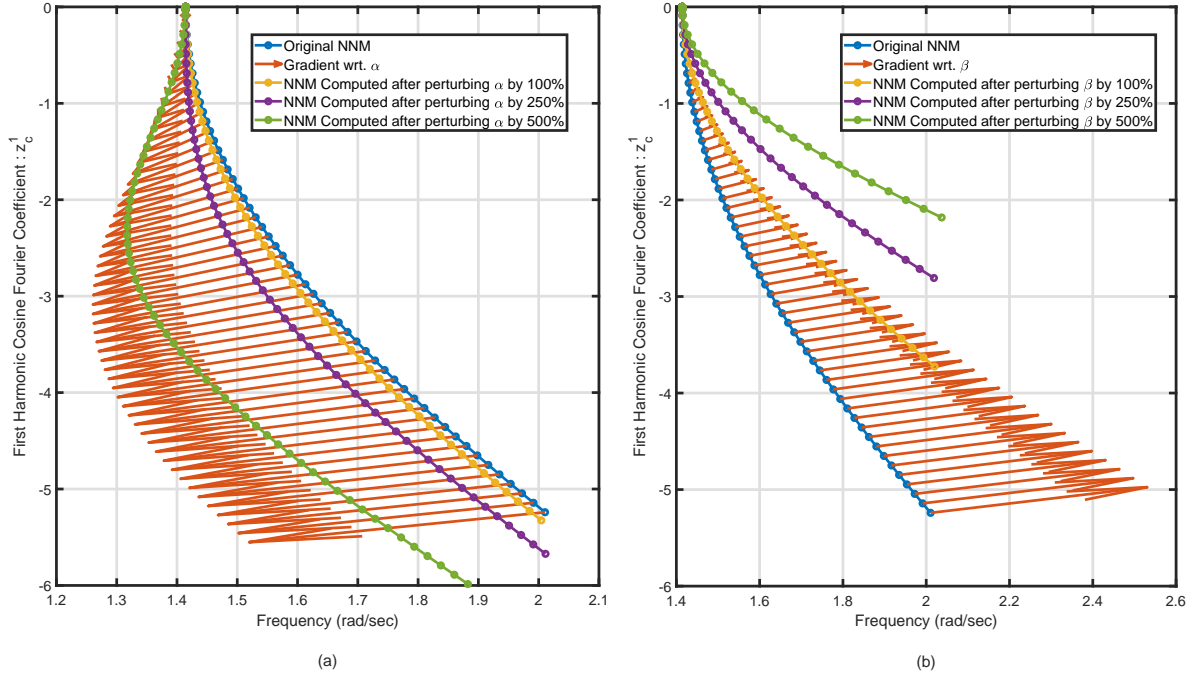


Figure 43: Nonlinear normal mode of an SDOF system, the gradients of the NNM solution and the NNMs after perturbing the polynomial parameters : (a) Gradient of the NNM with respect to the quadratic term α with $\alpha_0 = 0.1$ (b) Gradient of the NNM with respect to the cubic term β with $\beta_0 = 0.1$.

stiffness coefficient to obtain the design sensitivity. Each of the approaches provide the same gradient prediction, demonstrating the accuracy of the MHB gradient derivation in this work for this case.

4.3.2 Finite Element Model Nonlinear Internal Force Gradient

Due to the numerical nature of the finite element method, a closed form solution for the change in the nonlinear internal force changes with respect to the design parameters is not available. Nevertheless once can obtain the gradients in an efficient manner. An important note is that in certain cases this computation is not required, i.e. in the cases where the design parameters only have an influence on the linear properties of the model. An example

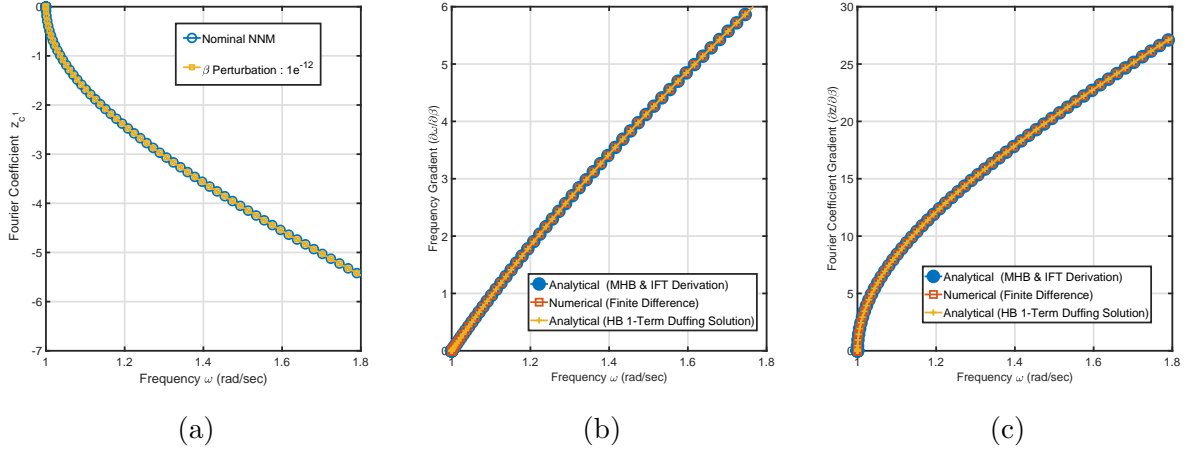


Figure 44: Comparison of the gradients of the SDOF duffing oscillator with pure hardening nonlinearity. (a) Nonlinear Normal Modes. (b) Frequency gradient. (c) Fourier coefficient gradient.

is that of tuning boundary stiffness terms such as the springs in Figure 5 and as will be demonstrated in Section 4.4.1.

The first point to make is that the solution across the period is already known and that the harmonic balance gradients required for the design sensitivity calculations have already been formed and can be saved during the solution procedure. The second point to make is that the procedure can be parallelized very efficiently since each point along the orbit can be computed independently as demonstrated in Section 3.5.4. This is demonstrated in Figure 45 where at each point along the discretized orbit the nonlinear portion of the stiffness matrix must be generated at that displacement followed by a matrix-vector product with the displacement. If reassembling the nonlinear portion of the stiffness matrix at each time and for each parameter would result in $n_p \cdot n_t$ generations of the matrix. This adds a significant overhead to the procedure and is not actually needed. Typically the entire tangent stiffness matrix does not need to be reformed at each step for each parameter gradient. Only the portion of the matrix that the current parameter has an influence on must be updated.

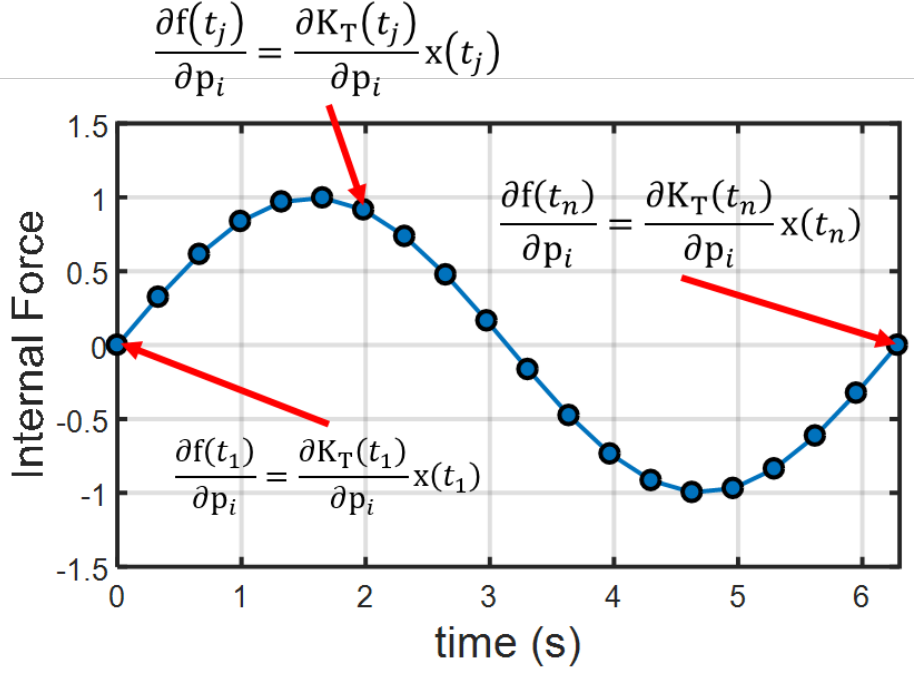


Figure 45: Diagram depicting the computation of periodic orbit time domain gradients.

A demonstration of a gradient computation for a FE model is presented for flat clamped clamped steel beam introduced in Section 3.5.1 where the free variables are the thicknesses of each element along the length of the beam. The gradients of the frequency of each point on the NNM with respect to the thickness of each element are represented as a contour plot in Figure 46. The x-axis corresponds to the frequency or point along the NNM and the y-axis is axial element number. To compute gradient for each solution, 21 in total, with respect to the 40 elements only takes 8.25 minutes using the formulas just derived. The result is interesting in that the NNM frequency increases if material is added around about the 1/6 points (where axial stretching is high), but decreases if material is added at the center.

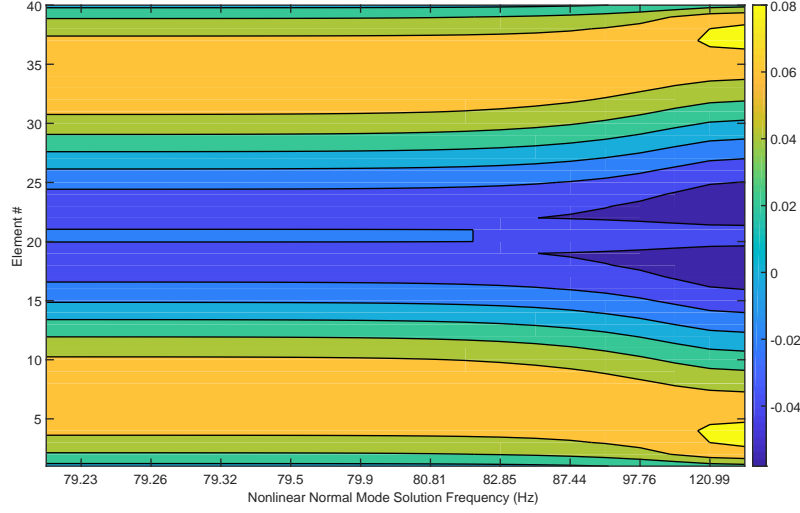


Figure 46: Gradient of each frequency along a nonlinear normal mode branch with respect to the thickness of each element along the beam.

4.3.3 Constraint on Linear Normal Mode Frequency of FE Models

Since the alteration of the parameters of the FE model will influence the linear frequencies of the model a nonlinear constraint is imposed on the optimization problem. In particular an equality constraint is enforced that penalizes deviations of the linear frequency from the value obtained from an experimental low level test. The constraint has the form

$$\mathbf{c} = \begin{bmatrix} 0 \\ 0 \\ \vdots \\ 0 \end{bmatrix} = \begin{bmatrix} \omega_{1,exp} - \omega_{1,num} \\ \omega_{2,exp} - \omega_{2,num} \\ \vdots \\ \omega_{m,exp} - \omega_{m,num} \end{bmatrix} \quad (85)$$

in which \mathbf{c} is a $m \times 1$ vector corresponding to the m modes of interest to be included within the constraint function. This constraint is not limited to only the frequency of the NNM of interest but can contain as many linear frequencies as the user would like to include.

Once again it is best to be able to provide gradients of the nonlinear constraint equation to speed up the computation of the nonlinear constraint rather than allowing the optimization code to compute them via finite differences. The gradient of the eigenvalues of a generalized eigenvalue problem of a FE model according to [98, 99] can be computed using

$$\frac{\partial \omega_{i,num}}{\partial \mathbf{p}} = \frac{1}{2\omega_{i,num}} \boldsymbol{\varphi}_i^T \left(\frac{\partial \mathbf{K}}{\partial \mathbf{p}} - \omega_{i,num}^2 \frac{\partial \mathbf{M}}{\partial \mathbf{p}} \right) \boldsymbol{\varphi}_i \quad (86)$$

as long as there are not repeated eigenvalues. This computation assumes that the eigenvectors, $\boldsymbol{\varphi}$, have been mass normalized. Note that the modal eigenvalue problem is already solved as a starting point for the NNM computation and the gradients of the linear stiffness and mass matrices, $\partial \mathbf{K} / \partial \mathbf{p}$ and $\partial \mathbf{M} / \partial \mathbf{p}$ respectively, are already computed from the gradient computation of the NNM solutions so the additional computational cost of the linear frequency gradient is negligible. The gradient of the constraint equation is simply

$$\frac{\partial \mathbf{c}}{\partial \mathbf{p}} = \begin{bmatrix} -\frac{\partial \omega_{1,num}}{\partial \mathbf{p}} \\ -\frac{\partial \omega_{2,num}}{\partial \mathbf{p}} \\ \vdots \\ -\frac{\partial \omega_{m,num}}{\partial \mathbf{p}} \end{bmatrix} \quad (87)$$

which is a $m \times p$ matrix. In the optimization routines utilized within Matlab [100, 93], the nonlinear constraint violation is typically combined with the objective function to obtain a merit function which is minimized. This at times leads to a solution that violates the nonlinear constraint and as such sometimes requires that the user artificially scale the nonlinear constraint function such that it is weighted higher than the objective function to ensure the

linear frequency is correct.

4.3.4 Solution Selection

To match the solutions between the experimental data and numerical data, the nearest neighbor matching algorithm is utilized because basic interpolation in either frequency or amplitude will not suffice for complex systems that contain a softening-hardening response or internal resonances. The euclidean distances between all combinations of experimental and numerical solutions are first computed. The point with the smallest euclidean distance is then selected and paired with an analytical point and the process proceeds without replacement of the numerical solution, to ensure that numerical solutions are not used twice. A comparison of a basic interpolation approach and the nearest neighbor search algorithm is presented in Figure 47 for a system that has a softening then hardening behavior. The basic interpolation in frequency provides mismatched pairs of solutions, whereas the nearest neighbor search provides more consistent matches. Additional scaling of the solutions, as will be discussed in sections when it has been applied, is at times required to compensate for the difference in scales between the amplitude and frequency components of the curve.

4.4 Application to Reduced Order Models

4.4.1 Flat Clamped-Clamped Beam - Numerical Demonstration

Before trying this on experimental data, it is helpful to test the algorithms numerically. And, there actually are cases in which one would want to do this, for example when one would want to update ROM parameters to match a FE model's NNM. This could be the

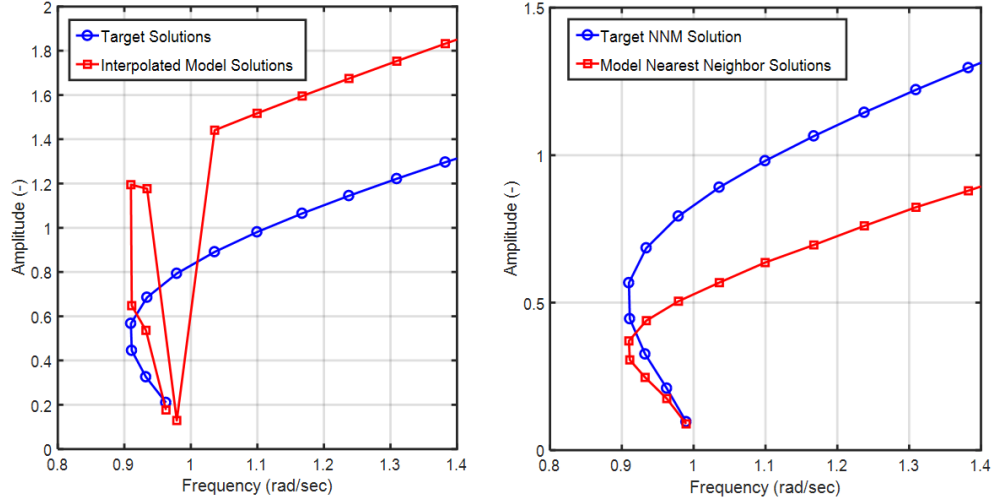


Figure 47: Comparison of linear interpolation in one dimension (left) and solution selection using nearest neighbor euclidean norm without replacement (right).

case in which there is difficulty in creating a ROM using static-force displacement data or if there is uncertainty in the parameters estimated from IC. The example here is applied to the steel flat beam with fixed end conditions introduced in Section 3.5.1. The target NNM data was computed from the full FE model using the AMF algorithm [55] rather than the harmonic balance method, to better approximate data obtained from an experimental test setup which contains all the system harmonics, up to the time step discretization of the integration scheme.

Three ROMs, ranging from single mode to three mode, were updated to match the target NNM data pairs corresponding to the frequency at a point on the NNM and the corresponding displacement at some node in the FEM. The NNMs of the ROMs were computed using the harmonic balance method with three harmonics included within the solution. The initial ROMs were created such that they predict the NNM here poorly. The NNM history, represented as a frequency-energy plot, is presented in Figure 48 showing the target NNM

data, initial ROM predictions and final ROM predictions after updating. The initial ROM predictions are an order of magnitude off in the energy for a frequency when compared to the target data. After the updating procedure, the frequency energy plots are indistinguishable. A quantitative measure of the accuracy increase is represented by the cost function from Eq (64) which is shown in subplot (a) of Figure 49 throughout the updating process. For each case the cost function is reduced by greater than a factor of 100.

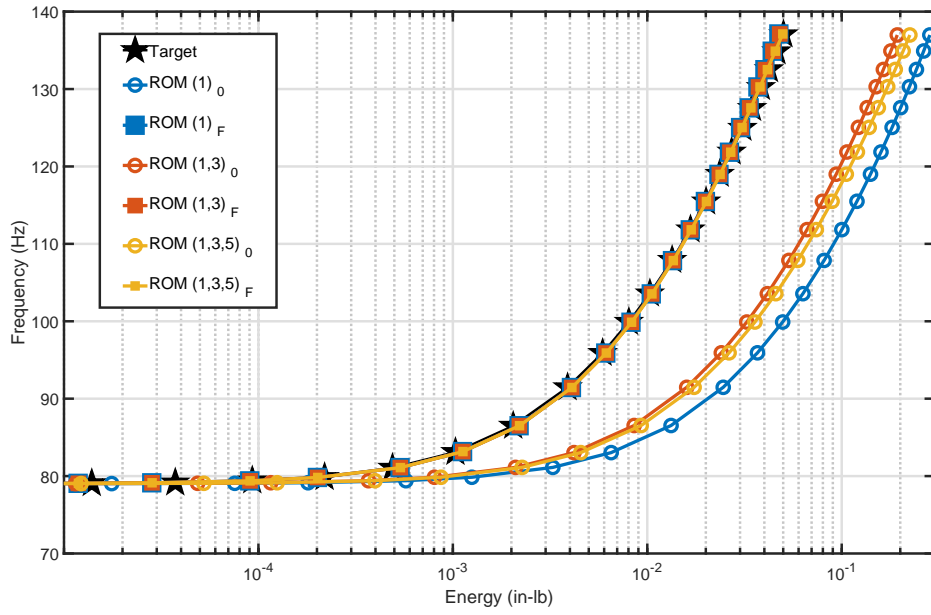


Figure 48: Nonlinear normal mode represented as a FEP of the target data, initial ROMs before updating and final ROMs after updating.

It is known that for the example at hand, and in general for flat structures, that the cubic term of the primary bending mode dominates the response of the system. The evolution of the cubic term of the first mode, $\beta_{1,1,1}$ during the model updating procedure is plotted in subplot (b) of Figure 49. For all three ROMs the cubic term approaches the same value of approximately 4.2×10^{12} .

An interesting example is demonstrated when including an in-plane boundary spring K_x

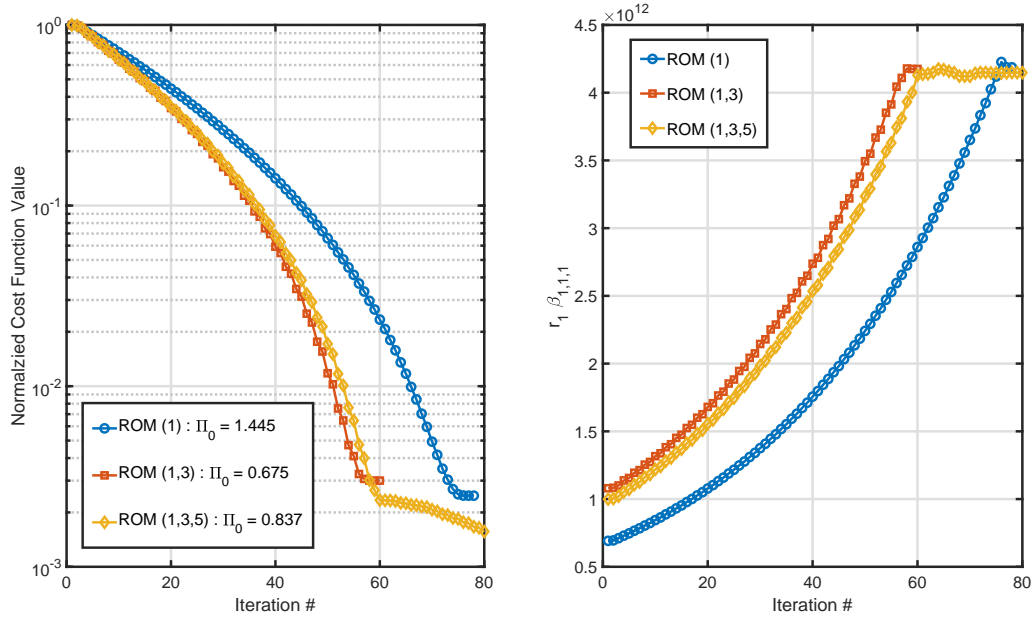


Figure 49: Model updating history. Cost function value history, normalized to initial value, is shown on the left plot. The cubic nonlinear stiffness term, $\beta_{1,1,1}$ of the first mode is shown the right plot.

at both ends of the flat beam presented in Section 3.5.1. This setup is to describe a situation similar to that shown in Figure 5 but shown again here in Figure 50 where it is emphasized that the only unknown parameter is the axial boundary stiffness. The in-plane boundary spring for a flat structure does not have an influence on the 1st natural frequency of the structure because it acts normal to motion of the mode. However it does have an influence on the nonlinear normal mode of the system even though it is only a linear spring. This occurs because the amount of axial stretching the beam is dependent on the relative stiffness of it's boundary.

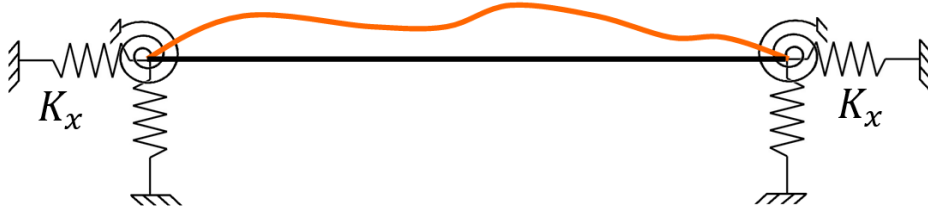


Figure 50: Diagram of a flat beam with unknown axial stiffness terms K_x .

The target data, in this case, are the displacement, frequency pairs along the NNM computed from the full FE model using the MHB method with 5 harmonics included within the solution. Three different sets of target data are generated for axial stiffness terms representing soft, moderate and stiff boundary conditions with values of $K_x = 2 \times 10^4$, $K_x = 2 \times 10^5$, and $K_x = 2 \times 10^6$ respectively. The initial ROM in this example is made from a FE model of the flat-beam with completely fixed end conditions. This initial modeling approach is an overly stiff approximation, but in the case that one does not know the boundary terms it is an adequate starting point. Only a single mode ROM is considered here, comprised of the first bending mode of the beam.

The first nonlinear normal mode of the initial ROM, final ROM after updating and the target NNM are shown in subplot (a) of Figure 51. As the spring value increases, the NNM eventually approaches that of a model with a fixed boundary condition. For the case with the largest axial spring value, $K_x = 2 \times 10^6$, there is minimal change in the NNM between the initial and final model, and this is because the value is nearly approximating a fixed condition. For the other two cases, $K_x = 2 \times 10^5$ and $K_x = 2 \times 10^4$, there is a noticeable change between the initial NNM and NNM after updating. In both cases the NNMs after updating align with the target data. In subplot (b) of Figure 51 the cubic term, $\beta_{1,1,1}$, of

the 1-mode ROM is plotted throughout the updating process. Additionally, the $\beta_{1,1,1}$ term estimated from the IC procedure for each FE model with the correct boundary stiffness term is shown with dashed line. For the stiff case, $K_x = 2 \times 10^6$, the updated model does not get much closer to the estimated IC prediction but stays within the vicinity. The other two cases' cubic stiffness terms have good agreement with the estimated values from the IC model after updating.

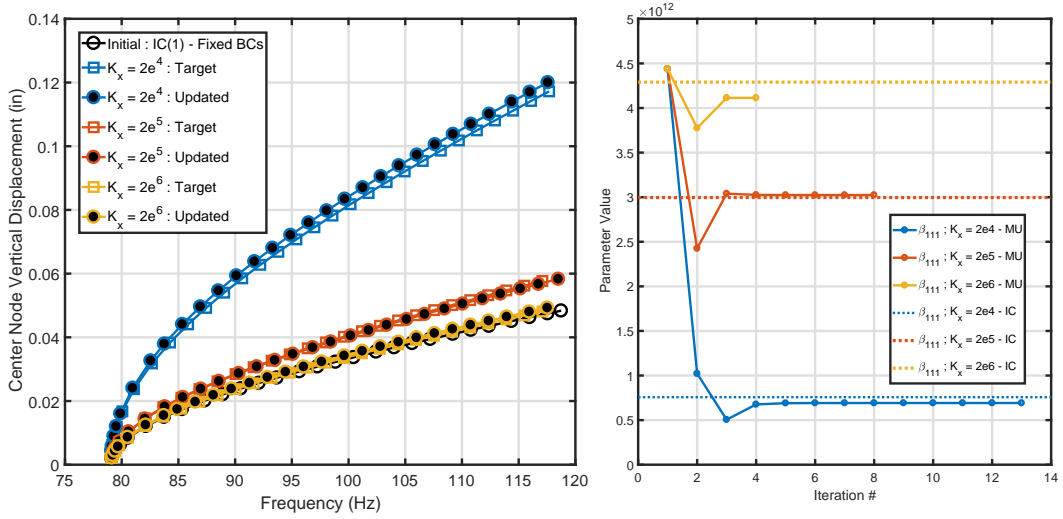


Figure 51: (a) Nonlinear normal modes of initial and final models after tuning ROM parameters. (b) Cubic nonlinear stiffness term during the model updating procedures and coefficients estimated from the IC procedure for each model. In the legend (MU) refers to Model Updating Results and (IC) refers to Implicit Condensation.

An approach such as this may find a lot of application in industry, such as when modeling aircraft panels. There it is attractive to model only the panel of interest, and not have to mesh the support structure and other components, which may require a lot more effort and add a lot of detail to the FE model. This example also demonstrates that it is possible to tune the polynomial parameters of a ROM to capture unknown physical parameters of a structure.

4.4.2 Curved Clamped-Clamped Beam - Numerical Demonstration

To demonstrate the approach on a more complex system, model updating was applied to curved beam. Using the curved beam geometry of Figure 23 as reference, the test structure has length of 139.7 mm, thickness of 1.397 mm, width of 12.7 mm, and radius of curvature of 1905 mm. The beam is made of Polylactide (PLA) with a nominal modulus of elasticity of 3516 MPa, and density of 1248 kg/m^3 . The target data is the first NNM of the structure and was computed using the harmonic balance method with 5 harmonics included within the solution.

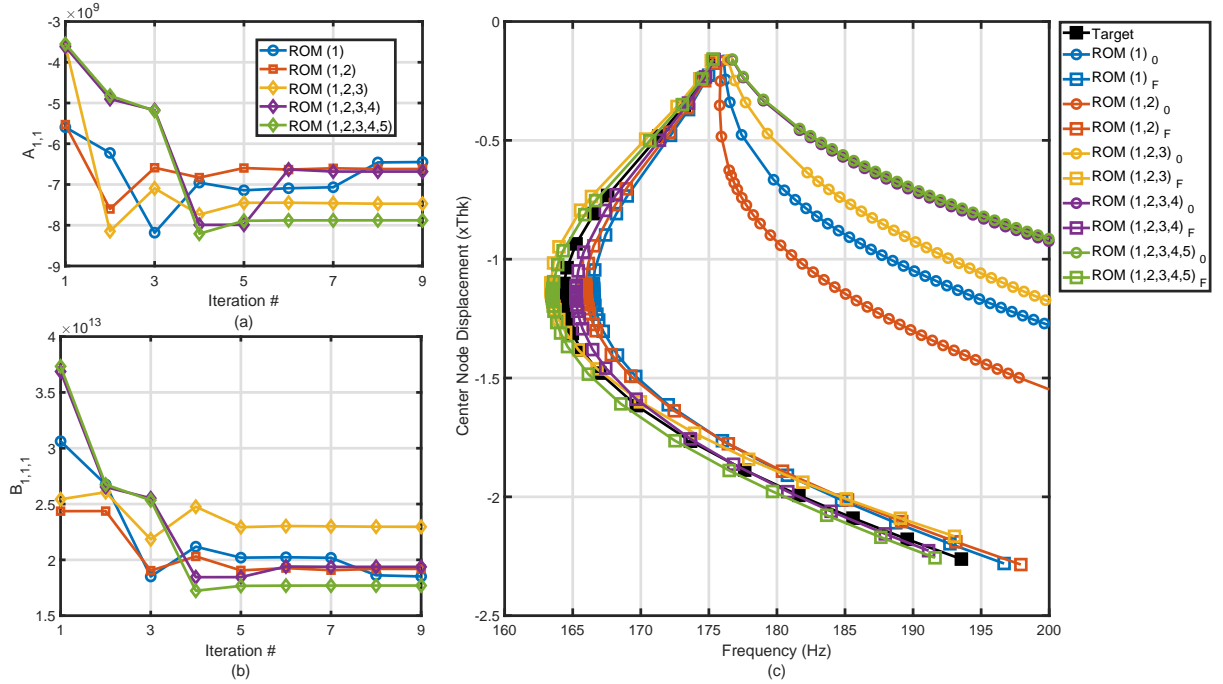


Figure 52: Initial and final Nonlinear Normal Modes of various curved beam ROMs along with the target NNM.

Although for each of the ROMs the final model looks accurate in terms of center node vertical displacement versus frequency, curved structures are known to have an asymmetric response. To evaluate the full field accuracy, the out of plane displacement residual between

the target data and the models are plotted in Figure 53 for the 1 mode ROM and 5 mode ROM. The 1 mode ROM is able to reduce out majority of the residual after updating but there is still a noticeable amount of asymmetric residual left with over 25% error. The 5 mode ROM on the other hand is able to reduce the residual at each point to below 5%.

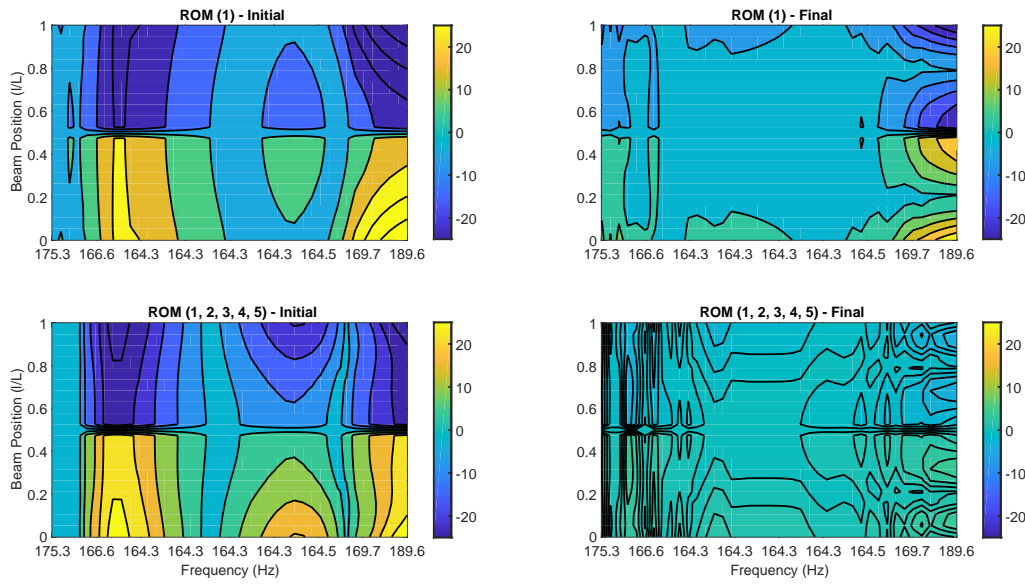


Figure 53: Out of plane displacement residual error between the target data and ROMs.

4.4.3 Flat Plate - Numerical Demonstration

The third numerical study is on a modified version of the RC19 panel from [101] add other citations as well. The panel is made of AISI 4140 alloy steel with dimensions of 254 mm x 127 mm with a thickness of 0.635 mm. The modified version in this case has a smaller mesh size as well as linear spring elements representing the in-plane boundary conditions of the side support structure. The finite element model used to represent the plate is shown in Figure 54.

The acquisition of data in this section will replicate an experimental setup in which

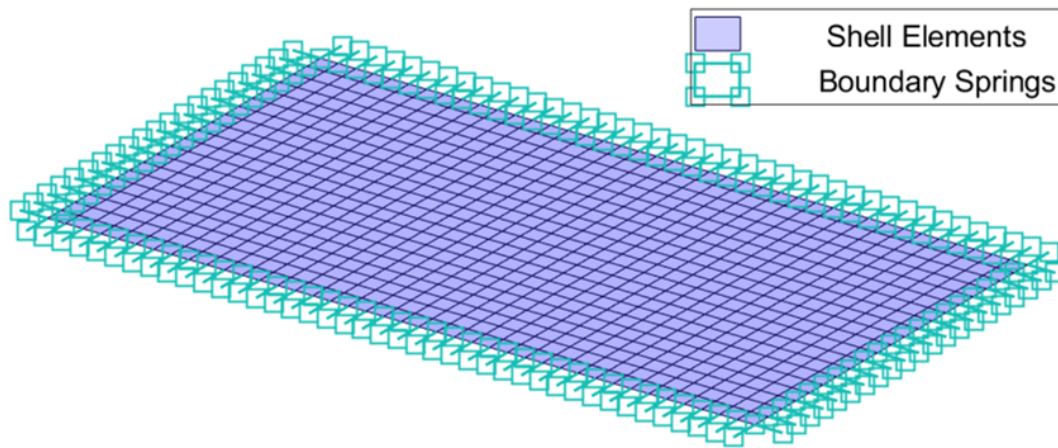


Figure 54: Finite element model of the RC19 panel in which the plate is modeled with 4 node shell elements and the boundaries are modeled with linear axial springs.

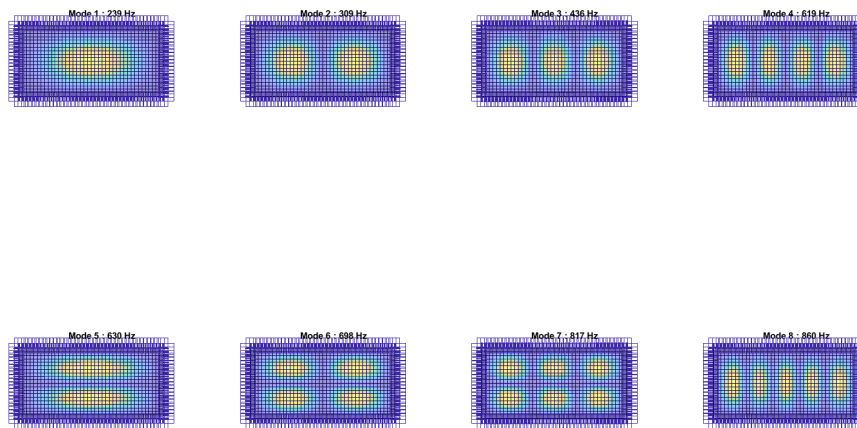


Figure 55: First eight linear normal modes of the flat plate.

only a select set of points are available for model updating. This was used to test the 2D gridded interpolant used within the model updating routine before applying to experimental systems. The grid of points in which the out of plane displacement is extracted from the model and used for updating is presented in Figure 56. This grid represents discrete points

that one may use to extract response using a laser vibrometer as will be discussed in the experimental section.

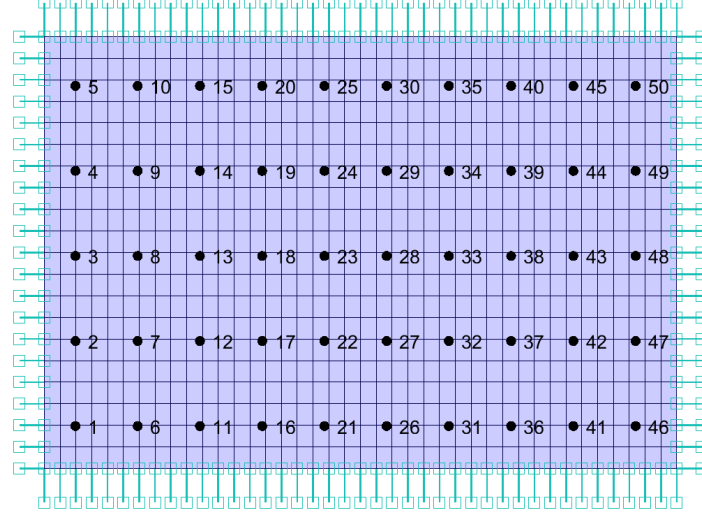


Figure 56: Finite element model of the RC19 panel with the points used to extract results used in model updating.

Two nonlinear normal modes are of interest for this structure, the first and third modes which have a strong coupling between them. Three reduced order models were created to model the flat plate. All three models were created from a FE model with fixed boundary conditions to provide a quick initial estimate of the model. The ROMs nonlinear stiffness terms were then tuned to match the objective NNM computed directly from the FE model of the structure with compliant boundary conditions. The spring value used for each of the springs was $1 \times 10^2 \text{ N/m}$. The target data were the transverse displacement and frequency pairs along the NNM branch with the displacement extracted from the points designated in Figure 56.

The first NNM of the flat plate along with the initial estimates of the three ROMs are

presented in subplot (a) of Figure 57. The SDOF ROM with the first mode included has a stiffer NNM than the target data but after updating is better able to approximate the curve although there is still some error present. The 2-DOF and 3-DOF initial ROMs have a better approximation of the NNM but still required some model updating to come into close agreement with the target NNM.

In this case, we also looked at updating to match the third NNM of the flat plate. The third NNM of the flat plate along with the initial estimates of the three ROMs are presented in subplot (b) of Figure 57. The SDOF ROM with only the third mode included within the basis set under predicts the amplitude for a given frequency. After updating the ROM is able to accurately capture the frequency-amplitude dependence. The 2-DOF and 3-DOF original ROMs were already very accurate relative to the target NNM and the model updating only had a slight improvement on the accuracy of the model.

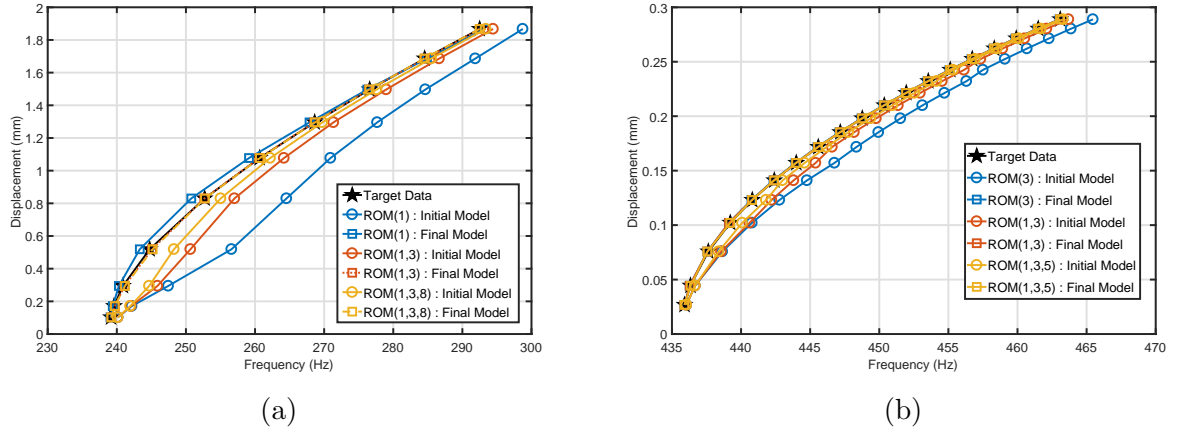


Figure 57: Nonlinear normal modes of the flat plate computed from the FE model and the ROMs' NNMs before and after model updating. (a) First NNM of the model. (b) Third NNM of the model.

4.5 Application to Finite Element Models

The second system of interest is that of correlating properties of a finite element model to match some set of target. A numerical demonstration is first provided followed by application to experimental data.

4.5.1 Boundary Springs of Flat Clamped-Clamped Beam

The first numerical when updating a finite element follows that of Section 4.4.1 where the structure of interest is the steel flat beam with axial springs at the end depicted in Figure 50. In this case the axial stiffness terms are tuned directly on the FE model rather than tuning polynomial terms of a ROM to match the target NNM. The computations of the NNM are done using the FE model. Since the axial stiffness term does not have a contribution to the nonlinear internal force of the system, the gradient of the internal force with respect to the spring does not have to be computed. The only computation in this case is the gradient of the linear dynamic matrix with respect to the spring stiffness represented in Eq 62.

In this case three nominal FE models were created representing extremely stiff, stiff and moderate axial stiffness with values of $K_x = 2 \times 10^7$, $K_x = 2 \times 10^6$, and $K_x = 2 \times 10^5$ respectively. The target data is a FE model with an axial stiffness value of $K_x = 2 \times 10^4$ representing a soft boundary condition. The updating results for the case when starting with a $K_x = 2 \times 10^6$ are presented in Figure 58 with the NNM represented as center node vertical displacement versus frequency.

The normalized cost function history and parameter values during the model updating for all three cases are shown in Figure 59. Overlaid on the parameter history results is

the axial stiffness value of the target NNM data. For each case the model updating routine predicts the correct axial stiffness value.

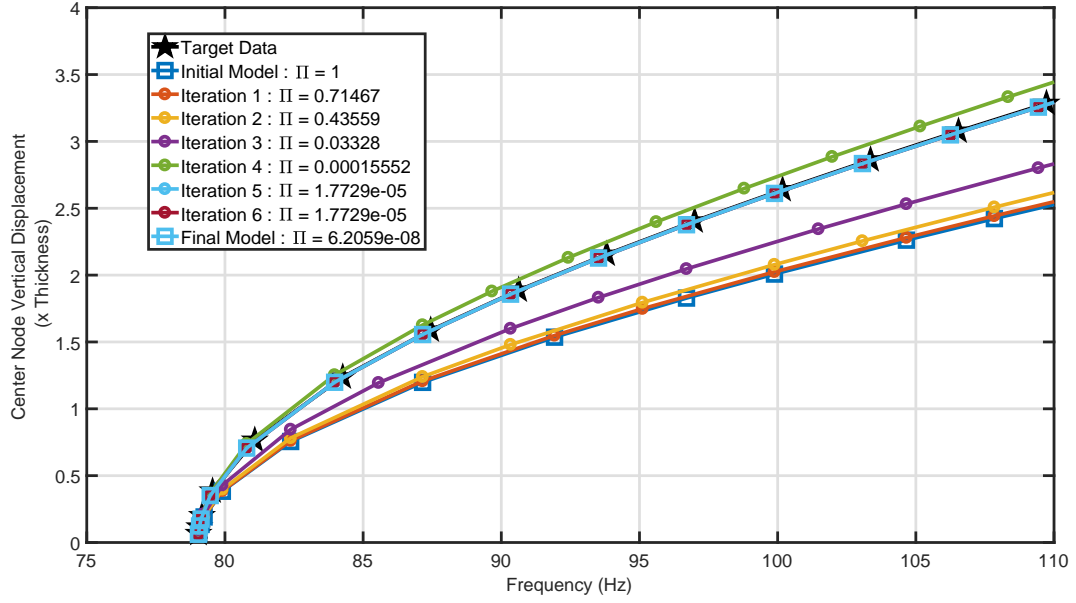


Figure 58: Nonlinear normal mode history represented as center node vertical displacement versus frequency during the the model updating procedure applied to the flat steel beam.

4.6 Recap

The model updating procedure was applied to both reduced order models and finite elements using numerically simulated target NNM data. The model updating procedure was able to produce accurate estimations of the parameters and approximation of the target nonlinear normal modes.

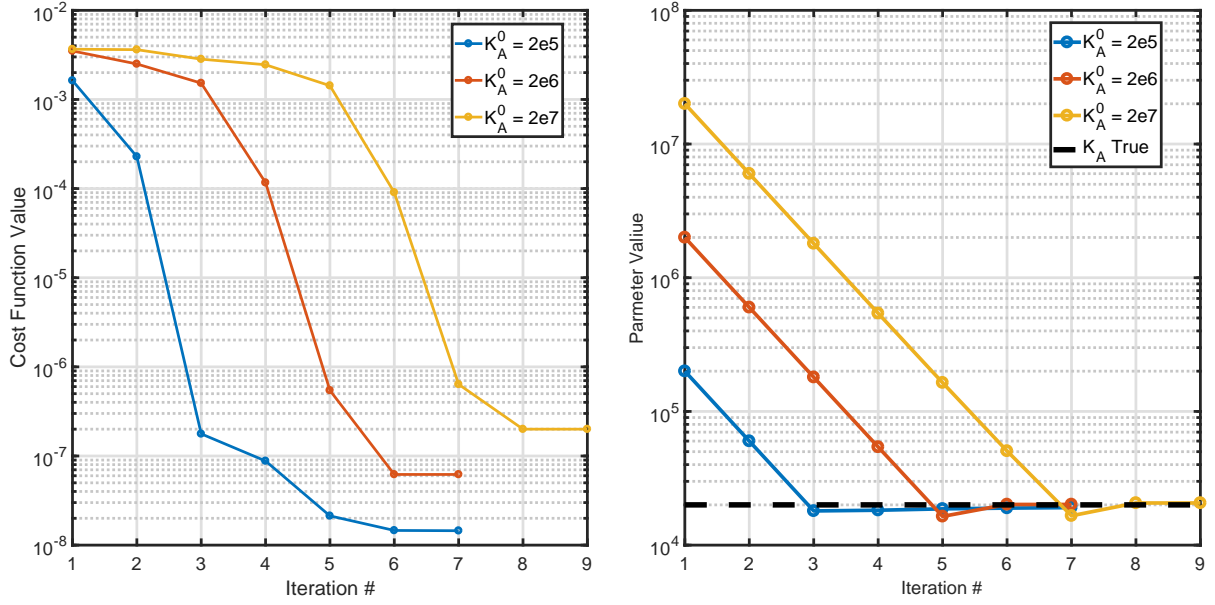


Figure 59: Cost function and in-plane boundary stiffness history during the model updating routine when using different start conditions.

5 Model Updating Applied to Experimental Systems

Model updating is typically used to tune the parameters of a numerical model to match experimental data. This section discusses the experimental data acquisition approach, post-processing of experimental obtained data and model updating applied to experimental systems. Section 5.1 details the experimental acquisition procedure for the two 3D printed beams investigated in this work presented in Sections 5.2 and 5.3. The last experimental study on an exhaust plate used data from the work by [102] and will be discussed in Section 5.4.

5.1 Experimental Setup and Data Acquisition

The identification of nonlinear normal modes of the experimental structure was conducted using a stepped-sine excitation procedure based upon the concept of force-appropriation, to be discussed briefly in the following section. The actual measurements were recorded using a Laser Doppler Vibrometer (LDV) at discrete points along the beam. The advantage of this method is that it is able to obtain near full-field measurements without contacting the structure. The general measurement system is represented in Figure 60 depicting the structure, excitation point and response measurements along the surface of the beam.

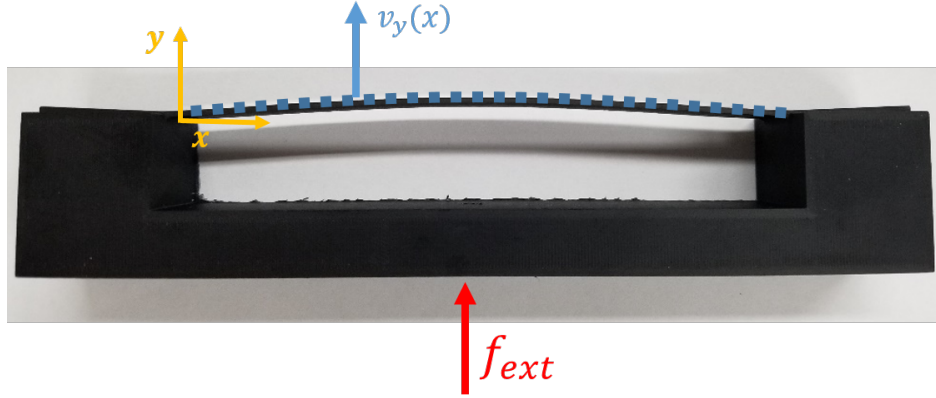


Figure 60: Schematic of the measurement coordinate system indicating the point of excitation and the transverse velocity response measured along the surface of the beam.

The structures are 3D printed from PLA plastic that included both the primary structure of interest, the thin beams, as well as a relatively stiff support structure. The motivation behind this experimental setup is to avoid having to clamp down the primary structure to the base structure. The inclusion of joints can introduce other nonlinearities such as damping into the system. This allows one to focus on the geometric nonlinearity of the system. Furthermore, as 3D printed parts become more common, there is an increased need for model updating methods because the as printed material properties are often uncertain.

The system was excited using a shaker table with a force transducer attached between the tip of the shaker and the base of the beam. The physical test setup is shown in detail in Figure 61 with each of the components called out. The force transducer is necessary to record the input force to identify the NNM accurately using the force appropriation scheme.

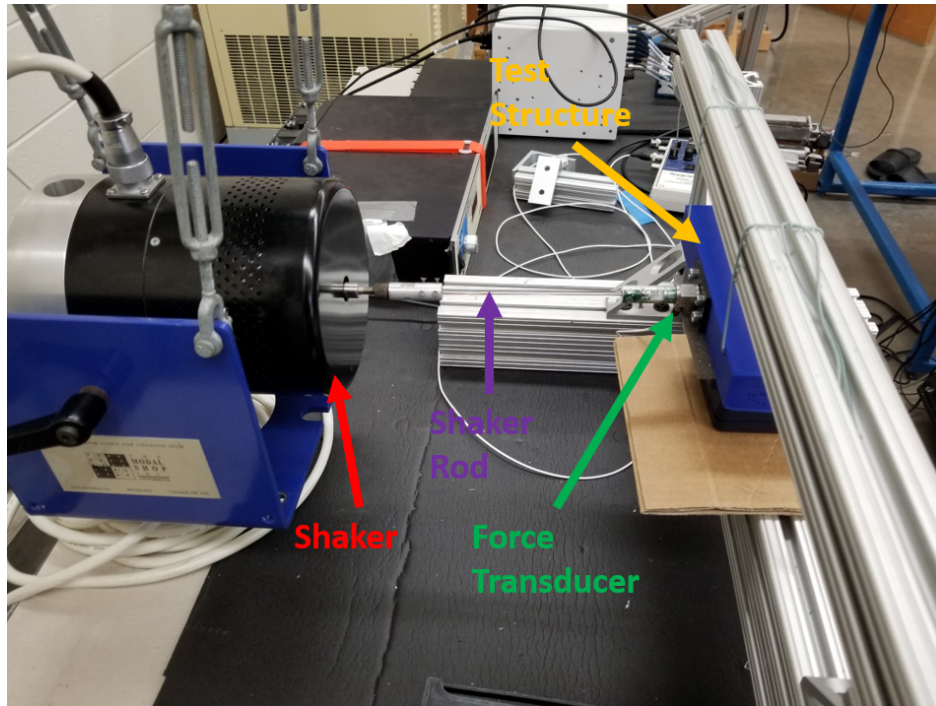


Figure 61: View of the physical setup showing the excitation mechanism of test including the shaker, shaker rod, force transducer and test structure.

The velocity response was recorded along the surface of the beam at discrete points using the LDV, an example is shown in Figure 62. A grid of points is created along the surface of the beam in an attempt to get near full field measurements. The field typically consisted of 26 points along the axial length of the beam and 2 points along the width. Once an NNM solution is found, as will be described in the next subsection, the velocity response is recorded for multiple cycles of the solution at each point on the grid.

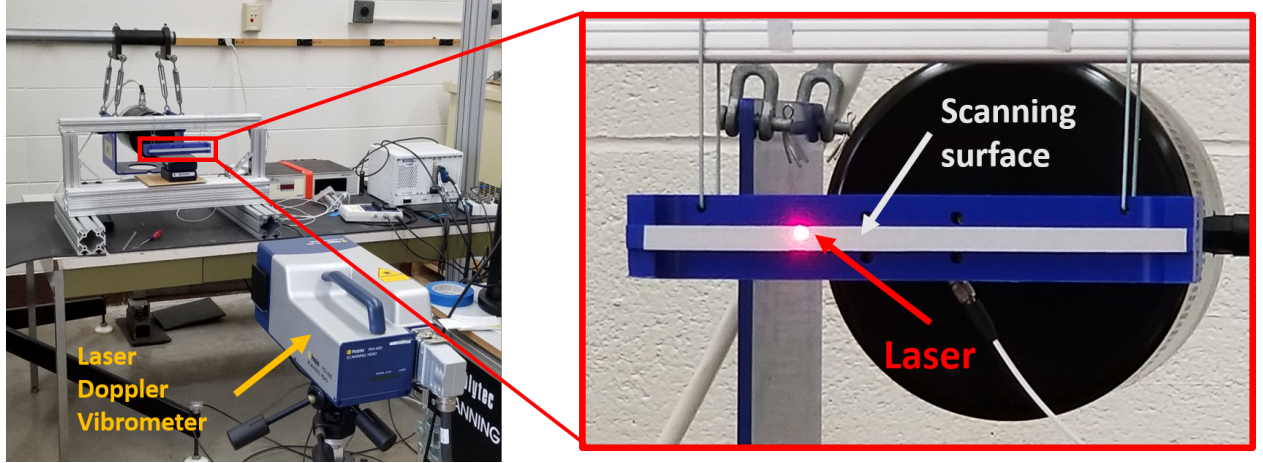


Figure 62: View of the physical setup showing the response recording mechanism of test including the Laser Doppler Vibrometer, scanning surface and laser.

5.1.1 Measuring Nonlinear Normal Modes using Force Appropriation

The method used within this work to experimentally identify nonlinear normal modes is the phase resonance method, which is well known for linear modal analysis, and which was extended to nonlinear systems by Peeters et al. [29]. The foundation of the method is stated simply as an NNM is found experimentally if the force used to excite the structure exactly cancels the damping forces of the structure. This is tied into the concept that a nonlinear normal mode is the periodic motion of the unforced-undamped system, or equivalently a system in which those two sets of forces cancel each other. For the case of linear damping, when looking at Eq (5) this occurs when

$$\mathbf{C}\dot{\mathbf{x}} = \mathbf{f}_{ext}(t) \quad (88)$$

This can be quantitatively evaluated by looking at the phase between the force input signal and the velocity output signal, which is proportional to the damping force. When the phase between the force and the velocity are 180° the system is approximately force appro-

priated. Although the definition uses the term "exactly," the force-appropriation method is only an approximation to the definition due to experimental limitations.

This force appropriation method is used with a stepped-sine procedure to continuously alter the amplitude and frequency of the force excitation such that the velocity and force are 180° out of phase. Once the NNM solution is found then the amplitude can be increased, and the next NNM solution is found. This experimental method has strong analogies with the continuation procedure described to compute NNMs. Furthermore, since the structure is nonlinear, higher harmonics can appear in the response such that one must add higher harmonics to the forcing signal to obtain an accurate NNM solution. For a detailed review of this procedure refer to [103, 31].

5.2 Application to Nominally Flat Beam

This section concerns the application of the model updating algorithm presented in Section 4 on an approximately flat 3D printed beam. The experimental structure was designed to be flat, but due to printing tolerances there are slight imperfections in the beam. The experimental data was acquired and processed via the methods discussed in the previous subsection. The specific beam tested has a length of 177.8 mm, a cross section width of 8.5 mm and a thickness of 2.6 mm. The beam can be seen in the previous section in Figure 61 and Figure 62 being tested. The system is made of PLA whose nominal material properties are a density of 1248 kg/m^3 , modulus of elasticity of $3.1 \times 10^9 \text{ N/m}^2$ and Poisson's ratio of 0.33.

The density and stiffness of the actual structure depends on the infill ratio prescribed

during printing, the specific PLA filament properties, the printer being used and the printer settings. All of these factors lead to uncertainties in the mechanical properties of the 3D printed structures. In particular, there is a large variance in modulus of elasticity with values ranging from 0.0850 GPa to 13.87 GPa [104], and a reported average value of 2.8 GPa. Considering all of these sources, the initial value used in this study was selected to be a value of 3.1 GPa.

5.2.1 Modeling

In aerospace applications, simplified models are often used to limit the element count in an assembly of substructures. Mimicking this case, here the beam was modeled with beam elements and with an axial spring on both ends to represent the stiffness of the boundary. The FE model of the beam is shown in Figure 63 in which the main body of the beam is modeled with 40 2-node beam elements and the axial springs represent the boundary conditions. This is an oversimplification of the structure since there will be some rotational stiffness at the ends, there is some pre-stress in the model due to cooling of the part during printing, and there is some imperfection/curvature in the beam. However, this approach has the advantage of reducing the number of parameters in the model updating to just two parameters, the modulus of elasticity of the beam and the axial stiffness of the springs. Furthermore, these two parameters can be tuned separately since the axial stiffness spring value will only influence the nonlinear response of the bending modes for a flat beam. The modulus can be updated to achieve the correct linear frequency followed by tuning the axial spring to match the nonlinear response.



Figure 63: Finite element model representing the nominally flat beam as flat with axial springs representing the boundary stiffness.

5.2.2 Linear Model Updating

First a simplified linear model updating procedure was conducted to get the first symmetric naturally frequency of the FEM to match with the experimental results. The free parameter of the linear model updating procedure was the elastic modulus since there is uncertainty in the value due to the previously described properties of 3D printing with PLA. The density was not considered a free parameter in this case because the mass of the FE model was in good agreement with the actual mass of the beam. When using the nominal PLA material properties the initial FE model over predicted the frequency of the first linear mode compared to the experimental data which has a frequency of 109.60 Hz. To bring these into agreement, the modulus of elasticity, E , was altered. The initial material properties are compared to those obtained after updating in Table 11.

As stated earlier, there is some imperfection in the beam, and any pre-stress is not being modeled in the FE model, and as such the updated modulus term is accounting for some of these unmodeled features. As more features and parameters are included within the model updating procedure the final modulus term would probably change.

Table 11: Updating of material properties of the 3D printed flat beam to match first natural frequency.

	$E \left(\frac{N}{m^2} \right)$	f (Hz)	$f_{error}(\%)$
Initial	3.1×10^9	133.20	21.09
Final	2.1×10^9	109.63	0.30

The first two symmetric linear normal modes, modes one and three, from the experiment are presented in Figure 64 along with the FE model's mode shapes interpolated to the experimental data acquisition points. Note that the experimental modes have a slight bit of asymmetry that is not captured by the FE model but the modal assurance criteria (MAC) values, which define the similarity between the shapes of modes, between the modes are still above 0.99 for both modes. The high MAC value did not warrant adding in the asymmetry for this modeling approach.

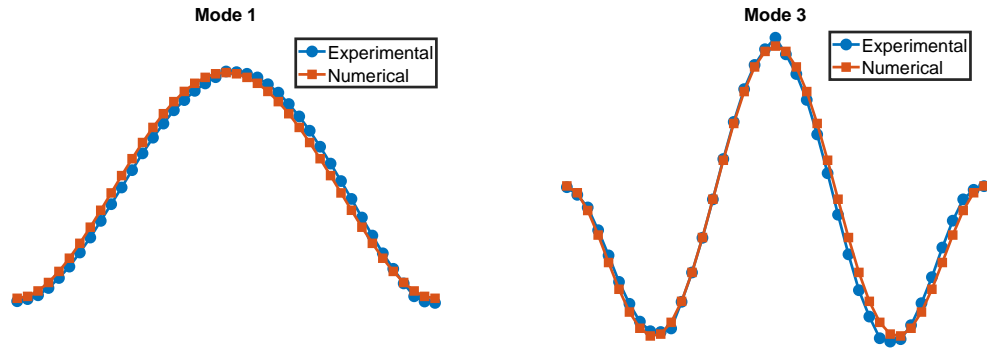


Figure 64: The LNMs identified experimentally from the flat beam and numerically estimated LNMs.

5.2.3 Nonlinear Reduced Order Model Updating

The free parameters of the reduced order model were once again the quadratic and cubic nonlinear stiffness coefficients, α and β respectively. The linear stiffness terms of the ROM, the natural frequencies squared, were kept at a fixed value based on the FE estimations of the linear normal modes, found to be close to the experimental results.

The target set of data used in this case consisted of (modal amplitude, frequency) pairs at various points on the NNM. The modal amplitudes were computed by projecting the full field response measurements onto the modal domain using the experimentally identified

mode shapes presented in Figure 64.

The nominal reduced order model was created from a FE model with fixed boundary conditions, a perfectly flat surface, and contained the updated material properties presented in Table 11. The initial and final NNM of a SDOF ROM containing only the first mode are presented in Figure 65. In subplot(a) the NNM is represented as modal amplitude versus frequency whereas subplot(b) represents the NNM as beam center node displacement versus frequency. The initial ROMs have a significantly stiffer NNM than the experimental results, demonstrated with lower amplitudes for a given frequency than the experimental results. This is expected as the fixed boundary conditions of the FE model are an overly stiff approximation of the structure's boundaries. The updated models, with a single harmonic and three harmonics included, both come into close agreement with the experimental data, while the three harmonic model has slightly better agreement.

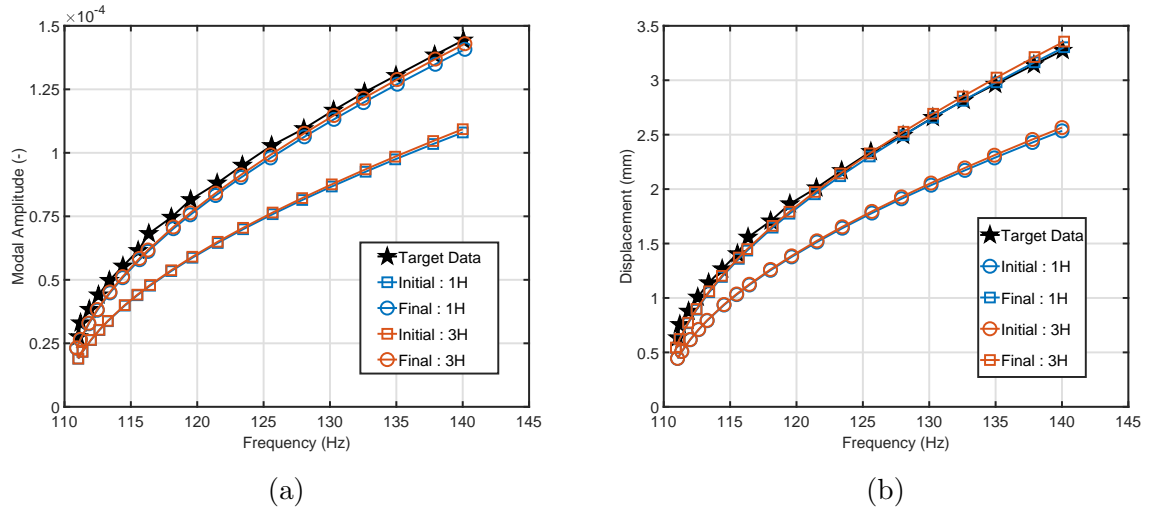


Figure 65: The experimental NNMs of the PLA flat beam test structure along with SDOF models' prediction before and after updating. (a) NNMs represented as modal amplitude of the first mode versus frequency. (b) NNMs represented as beam center vertical displacement versus frequency where the beam thickness is 2.6 mm.

The cost function and parameter values of the SDOF model during the updating routine

are plotted in Figure 66. In each case the cost function is reduced by 30%. The cubic nonlinear stiffness term, $\beta_1(1, 1, 1)$, decreased with respect to the original values for each model. This is as expected, as the FEM has fixed boundary conditions resulting in an overly stiff approximation for the NNM; in the test article there is some compliance in the base support. In essence, the model updating procedure allowed us to skip modeling the side supports and instead use model updating to obtain a ROM that matches the actual response very well.

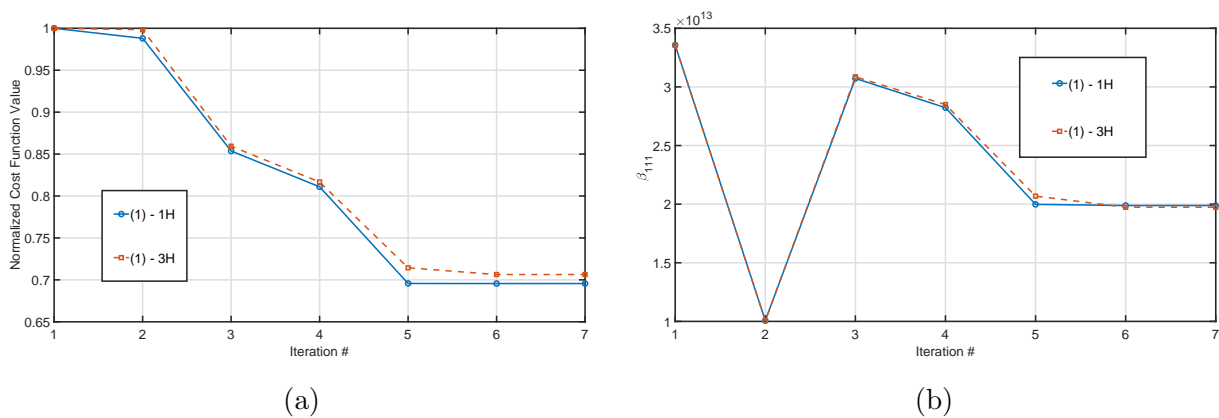


Figure 66: Subplot(a) Normalized cost function during the model updating routine. Subplot(b) The cubic polynomial stiffness term of first mode during the updating routine.

The final NNM predictions between the single harmonic and three harmonic solutions in Figure 65 are nearly indistinguishable. To give a better insight into the accuracy of the updated model, the norm modal amplitude error at each point is plotted in Figure 67. The three harmonic solution is able to reduce the modal amplitude error slightly more than the single harmonic solution. In this case the single harmonic solution suffices to obtain an accurate backbone although for a system with so few DOF the addition of harmonics has negligible computational cost.

Although the SDOF ROM is able to capture the NNM backbone accurately a 2-DOF

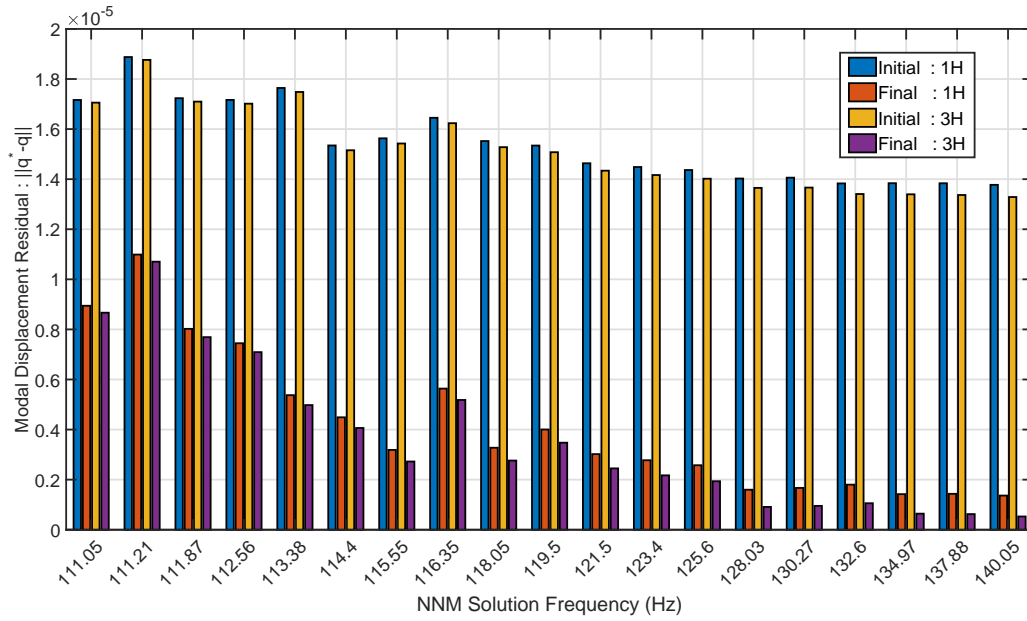


Figure 67: Flat Experimental Beam: Modal amplitude error of the initial and final SDOF models when including only 1 and 3 harmonics in the solution.

ROM, containing the first and third mode of the system, was created and updated to compare with the experimental results. In particular it was of interest to see how well the other modes would be captured by the updating routine, the NNM represented as mode three amplitude versus frequency is shown in Figure 68. Two different solutions are considered, a single harmonic and three harmonics. In this case there is a more noticeable difference in the ability of the solutions to capture the 3rd mode's amplitude along the NNM. It is important to keep in mind though that the third modes amplitude is nearly 2 orders of magnitude less than the first mode and as such the actual gain in accuracy between the single harmonic solution and 3 harmonics solution is negligible.

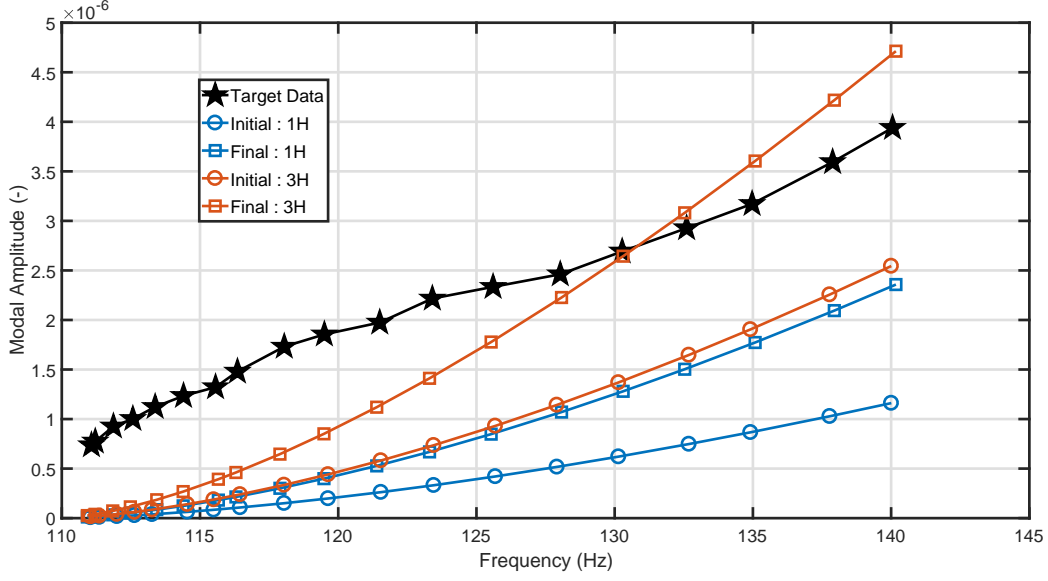


Figure 68: The experimental NNMs of the PLA flat beam test structure along with 2-DOF models' prediction before and after updating. NNM is represented as modal amplitude of the third mode versus frequency.

5.2.4 Nonlinear Finite Element Model Updating

Now it is sought to update the FE model directly so that its NNMs match the experimental data. The free parameters of the finite element model during nonlinear updating are the axial spring values on the end in which a single value is used to control both ends. Note that the axial spring value is a linear parameter but it influences the amount of axial stretching that occurs in the beam and as a result the amount of nonlinearity that occurs. The target set of data used in this case consisted of (physical displacement, frequency) pairs at various points on the NNM. Two initial models were considered, one in which the initial axial spring value was stiff, approximating a fixed boundary condition and one in which the initial value was soft. The NNMs were computed using 3 harmonics included within the MHB procedure. The NNMs during updating for both cases can be found in Figure 69 where the NNM is represented as center beam transverse displacement versus frequency. In

both cases the model updating procedure converges on a model that is able to approximate the NNM accurately.

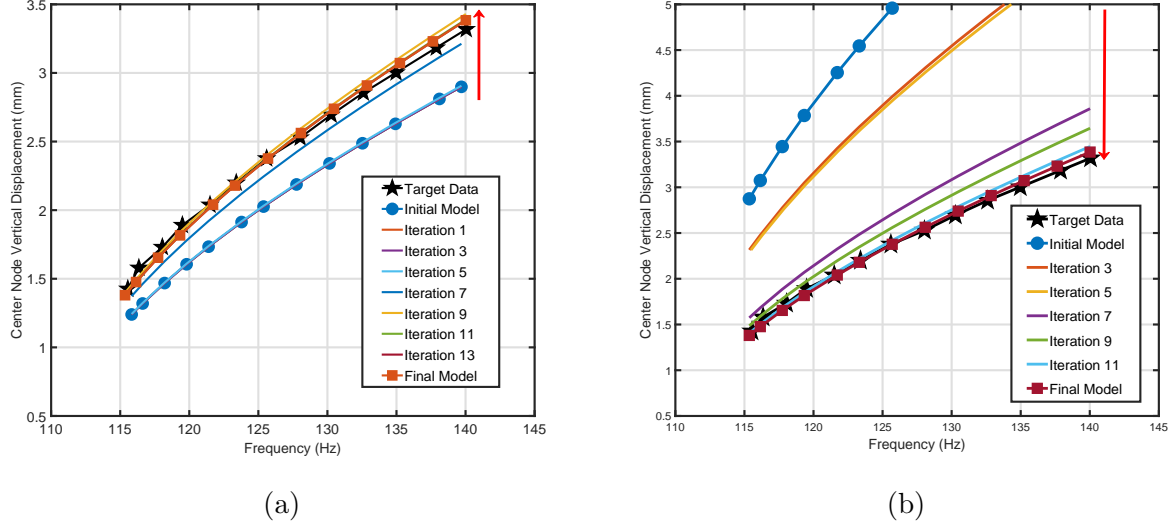


Figure 69: The experimental NNMs of the PLA flat beam test structure along with FE model's prediction during the updating procedure. NNMs represented as beam center vertical displacement versus frequency. (a) Model with initially stiff spring values. (b) Model with initially soft spring values.

The cost function and parameter values of the FE model during the updating routine are plotted in subplot(a) of Figure 70 along with the axial stiffness values in subplot(b). The cost function for both runs approaches the same value and in both cases the cost function is reduced by factor of approximately two. The axial stiffness value shown in subplot(b) of Figure 70 after updating converges to the same value whether using the initially hard or initially soft state providing confidence in the value.

5.2.5 Comparing Final Reduced Order Models

Once the axial stiffness spring values of finite element model were updated to match the experimentally extracted first NNMs it was desired to see if a single mode ROM made

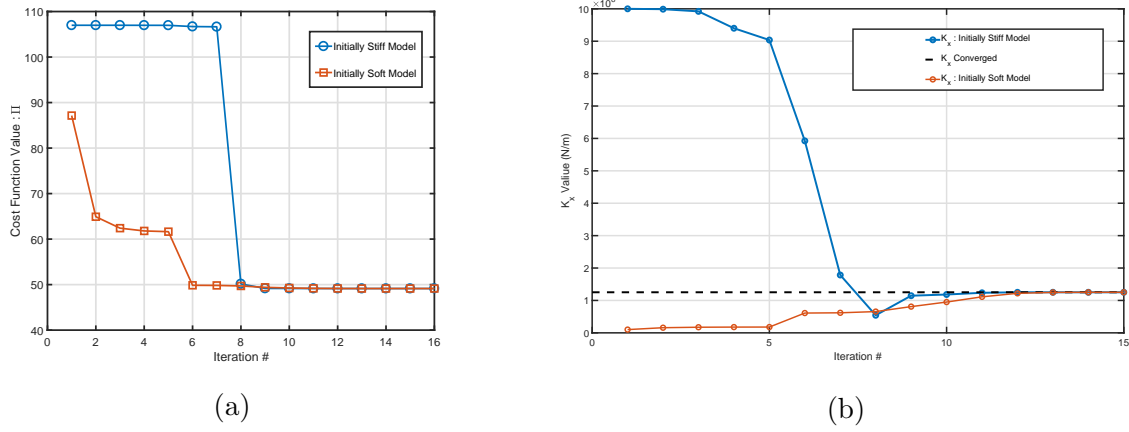


Figure 70: Model updating history of the flat beam. (a) Cost function during the model updating procedure. (b) The axial spring stiffness value during updating.

from the updated FE matched the single mode ROM that was created from the FE model with fixed boundary conditions and updated to match the experimental data. The cubic nonlinear coefficient obtained by the updating the ROM was 1.95×10^{13} , whereas the cubic coefficient identified with the implicit condensation procedure from the updated FE model was 1.80×10^{13} which is only a difference of 8.5%. The values are presented in Figure 71.

Although there is some slight difference in the cubic parameter value, the NNMS of both ROMs provide accurate representations of the experimental NNM. The NNMs, represented as center node transverse displacement versus frequency, of the initial and updated ROM from the fixed boundary condition model along with the ROM created from the FE model with correct boundary conditions are presented in Figure 72. Both the updated ROM model and the model created from the updated FE model provide excellent comparison with the experimental data.

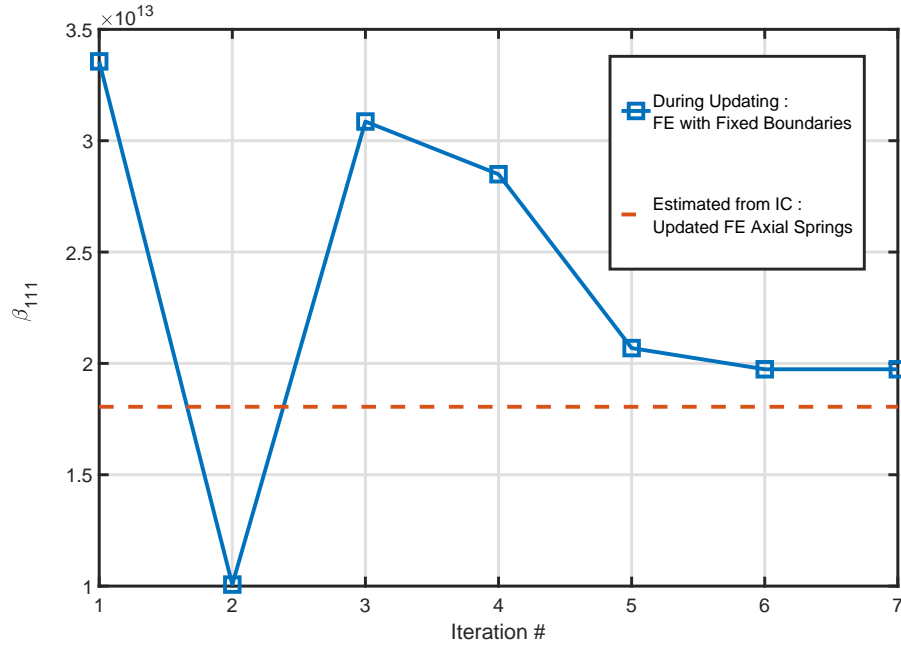


Figure 71: Comparing the cubic coefficient β_{111} of the first mode with the ROM during updating and a ROM made from the updated flat beam finite element model.

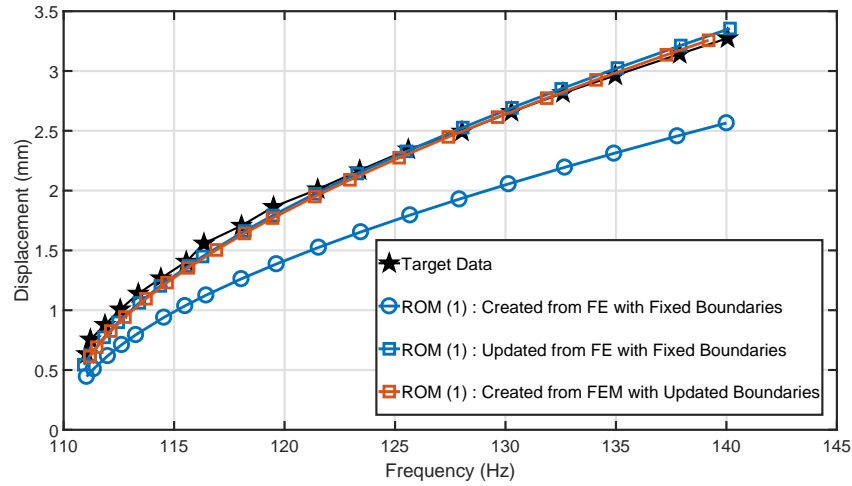


Figure 72: Nonlinear normal mode of the flat beam with the ROM updated from fixed boundary condition FE model and ROM created from the FE model with updated boundary conditions.

5.2.6 Discussion

The model updating procedure was applied to both ROMs and a FE model to approximate the experimental NNMs of the flat beam 3D printed structure. In both cases the models

were able to be updated to better approximate the nonlinear normal mode of the physical structure. In the case of the ROM, a single mode model was able to capture the backbone accurately. The addition of another mode, the third mode, was investigated and was improved somewhat but the contribution of that mode was negligible compared to the first mode.

The axial stiffness of the springs used to approximate the boundary conditions of the structure were tuned to obtain an accurate estimation of the NNM backbone. A final evaluation of both methods was conducted by comparing both the coefficients and NNMs of the ROM from updating and a ROM created from the updated FE model. Both ROMs were able to capture the experimental NNM and contain similar cubic coefficient values with a difference of only 8.5%

Note that although the modeling approach in this section utilized a simplistic approach to reduce the number of free parameters, the model updating procedure could be applied to more complex models. Other potential approaches would be to include torsional springs on the ends to account for rotational stiffness of the boundary, add a slight amount of curvature in the model to present the imperfection or include a pre-stress. Regardless of the modeling approach, the model updating procedure was able to accurately capture the linear and nonlinear behavior of the first mode of the system.

5.3 Curved Beam

The second experimental case study considers updating the parameters of ROMs and finite element models to match the experimentally identified nonlinear normal modes of a 3D

printed curved beam. The specific beam tested has a length of 180 mm, crosssection width of 8.5 mm, thickness of 2.6 mm and a nominal radius of curvature of 3175 mm. The curvature creates a maximum height of the beam of 1.3 mm, or 0.5x the beam thickness. Note that the radius of curvature is designed to be 3175 mm but due to printing tolerances, and expansion after printing this value may not be exact. This slight amount of curvature creates large changes in the dynamics of the structure relative to a flat beam, as will be described in the following section. The beam is shown in Figure 73 for reference. The main beam of interest, the slender beam in the center, is covered with reflective tape to achieve a better reading using the LDV. The ends of the structure that connect to the beam are notably thicker and thus stiffer than the beam of interest and procedures in which to approximate those boundary conditions in a simplified manner will be discussed.

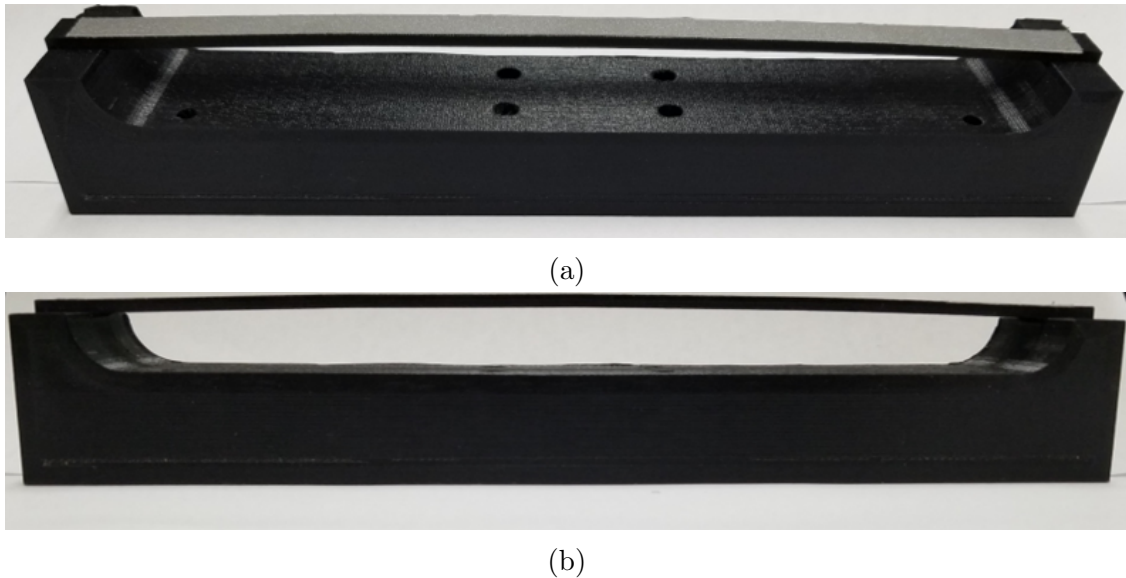


Figure 73: 3D printed beam (a) orthographic view (b) side view

5.3.1 Experimental Data

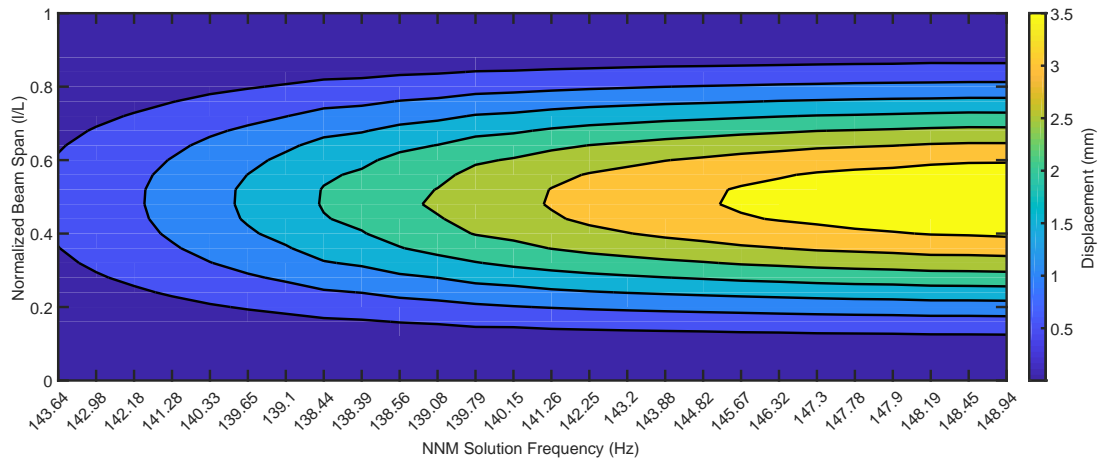
The first two symmetric bending modes (the first and third linear normal modes) of the beam were identified via low level tests. The frequency of the first mode was 144.5 Hz and the frequency of the third linear normal mode was 700 Hz. The experimentally extracted NNM data is presented in Figure 74 including full field displacement data at each point along the NNM in subplot (a) and the beam's displacement versus frequency at the center and quarter span point along the beam in subplot(b). The NNM contains an initial softening, or decrease in frequency with amplitude, followed by a hardening of the system. The shape of the response did not change along the backbone as designated by the contour plot in subplot (a) of Figure 74, in which the response appears to remain in the shape of the first mode.

5.3.2 Modeling

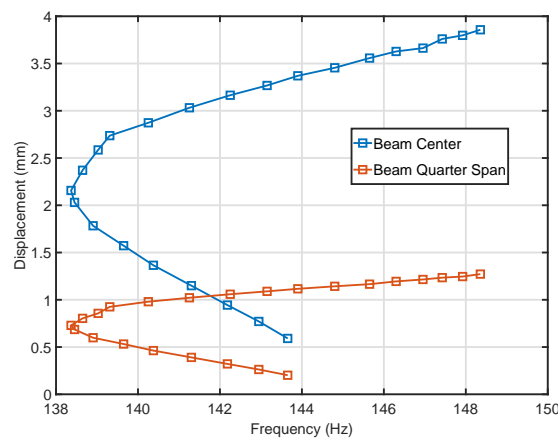
The FE modeling of the structure was conducted using an in-house finite element code in order to perform the nonlinear model updating procedure. The main body of the beam was modeled using 2-node beam elements whereas the rest of the structure, what the beam of interest is mounted to was modeled in a variety of approaches as will be discussed subsequently. The radius of curvature of the beam was controlled via the following equation

$$z_i = \sqrt{r^2 - \left(x_i - \frac{L}{2}\right)^2} - \frac{1}{2}\sqrt{4r^2 - L^2} \quad (89)$$

where x_i is the axial span coordinates of the node, L is the length of the main beam (180 mm), and r is the radius of curvature. The free design parameter is the radius of curvature r which controls the height of each node based on Eq (89).



(a)



(b)

Figure 74: Experimentally identified Nonlinear Normal Modes of Curve Beam. (a) Full field displacement at each point along the NNM. (b) Displacement at center and quarter span of beam versus frequency.

Two different approaches were used to model the boundary conditions of the structure; modeling the boundaries as discrete spring elements and modeling the structure on each side as single vertical beam element. The approaches are demonstrated graphically in Figure 75.

The first modeling approach was chosen because of the simplicity of the parameters to be updated and the ability to control the discrete spring parameters. Furthermore, it is postulated that a majority of the geometrically nonlinear response is limited to the main portion of the structure whereas the side structure maintains a relatively linear response.

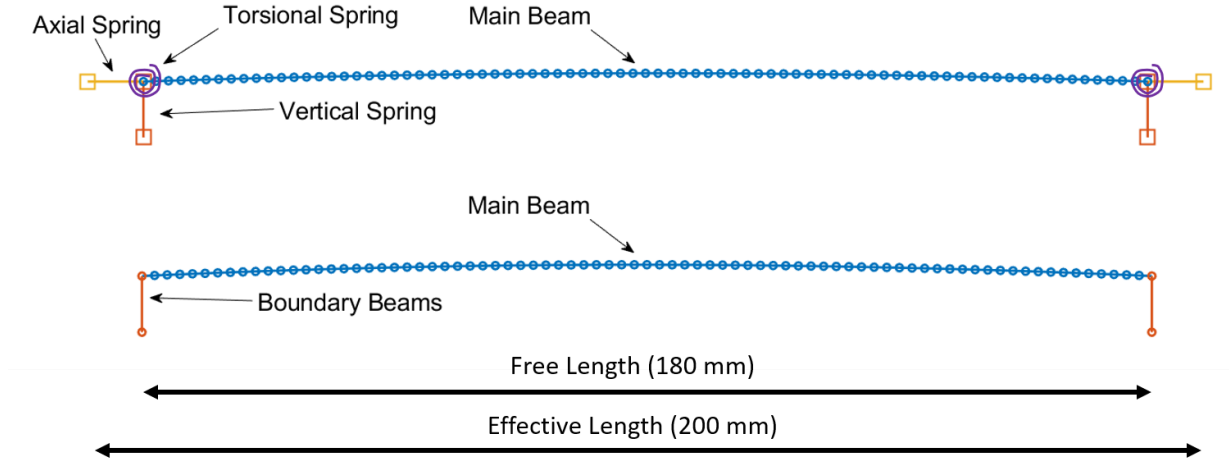


Figure 75: Various approaches investigated into modeling the beam and its boundary conditions; (top) discrete springs at both ends of the free length of the beam, (bottom) single beam element at both ends of the free length of the beam.

An advantage of this approach is that a majority of the free parameters are linear springs which speed up the gradient computation since the gradient of the nonlinear internal force, $\partial \tilde{\mathbf{f}} / \partial \mathbf{p}$, with respect to those parameters is zero and need not be computed.

The second modeling approach is one step more rigorous than the previous because the actual side geometry can be accounted for in the beam element to generate the appropriate stiffness and mass. The free parameters of this model are the modulus of the main beam, the radius of curvature of the main beam, the modulus of the boundary beams and the length of the boundary beams. The reason for having a different modulus for the main structure and the side structure is that during 3D printing there are different infill ratios for the main beam and side beam. The motivation behind including the length of the boundary beam is that it allows for a relative control of the torsional stiffness to axial stiffness of the boundary. This is demonstrated by looking at the linear stiffness of a 2D beam. The bending stiffness term of the boundary beam due to a transverse unit load, which becomes the axial stiffness

at the boundary of our curved beam, is a cubic function of the length of the beam as

$$K_{axial} = \frac{12EI_y}{L_s^3} \quad (90)$$

where E is the modulus of elasticity, I_y is the area moment of inertia about the out of the plane direction and L_s is the length of a beam. On the other hand, the bending stiffness of the boundary beam due to a moment on its end, which becomes the torsional stiffness of the main beam, is

$$K_{torsional} = \frac{4EI_y}{L_s} \quad (91)$$

which is only linear in the length of the beam. By including the length of the beam as a free parameter, the relative importance of these can be accounted for in a single parameter whereas the modulus will scale them the same.

One may question why one would not explicitly model the side structure with 3D elements such as hexagonal or tetrahedron elements. The first reason for not pursuing this approach was that in the in-house finite element code used to compute NNMs using the MHB method currently does not 3D solid elements. From a practical point of view, since the nonlinear response of the main beam is all that is of interest, explicitly modeling the side structures adds significant computational cost to the model updating procedure while adding little benefit. For example, in Figure 76 there is a hexagonal mesh of the side structure which, contains 17985 elements, significantly more than the beam of interest.

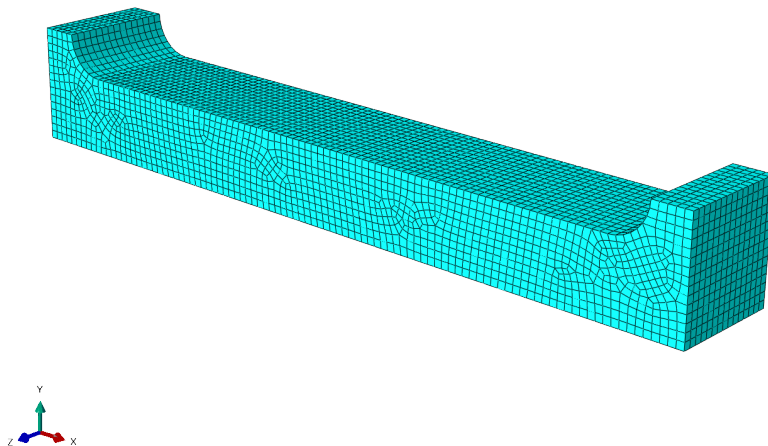


Figure 76: Finite element of the support structure if modeled explicitly with 3D 8-node hexagonal elements.

5.3.3 Linear Model Updating

Prior to nonlinear updating, linear model updating was performed to have a good starting model for the nonlinear model updating procedure. The target data was the frequency values of the first and third linear normal modes extracted from low-level burst random excitation. For the first modeling approach, the first LNM was accurate whereas the third LNM had over 5% error, which after updating was reduced down to less than 1%. The boundary springs had the largest change in parameter values with changes near 50%. The radius of curvature decreased by 20%, which is a fairly large deviation although that only resulted in a change in maximum height of 0.3 mm, with a value of 1.6 mm. The modulus of elasticity, on the other hand, remained relatively unchanged. The initial parameter values and values after updating are presented in Table 12. Although a vertical spring is indicated in Figure 75 for the first modeling approach, the linear modes were insensitive to the spring constant values and are not reported here.

For the second modeling approach the initial frequencies of the model were already accurate compared to the experimental data and model updating only slightly improved the accuracy. The initial parameter values and values after updating are presented in Table 13. The mode shapes, for each modeling approach, corresponding to the experimentally identified linear frequencies are presented in Figure 77.

Table 12: Parameters before and after linear model updating for Modeling Approach 1.

Parameter	Initial Value	Final Value	%Change
Main Beam Elastic Modulus (GPa)	3.100	3.118	0.580
Radius of Curvature (m)	3.175	2.525	-20.482
Axial Spring LH (N/m)	1.000×10^6	1.469×10^6	46.870
Axial Spring RH (N/m)	1.000×10^6	1.438×10^6	43.786
Torsional Spring LH (N-m/rad)	1.000×10^2	1.571×10^2	57.134
Torsional Spring RH (N-m/rad)	1.000×10^2	1.558×10^2	55.828

Table 13: Parameters before and after linear model updating for Modeling Approach 2.

Parameter	Initial Value	Final Value	%Change
Main Beam Elastic Modulus (GPa)	3.100	3.090	-0.316
Radius of Curvature (m)	3.175	3.304	4.059
Support Beam Elastic Modulus (GPa)	3.100	3.098	-0.011
Support Beam Length (m)	0.010	0.010	0.000

Table 14: Frequencies before and after linear model updating for each of the curved beam modeling approaches.

Modeling Approach	Mode #	f_{exp} (Hz)	$f_{num,0}$ (Hz)	$error_0$ (%)	$f_{num,F}$ (Hz)	$error_F$ (%)
1	1	144.50	146.14	1.13	146.00	1.04
	3	700.00	738.55	5.51	699.99	-0.01
2	1	144.50	145.33	-0.57	144.00	0.35
	3	700.00	701.14	0.16	700.00	0.00

5.3.4 Nonlinear Reduced Order Model Updating

The original nonlinear ROMs of the curved beam were created before performing the linear model updating procedure described in the previous subsection. The original ROMS

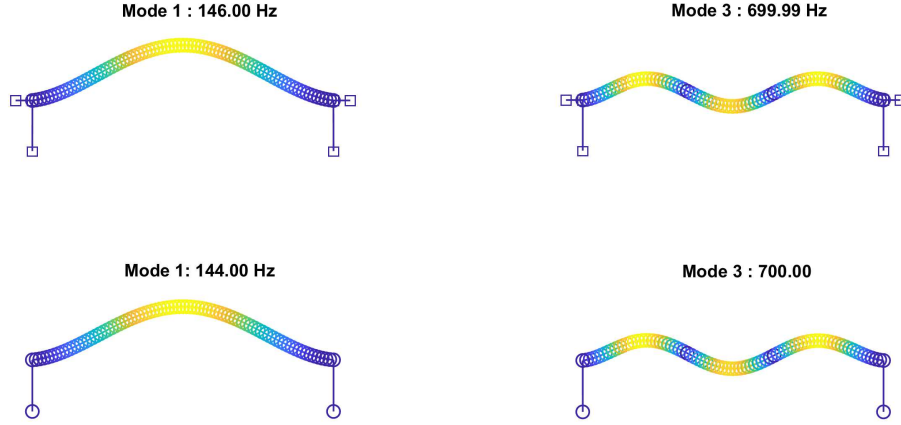


Figure 77: Mode shapes of the curved beam for each modeling approach.

were created from a fixed boundary version of the curved beam with the designed radius of curvature (3175 mm) and the nominal material properties consisting of a modulus of elasticity of 3.10 GPa and density of 1248 kg/m^3 . This model provided a first natural frequency of 145.51 Hz, only a 0.69% error relative to the identified experimental frequency. Since we are going to update the parameters of the ROM to estimate the experimental data this quick approximation and simplification of the model is justified. The target data in this case were the pairs of the physical displacement field and frequency along the NNM branch.

The first ROM that was updated was a single mode ROM consisting of the 1st mode, which has only two free parameters, α_{11} and β_{111} . The results are presented in Figure 78 showing the NNMs during updating, represented as first mode amplitude versus frequency, in subplot (a) along with the quadratic and cubic parameters of the ROM in subplot (b). The initial NNM of the ROM (which came from the nominal FEM) is significantly in error relative to the experimental NNM. The ROM's NNM exhibits no softening behavior. After updating,

the NNM comes into closer agreement but contains some amplitude and frequency error during the initial softening portion of the branch. The cubic nonlinear stiffness coefficient did not change during the updating but the quadratic coefficient increased in magnitude significantly, contributing to the softening behavior of the system.

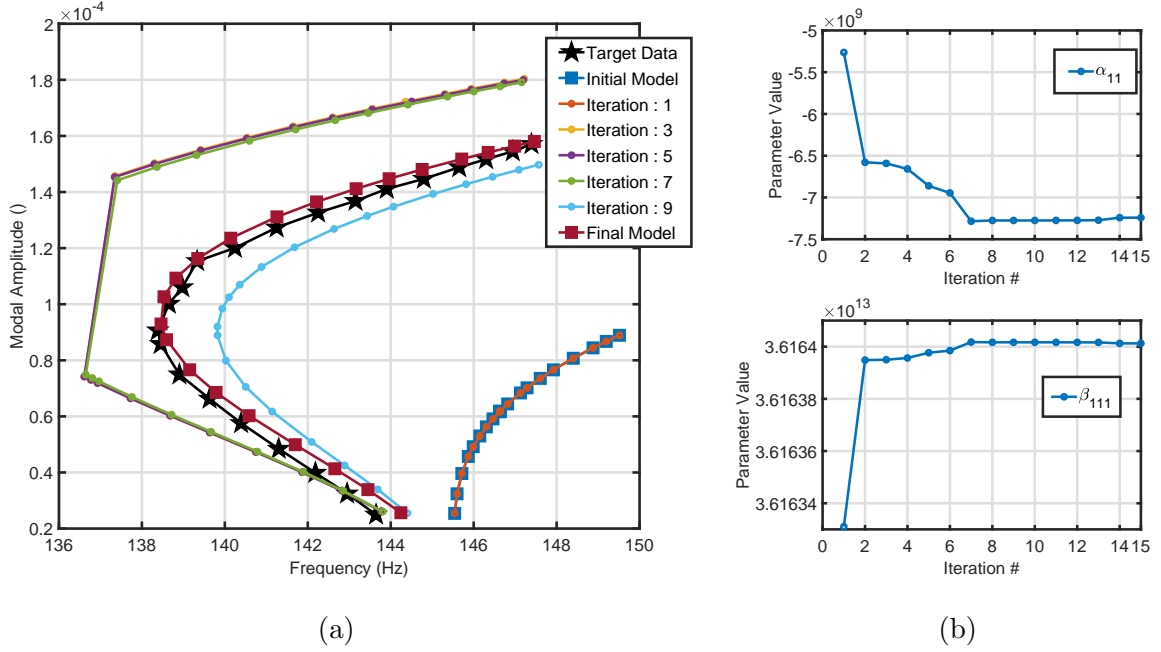


Figure 78: The experimentally measured 1st NNM of the curved beam test structure, represented as modal amplitude of 1st mode versus frequency, along with various NNMs found while updating of a SDOF ROM. (b) ROM nonlinear stiffness parameters during the updating procedure.

The results when updating three different sized ROMs are presented in Figure 79; in each case 3 harmonics were included within the solution. The NNM is represented as transverse displacement of the center of the beam versus frequency. The number of free parameters for the 1-DOF, 2-DOF and 3-DOF ROM are 2, 14, and 48 respectively. The 2-DOF ROM only increases the accuracy of the NNM prediction slightly compared to the 1-DOF ROM. The 3-DOF ROM, on the other hand, is able to better predict the displacement in the high amplitude portion of the NNM compared to the other two ROMs but does not predict the

softening to hardening transition frequency as well.

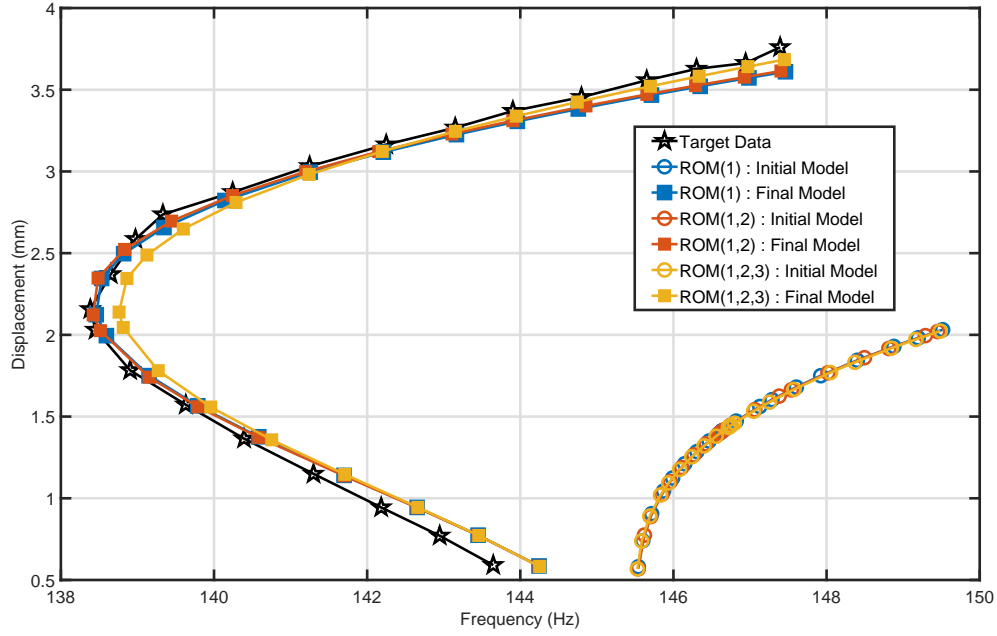


Figure 79: The 1st NNM of the curved beam test structure, represented as center point transverse displacement versus frequency, along with the initial NNMs and final NNMs after updating of a 1-, 2-, and 3-DOF ROM.

The displacement residuals at four selected solutions along the backbone are presented in Figure 80 for each ROM. The additions of the second mode into the ROM does not reduce the residual by much but as the third mode is included, but is a noticeable ability to better capture some asymmetry of the beam's response.

Even though the ROMs are able to follow the experimental backbone softening then hardening trend, there was still some error in the frequency at low amplitudes up into the transition. It was then desired to determine how sensitive the NNMs of the ROMs were to the linear frequency of the system. This was investigated by altering the linear modal stiffness term of the of the first mode, $\Lambda(1,1) = \omega_1^2$, of each of the ROMs before performing the updating procedure on the nonlinear coefficients. For the first step the frequency was set

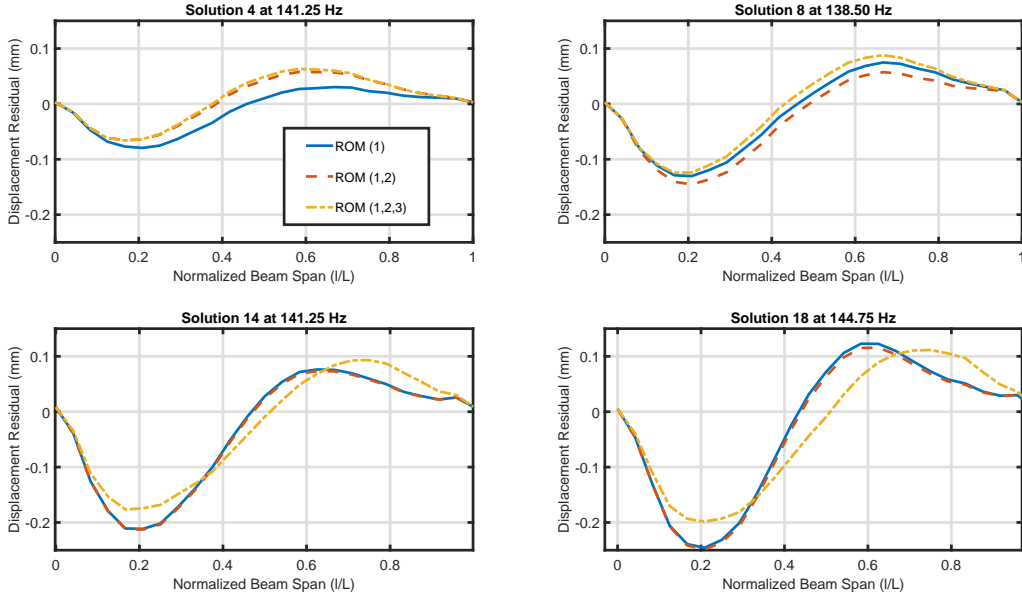


Figure 80: The displacement residual between the ROM NNM solutions and experimental data at selected solutions along the NNM.

to the linear frequency identified from low level experimental test, 144.50 Hz. The results for each ROM with the first mode frequency altered to 144.5 Hz are presented in Figure 81. The NNMs computed from the ROMs are able to follow the experimental NNM fairly accurately but there is still some frequency error prior to the softening of the NNM for each ROM.

Next, the frequency of the first mode of the ROMs was altered to 145.00 Hz, the results for those cases are presented in Figure 82. These NNMs more accurately trace the backbone prior to the softening to hardening transition. The 3-DOF ROM is nearly indistinguishable from the experimental backbone.

The motivation for allowing changes to the linear stiffness of the ROM is that the goal of the ROM is to be able to predict the nonlinear response of the structure. The 0.5 Hz shift is less than a 0.35% deviation from the identified frequency of the first mode from the low

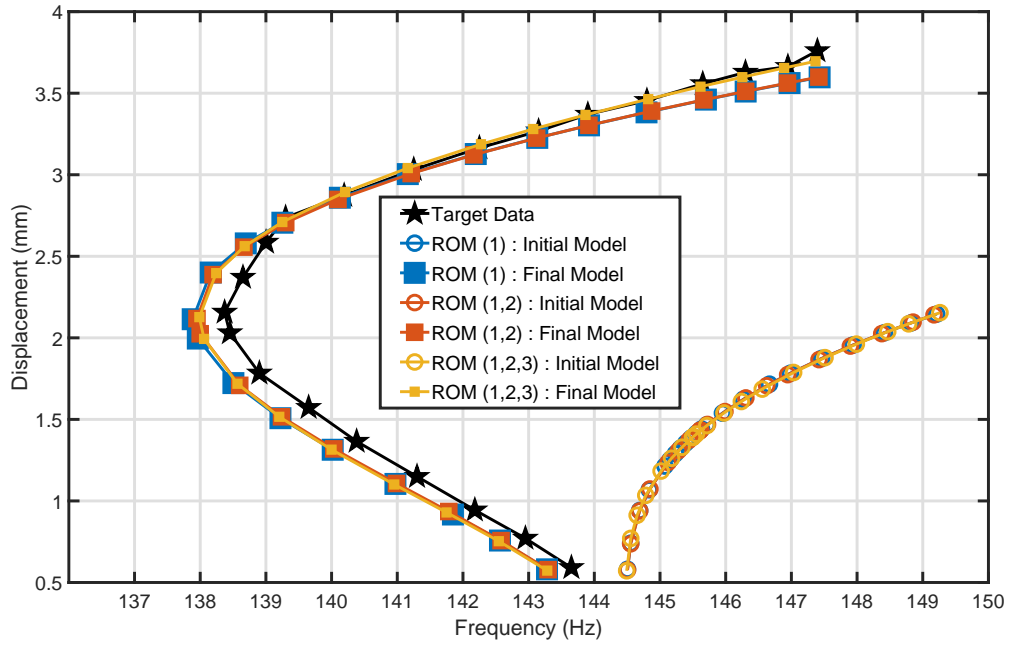


Figure 81: The 1st NNM of the curved beam test structure, represented as center point transverse displacement versus frequency, along with the initial NNMs and final NNMs after updating of a 1-, 2-, and 3-DOF ROM with the frequency of the first mode set to 144.50 Hz.

level test. This is well within an acceptable error bound for linear model correlation and updating.

A numerical comparison of the initial and final objective functions for all three ROMs with the three different frequencies for the first mode considered are presented in Table 15. In each case there is significant reduction in the objective function after updating. Also, as the number of modes increased the final objective function decreased for each case. The frequency that provides the lowest objective function is 145.00 Hz with a value of 0.0668. Interestingly, this is not the frequency identified from the low-level experimental test. This could be attributed to changes in the fundamental frequency of the structure during testing.

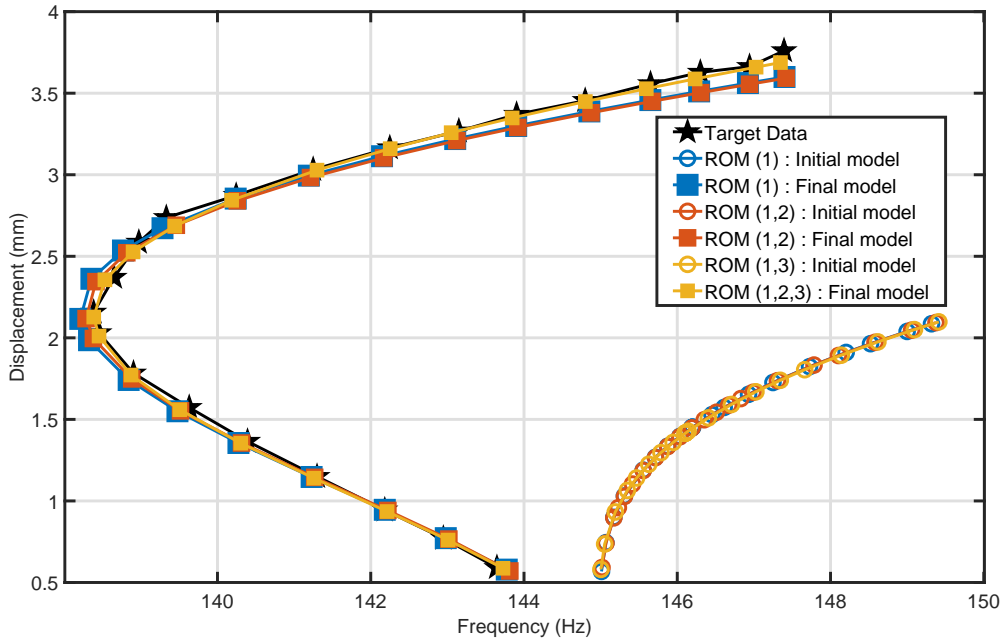


Figure 82: The 1st NNM of the curved beam test structure, represented as center point transverse displacement versus frequency, along with the initial NNMs and final NNMs after updating of a 1-, 2-, and 3-DOF ROM with the frequency of the first mode set to 145.00 Hz.

Table 15: Nonlinear model updating final objective function Π for each of the curved beam modeling approaches.

Linear Frequency (Hz)	ROM Modes	Π_0	Π_F
144.50	(1)	7.4195	0.0955
	(1,2)	7.4410	0.0925
	(1, 2, 3)	7.4547	0.0849
145.00	(1)	8.4140	0.0775
	(1, 2)	8.5710	0.0763
	(1, 2, 3)	8.4280	0.0668
145.51	(1)	9.4960	0.0861
	(1, 2)	9.5292	0.0859
	(1, 2, 3)	11.4954	0.0853

5.3.5 Nonlinear Finite Element Model Updating

After the linear FE model was well correlated to the low level data, nonlinear model updating was conducted. The free parameters remained constant between the linear and nonlinear

model updating, now the objective is to minimize the difference between the experimental curve and the numerically computed NNMs of the models. Additionally, a constraint that the first linear frequency must remain at 144.5 Hz was imposed so that the origin of the NNM would remain at the LNM.

The NNM backbones, represented as center node vertical displacement versus frequency, during the model updating phase for the first modeling approach are presented in Figure 83. The initial model contains a pure hardening response. Throughout the model updating procedure the NNM starts to soften more and more before the hardening transition. The final model is able to predict the general softening to hardening behavior of the experimental NNM but there are still some errors along the branch. In particular the final NNM contains errors in frequency prior to the transition point, and contains amplitude error after the transition point.

The parameters of the model during the updating process are shown in Figure 84 and the final values can be found in Table 16. All of the spring parameters increase in value whereas the modulus of the main beam decreases slightly. This points to the boundaries being overly soft during the linear model updating and the main beam modulus being too stiff. The radius of curvature decreased even more, by 21 %, resulting in a final radius of curvature of 1.983 proving a maximum height of 2 mm, only a 0.7mm change from nominal. The increase in curvature helps contribute to the softening behavior seen in the final model.

In the Figure 85 the NNMs during updating for the second modeling approach are presented. Once again the initial model's NNM contains only a hardening response. After updating the model's NNM contains a softening, in agreement with experimental data, prior to a hardening of the curve which over approximates the displacement for a given frequency.

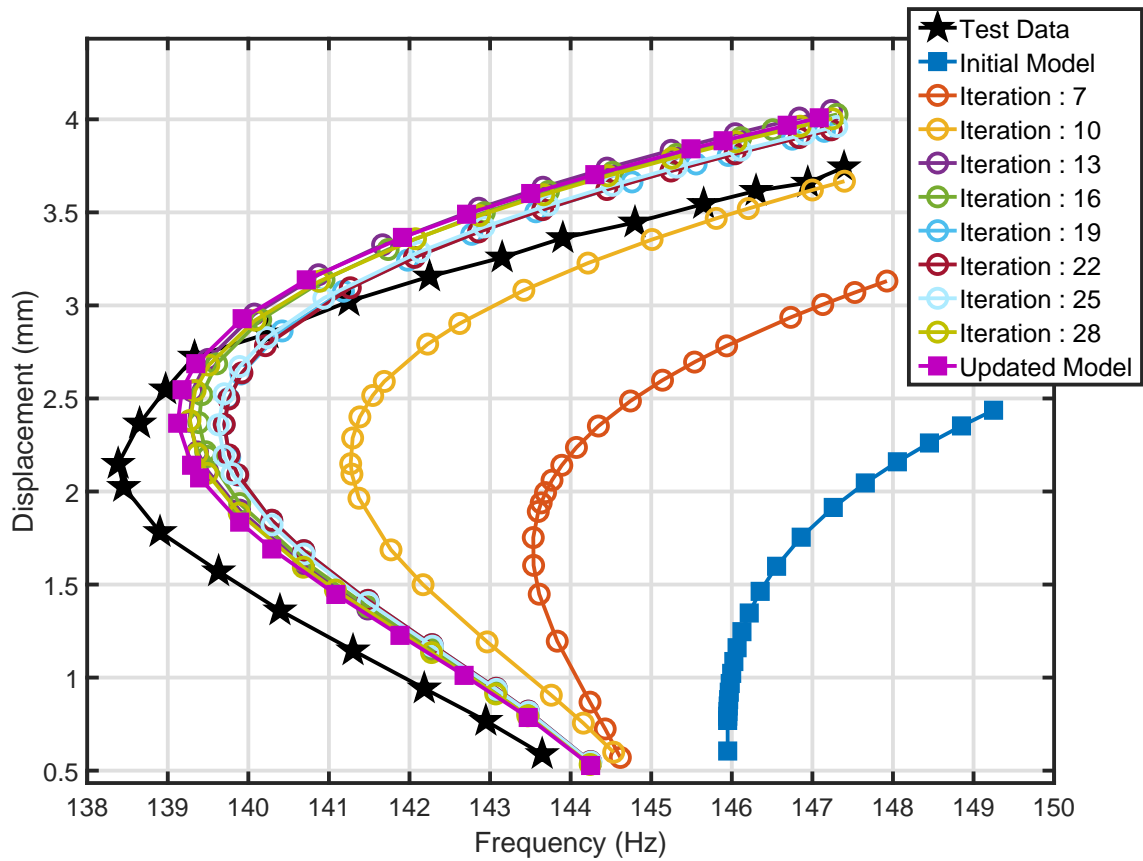


Figure 83: Nonlinear normal modes, represented as center of beam transverse displacement versus frequency, during the model updating procedure for Modeling Approach 1 using springs to represent the boundaries.

The maximum frequency error along the NNM is less than 1.5 Hz for a given amplitude.

The softening to hardening transition occurs at the same amplitude, a value of 2.25 mm.

The parameters of the single beam model during updating are presented in Figure 86 and final values are shown in Table 17. The modulus of the side beam increased during the procedure, which increases both the bending and axial stiffness of the boundary of the main beam. The length of the side beam also increased which decreases the bending and axial stiffness of the boundary of the main beam but at different ratios as described earlier. The modulus of the main beam decreased which reduces the stiffness of the main beam

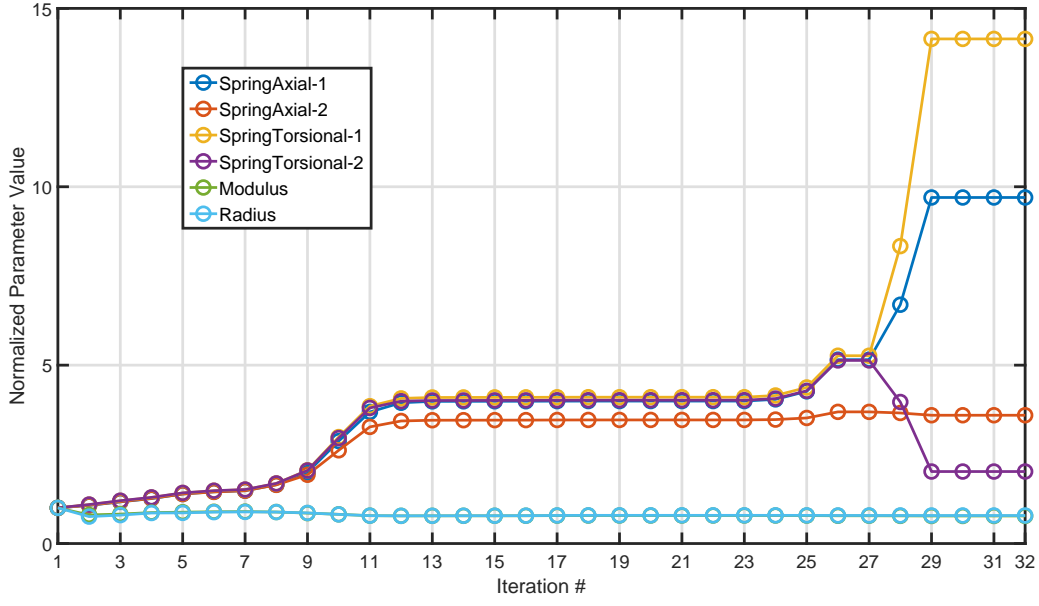


Figure 84: Normalized design parameters during the model updating procedure for Modeling Approach 1 using springs to represent the boundaries.

whereas the radius of curvature also decreased, increasing the maximum height to 1.9 mm, contributing to the softening behavior of the final model.

Table 16: Parameters after linear model updating and parameters after nonlinear updating for Modeling Approach 1. The column % change denotes changes relative to linear model updating value.

Parameter	Linear Updating	Nonlinear Updating	% Change
Main Beam Elastic Modulus (GPa)	3.118	2.411	-22.67
Radius of Curvature (m)	2.525	1.982	-21.47
Axial Spring LH (N/m)	1.469×10^6	1.426×10^7	869.93
Axial Spring RH (N/m)	1.438×10^6	5.170×10^6	359.59
Torsional Spring LH (N-m/rad)	1.571×10^2	2.223×10^3	1414.39
Torsional Spring RH (N-m/rad)	1.558×10^2	3.145×10^2	201.81

A comparison of the final accuracy of the two approaches is presented in Table 18. The table provides the % violation of the linear frequency as well as the initial and final objective function values, defined in Eq (64), for each modeling approach. The objective function from the nonlinear updating for both modeling approaches decreased significantly.

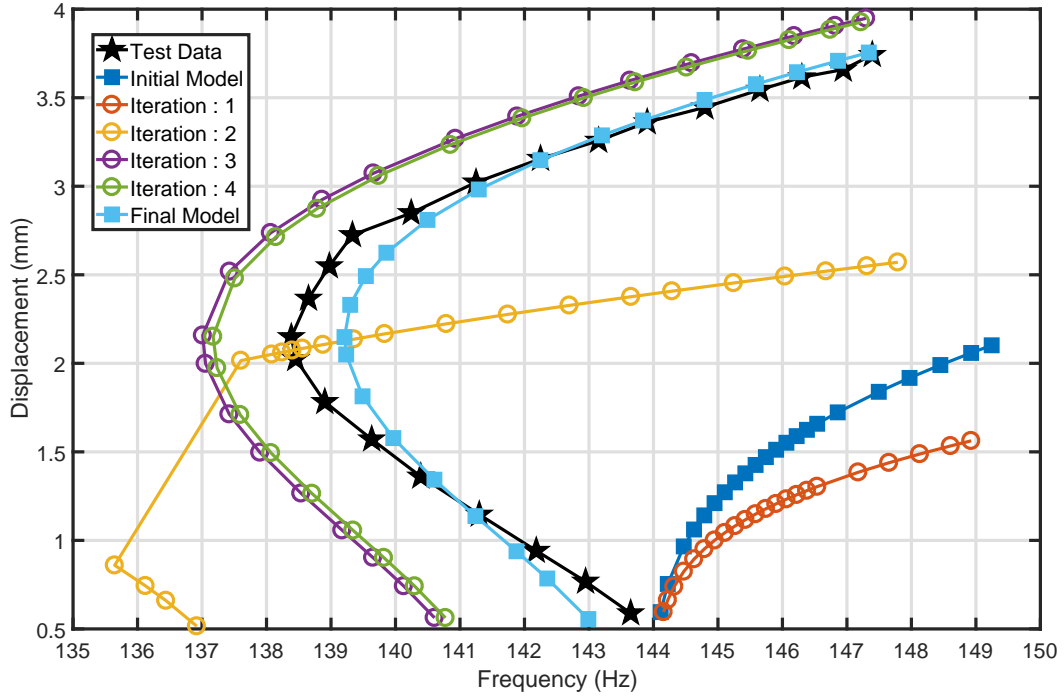


Figure 85: Nonlinear normal modes, represented as center of beam transverse displacement versus frequency, during the model updating procedure for Modeling Approach 2 using a vertical beam to represent the boundaries.

Table 17: Original parameters, parameters after linear model updating and parameters after nonlinear updating for Modeling Approach 2. The column % change denotes changes relative to linear model updating value.

Parameter	Linear Updating	Nonlinear Updating	% Change
Main Beam Elastic Modulus (GPa)	3.090	2.438	-21.10
Radius of Curvature (m)	3.304	2.0810	-37.01
Support Beam Elastic Modulus (GPa)	3.098	3.869	24.83
Support Beam Length (m)	0.010	0.0119	19.49

The linear frequency of the second modeling approach remained accurate, within 0.5% of the experimental. The modeling approach using the beam at the boundary was better able to represent the NNM backbone compared to the spring model based upon the provided cost function value.

It is important to note again that this model updating procedure utilizes a gradient based

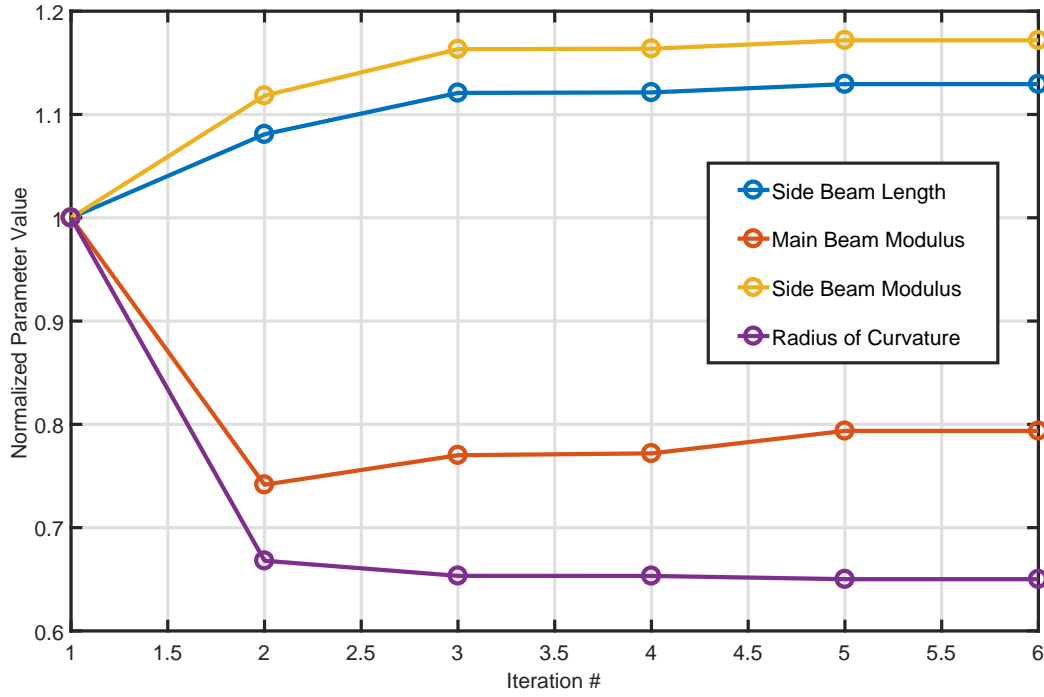


Figure 86: Normalized design parameters during the model updating procedure for Modeling Approach 2 using a vertical beam to represent the boundaries.

optimization procedure and as such only local minimums can be found. It is possible there are other parameterizations of each model that could better minimize the objective function value. These other local minimum could potentially be found by using a global optimization routine or starting the algorithm with different sets of initial parameter values.

Table 18: Nonlinear model updating objective function values results for each of the curved beam modeling approaches after updating and linear frequency error after updating.

Modeling Approach	$f_{lin,exp}$ (Hz)	$f_{lin,num}$ (Hz)	$f_{lin,error}$ (%)	Π_0	Π_F
1	144.50	145.00	0.34	2.865	0.069
2	144.50	143.76	0.51	4.251	0.015

5.3.6 Comparing Final Reduced Order Models

After the two FE models were updated to best match the nonlinear normal mode of the experimental structure, ROMs were created from each model to investigate how well the ROMs approximated the experimental data. A SDOF ROM consisting of the first mode was created from the updated spring boundary condition model and the NNM computed from that ROM is presented in subplot (a) of Figure 87. The SDOF ROM created from the model follows that of the updated model almost identically. A SDOF ROM was created from the updated FE model with vertical beams representing the boundary conditions. A comparison of the NNM of the ROM and the experimental NNM is presented in subplot (b) of Figure 87 along with the initial and final NNMs of the FE model. The ROM produces an indistinguishable NNM compared to the FE model it was made from.

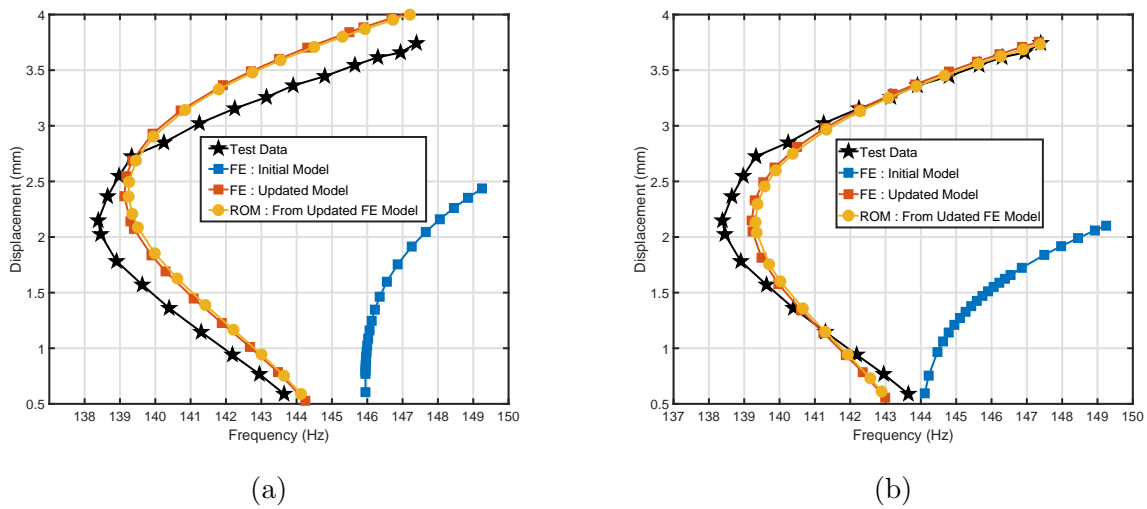


Figure 87: Nonlinear normal modes, represented as center of beam transverse displacement frequency frequency, of ROMs built from updated FE models. (a) FE modeling approach 1. (b) FE modeling approach 2.

The parameters for each SDOF ROM created from the updated FE models and the SDOF ROM updated from the fixed boundary condition model are presented in Table 19.

The ROMs created from the updated FE models contain similar parameters for both the quadratic and cubic terms with a maximum deviation of 7.5% in the cubic term. The ROM created from the fixed boundary condition model on the other hand has a 20% deviation in the quadratic value and a 25% deviation in the cubic parameter from the ROMs created from the updated FE models.

Table 19: Comparison of the SDOF ROM parameters between a ROM that is updated from fixed boundary condition model and the ROM created from updated FE models.

Modeling Approach	$f_{lin}(\text{Hz})$	α_{11}	β_{111}
ROM (1)	145.51	-7.351×10^9	3.617×10^{13}
FE 1	145.00	-6.149×10^9	2.689×10^{13}
FE 2	143.76	-6.126×10^9	2.890×10^{13}

5.3.7 Discussion

The model updating procedure was applied to various modeling approaches to approximate the NNM of a 3D printed curved beam. Both reduced order models and finite element models were updated to the experimentally identified NNMs of a 3D printed curved beam. The curved beams NNMs contained a softening-hardening nonlinearity demonstrating a complex and difficult model updating case study. In both cases, the models were able to be updated to better approximate the nonlinear normal mode of the physical structure.

When updating the ROMs from the finite element model with fixed boundary conditions, each of the ROMs nonlinear stiffness coefficients was able to be tuned to accurately capture the NNM. It was found that a 3-DOF ROM with modes one, two, and three included within the basis set provided the most accurate prediction. Furthermore, when altering the linear frequency to a value of 145.00 Hz, the 3-DOF ROM had the highest accuracy. This

frequency value deviated slightly, less than 0.3% from the frequency identified from low level experimental test.

Two different FE modeling approaches were explored to represent the experimental structure and both linear and nonlinear updating were applied to them. In all three cases the linear models were able to be tuned to match the linear frequencies of the model. Nonlinear model updating, using NNMs, was then performed for each modeling approach. For each case the initial NNMs of the model were significantly off, they contained a pure hardening NNM which is not present in the experimental NNM. After updating the error in each modeling approach significantly decreased and the final NNMs of each approach better approximated the experimental NNM. The FE approach that used beams to represent the support structure of the beam provided the best NNM results after updating with a maximum frequency error of less than 1 Hz along the entire branch.

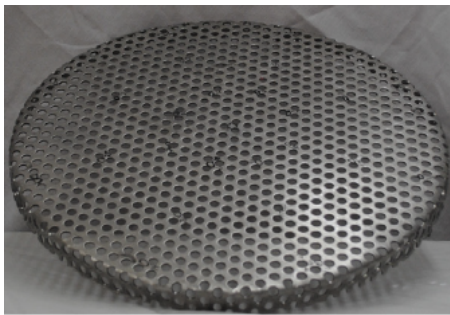
A computational cost comparison is provided in Table 20 for each of the FE modeling approaches and the three ROMs updated. The two FE approaches which do not explicitly model the beam support structure only take two to three minutes to compute both the NNMs and gradients. The NNM computation for the ROMs take less than a minute, and this is conservative since extremely small step sizes were used in those NNM computations. The cost to compute the gradients of the ROMs are all negligible with less than a second for even the 3-DOF ROM.

Table 20: Comparison of the computational costs associated with computing the NNMs and gradients at each iteration of the model updating routine.

Modeling Approach	NNM (sec)	Gradient (sec)
FE 1	134.09	115.56
FE 2	166.17	160.58
ROM (1)	7.78	0.07
ROM (1,2)	15.28	0.13
ROM (1,2,3)	23.95	0.18

5.4 Exhaust Cover Plate

The last experimental system considered is a circular perforated plate that has been studied in the past [102, 31]. The plate, which is nominally 16 gauge (1.52 mm) thick 409 stainless steel, contains circular perforations in an equilateral pattern. An image of the structure is shown in Figure 88. The edges of the plate are bent and welded to a vertical bent steel strip as shown in subplot (b) of Figure 88. The nominal diameter of the plate is 317.5 mm with the bent portion approximately 12 mm and vertical strip of 89 mm.



(a)



(b)

Figure 88: Photos of the exhaust plate studied in this section (a) perforated plate portion only (b) perforated plate welded to steel strip

5.4.1 Modeling

The exhaust plate is modeled in an in-house finite element code, in order to perform linear and nonlinear model updating more efficiently. The perforated plate structure is modeled with 4-node shell elements that represent the main plate, bend radius and lip. The holes present in the top portion of the plate are not explicitly modeled but are accounted for by reducing the modulus of elasticity of the parent material which will be discussed in the next section. The vertical steel plate that the plate is welded to is not explicitly modeled but is rather represented with radial boundary springs on each of the boundary nodes, all with equal spring constants. The FE model can be found in Figure 89 denoting the main structure modeled with shell elements and the side plate modeled with spring elements. The circles on the top portion of the mesh are used to represent the nodes that are used to interpolate the FE NNMs onto the measurement points used in the experiment. Additionally, the physical location of those nodes are controlled by the radius of curvature of the plate. The equation that those nodes follow is that of a spherical cap. In [102] it was found that there is slight curvature present in the structure, identified by using digital image correlation (DIC) of the plate surface. In [102] they directly incorporated the DIC field into the model, in this work instead we will model the top plate as a spherical dome controlled by a radius of curvature parameter that is included within the model updating process as a free parameter. This simulates a situation in which DIC measurements are not available or one in which adjusting the curvature according to DIC was not sufficient to bring the model into agreement with

measurements. The equation that defines the vertical position of the node, z-axis position is

$$z_i = z_{base} + \sqrt{r^2 - x_i^2 - y_i^2} - \sqrt{r^2 - R^2} \quad (92)$$

where x_i and y_i are the in-plane coordinates of the i^{th} node, R is the radius of the plate (158.8 mm), z_{base} is the baseline height of the structure and r is the radius of curvature of the spherical dome.

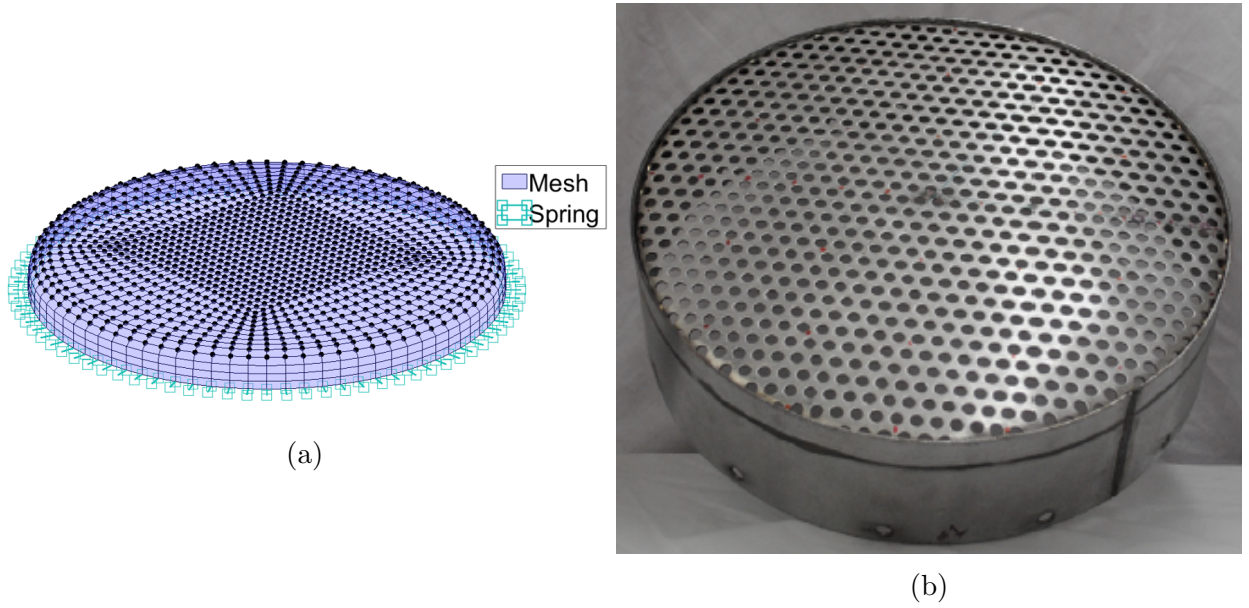


Figure 89: Finite element model representation of the exhaust plate in which the plate is modeled with 4-node shell elements, the boundary is represented with radial springs and the circles represent nodes that are used for interpolation and control of plate radius

The mesh of the FE model and the points where DIC measurements were recorded are overlaid is presented in Figure 90. A 2D gridded interpolation is used to select the transverse displacement of the FE nodes to correlate with the experimental data.

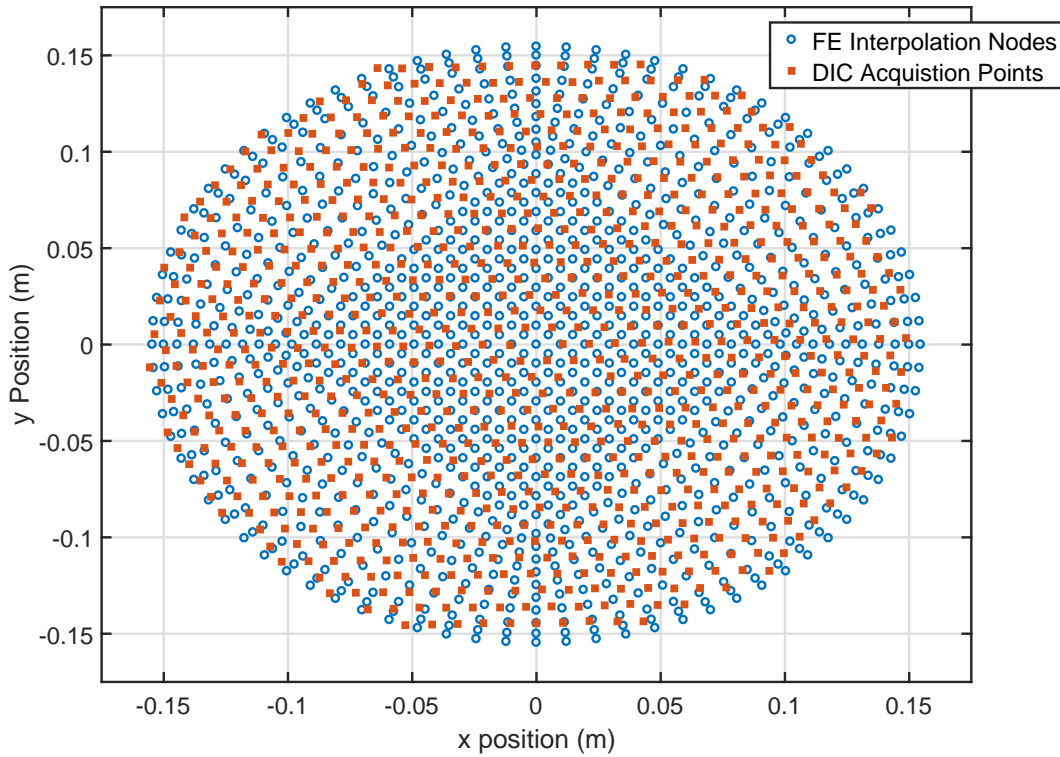


Figure 90: Locations of the nodes in the FE model considered within the interpolation routine and the DIC acquisition points.

5.4.2 Linear Finite Element Model Updating

Prior to nonlinear updating, linear model updating was performed to have a good starting model for the nonlinear model updating procedure. The target data was the first 10 linear normal modes extracted from a low-level test with burst random excitation from [102]. The free parameters for the linear model updating were the modulus of elasticity, radius of curvature of the top plate, and the radial spring stiffness values. The experimentally identified modes along with the FE model's interpolated mode shapes are presented in Figure 91 for modes 1-5. Modes 6-10 can be found in Figure 92.

The initial parameter values, final values and percent changes are presented in Table

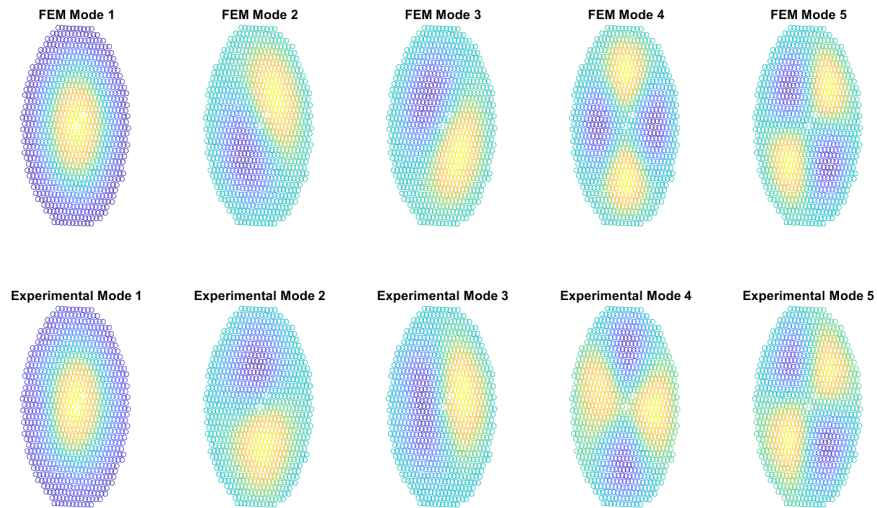


Figure 91: First 5 linear normal modes of the exhaust plate.

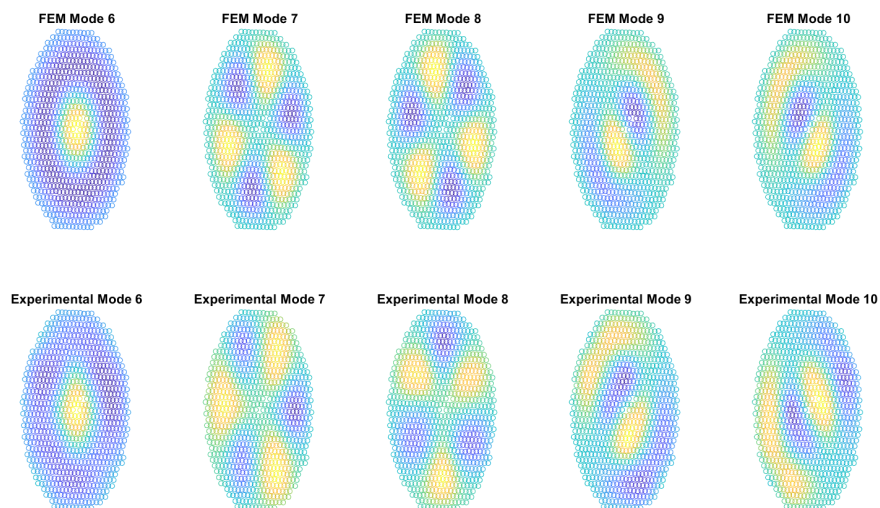


Figure 92: Linear normal modes 6 to 10 of the exhaust plate.

21. Although the parent material is steel with an elastic modulus of 200 GPa the holes present within the structure, which are not modeled, result in a reduction of stiffness of the structure. The initial elastic modulus used in this work was taken from [102] which used an approximation based on the parent material, hole pattern and hole size to determine the

effective modulus of the plate if it were modeled without the holes. The resulting modulus value was 168 GPa. The final value obtained, after linear updating in this work, agrees well with the final value obtained in [102], which was 96 GPa. The radial spring values did not change during the updating, and the bending modes were found to be fairly insensitive to the change in the radial stiffness values. The initial radius of curvature, 200 m, was set to a value that provided a nearly flat surface. The final radius of curvature provided a maximum height of 3 mm above the outer edge portion, which compares well with the DIC data from [102]. This is shown in Figure 93 where subplot (a) contains a side view of the FE model and subplot(b) a side view of the DIC data used to estimate the curvature of the plate [102]. In this study, the structure is still symmetric, whereas in reality this is not the case so some error in the repeated modes of the structure is expected.

The linear model updating results for the first 10 modes are presented in Table 22. The initial model, with a flat top surface, has frequency errors up to 25% for many of the modes. After the linear model updating procedure the largest error is 3% for modes 2 and 3, which are repeated modes, and as stated earlier, some error is expected with those modes because the asymmetry present in the structure was not modeled. These errors would be considered acceptable for typical linear model updating studies, for example, NASA and the Air Force want frequency errors of no more than 3–5% typically. The modal assurance criteria (MAC) values are also presented in the table, which denote the similarity of the shapes between the numerical model and the experimental data. The first bending mode of the system, the NNM of interest, has MAC value of 0.986, indicating a well correlated mode. The lowest MAC value was 0.878 for the 10th mode, which is a repeated mode and as such some error is expected.

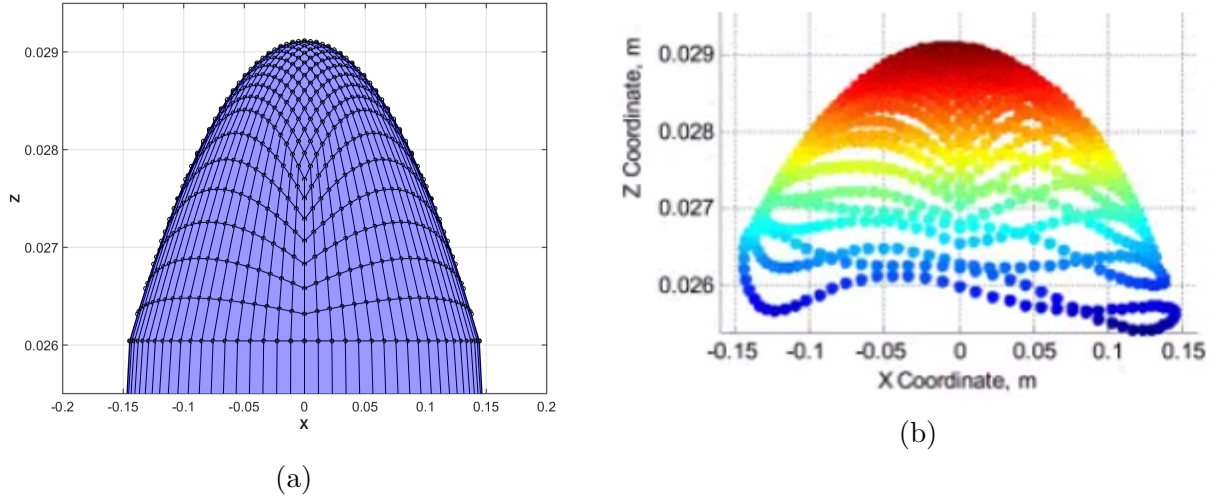


Figure 93: Side views of the exhaust plate (a) Finite element model (b) DIC data from [102].

Table 21: Exhaust plate parameters before and after linear model updating.

Parameter	Initial Value	Final Value	% Change
Elastic Modulus (GPa)	168.00	95.50	43.15
Radius of Curvature (m)	200.000	0.919	99.54
Radial Spring Stiffness (N/m)	1×10^6	1×10^6	0.00

Table 22: Natural frequencies before $()_0$ and after $()_F$ model updating of the exhaust plate.

Mode #	f_{exp}	$f_{num,0}$	$error_0(\%)$	$f_{num,F}$	$error_F(\%)$	MAC_F
1	205.36	174.63	-14.96	207.71	1.15	0.986
2	327.78	362.61	10.60	337.69	3.01	0.980
3	348.65	362.69	4.03	337.77	-3.12	0.969
4	489.16	598.73	22.40	502.60	2.75	0.925
5	510.22	599.78	17.55	503.34	-1.35	0.958
6	572.62	683.02	19.28	557.04	-2.72	0.939
7	697.89	882.42	26.44	707.31	1.35	0.905
8	699.95	882.45	26.07	707.37	1.05	0.909
9	814.11	1044.05	28.24	822.69	1.05	0.903
10	827.68	1044.28	26.17	822.87	-0.58	0.878

5.4.3 Nonlinear Reduced Order Model Updating

After the linear model was well correlated to the low level data, a series of nonlinear reduced order models were created using the implicit condensation procedure. The first ROM created

was a single mode model consisting of the first mode with two nonlinear terms, a quadratic and cubic. The 1st NNM of the ROM is plotted in Figure 94 along with the experimentally extracted NNM data from [102]. Note that the 1-DOF model does not predict the softening then hardening behavior of the experimental NNM data at all, even after the model updating procedure and regardless of the number of harmonics included within the solution. The reason for this is that the experimental data after the softening to hardening transition is actually along an internal resonance branch. The internal resonance is with the 6th mode of the system, so the 6th mode is required within the ROM's basis set to be able to trace the internal resonance branch and as such was included within the basis set next.

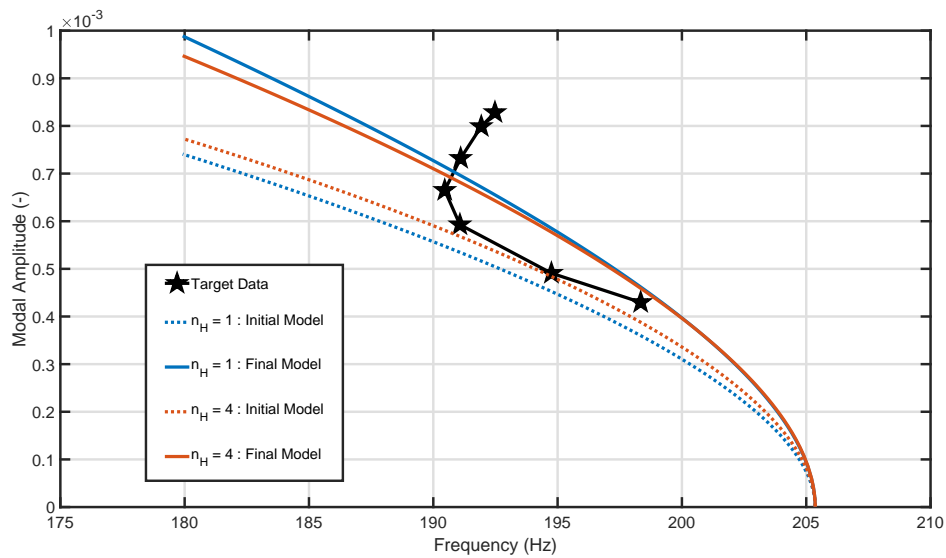


Figure 94: Nonlinear normal modes of the exhaust plate, represented as first modal amplitude versus frequency, including the experimentally identified data, the original models, and final modes of a 1-DOF ROM with various number of harmonics included in the solution.

The model updating was then repeated for a 2-mode ROM including the first and sixth mode of the exhaust plate. The 1st nonlinear normal mode of the 2-DOF ROM along with the experimental NNM points are plotted in Figure 95. The numerical data shown in the

figure are the interpolated points along the NNM curve, the seven NNM solutions with the closest euclidean distance to the experimental NNM points. Since the available experimental data is along an internal resonance branch, the single harmonic solution plotted in Figure 95 misses the internal resonance and does a poor job of estimating the data. For a complete picture of the NNM curve of the single harmonic response, refer to Figure 97, which shows the NNM of the ROM at all points along the NNM and over a larger range of amplitude. It is more clear that the branch in question is an internal resonance branch. The model updating procedure was applied to the nonlinear coefficients of the ROM, and the results show the ROM has no chance of predicting the internal resonance. After model updating the behavior of the NNM is noticeably different between the two models, with the updated model containing a softening to hardening transition along the main backbone.

A solution with three harmonics captures the internal resonance turning point well with a frequency error of only 1 Hz as demonstrated in Figure 95. Similarly, when including the fourth harmonic the original model is able to capture the curve fairly well, surprisingly with only slightly lower frequency error at the turning point, but both solutions under predict the amplitude after the turning point for a specific frequency. After model updating, both solutions better represent the curve past the turning point. Once again, to better demonstrate the NNM curve the four harmonic solution, before and after updating, is plotted in Figure 97 which includes all solutions, not just the one used for interpolation within the model updating algorithm. Subplot (b) contains a zoomed in portion of the plot that highlights the updated four harmonic solution's ability to better represent the data compared to the original model.

The parameters of the 2-DOF ROM with four harmonics included within the MHB

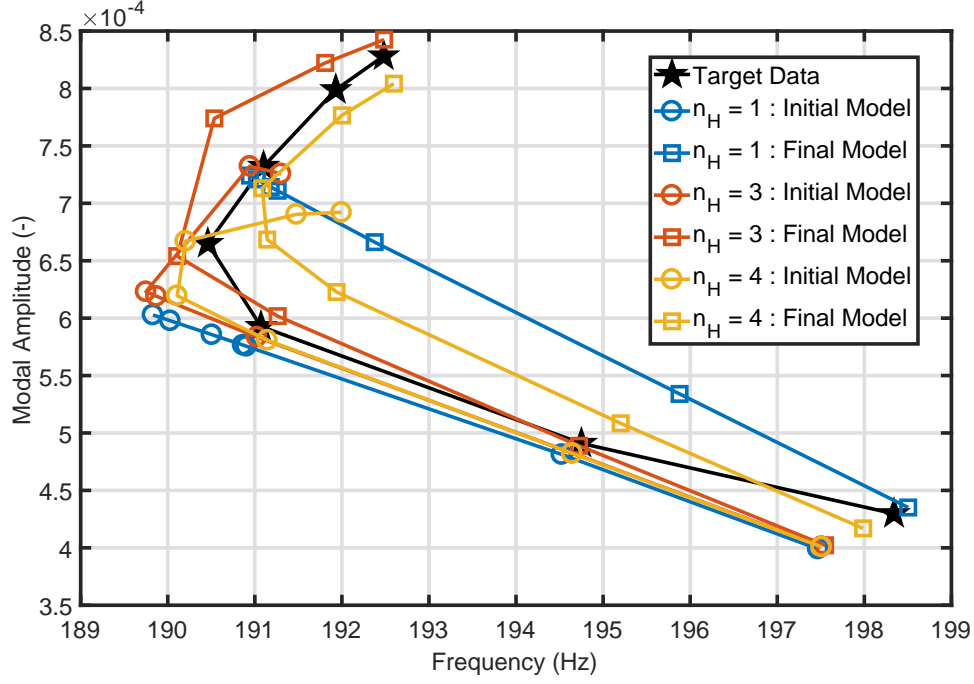


Figure 95: Nonlinear normal modes of the exhaust plate, represented as first modal amplitude versus frequency, including the experimentally identified data, the original models and final modes of a 2-DOF ROM with 1, 2, and 4 harmonics included within the MHB solution.

solution are presented in Figure 96. The change in all the parameters is very small with a maximum change of less than 7% for the first mode quadratic value, α_{11} . Even though the changes are small the influence on the NNM is significant as previously noted. Additionally there is noticeable change in the quadratic coupling parameter between the first and sixth mode, α_{16} . The alteration of this value indicates a change in the amount of coupling between the first and sixth mode of the system which occurs during the internal resonance.

The nonlinear cost function values for the 2-DOF ROM model with various harmonics included within the MHB solution are presented in Table 23. In the single harmonic case, even though the curve is not represented well, the cost function decreased by a factor of 3. The cost function is reduced by a factor of 4 for the three and four harmonic solutions.

A frequency energy plot is presented in Figure 98. The frequency energy plot is used as

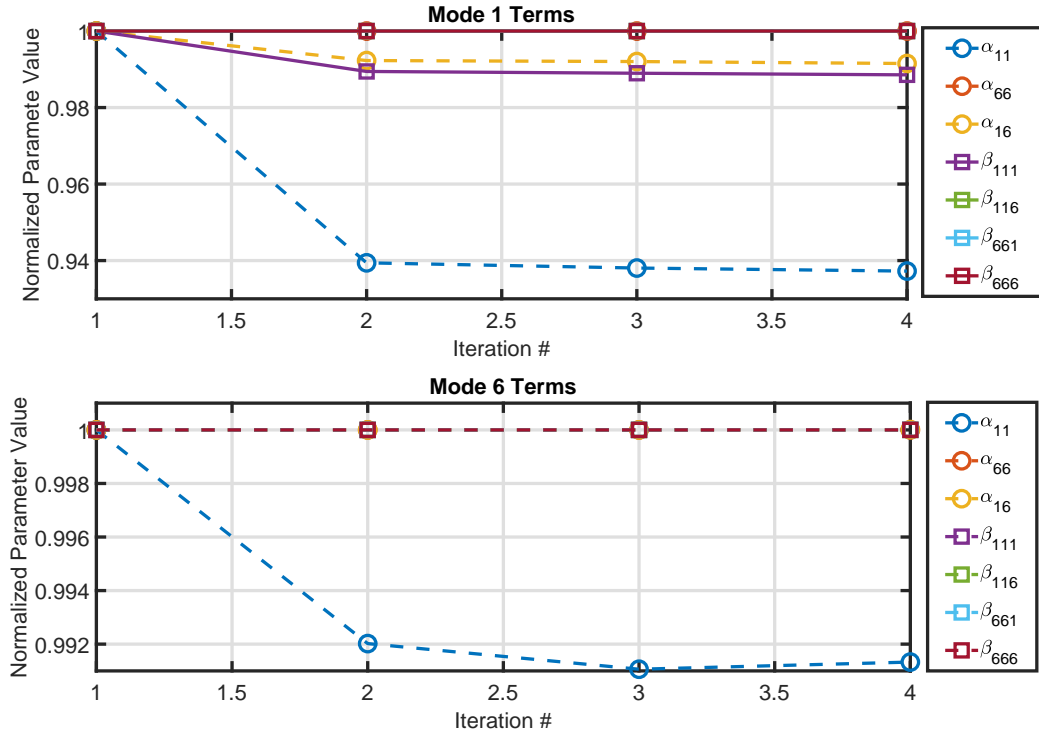


Figure 96: Normalized nonlinear stiffness parameters during the model updating procedure of the 2-DOF ROM with four harmonics included within the MHB solution

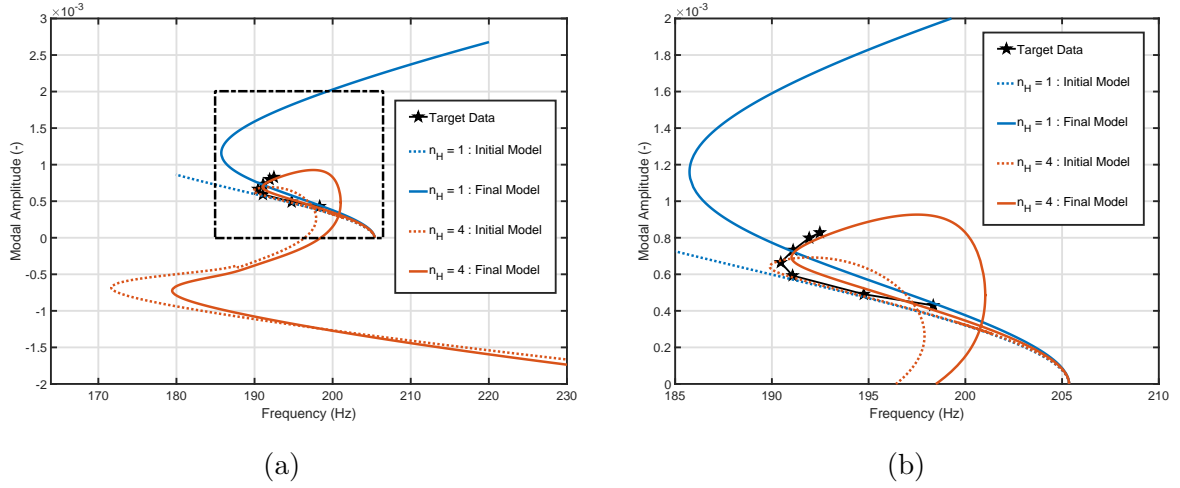


Figure 97: Full nonlinear normal mode curve of the 2-DOF ROMs represented as first modal amplitude versus frequency. (a) The entire computed curve. (b) A zoomed in portion of the curve, defined by the box in subplot (a), to highlight the experimental data.

a simple way to demonstrate the difference between the single harmonic and four harmonics solution, in particular highlighting the internal resonance portion of the branch. To demonstrate that the loop is truly an internal resonance the time history response along the orbit at a few solutions along the NNM curve are presented in Figure 99. At point A along the main backbone branch the response is primarily in the first mode whereas at point B, along the internal resonance loop, the response is in both the first and sixth mode. The sixth mode is oscillating at 3 times the frequency of the first mode indicating a 1:3 internal resonance of the sixth mode. At points C and D further along the NNM the response is once again primarily in the first mode but with still a minor contribution from the 6th mode with that higher harmonic response.

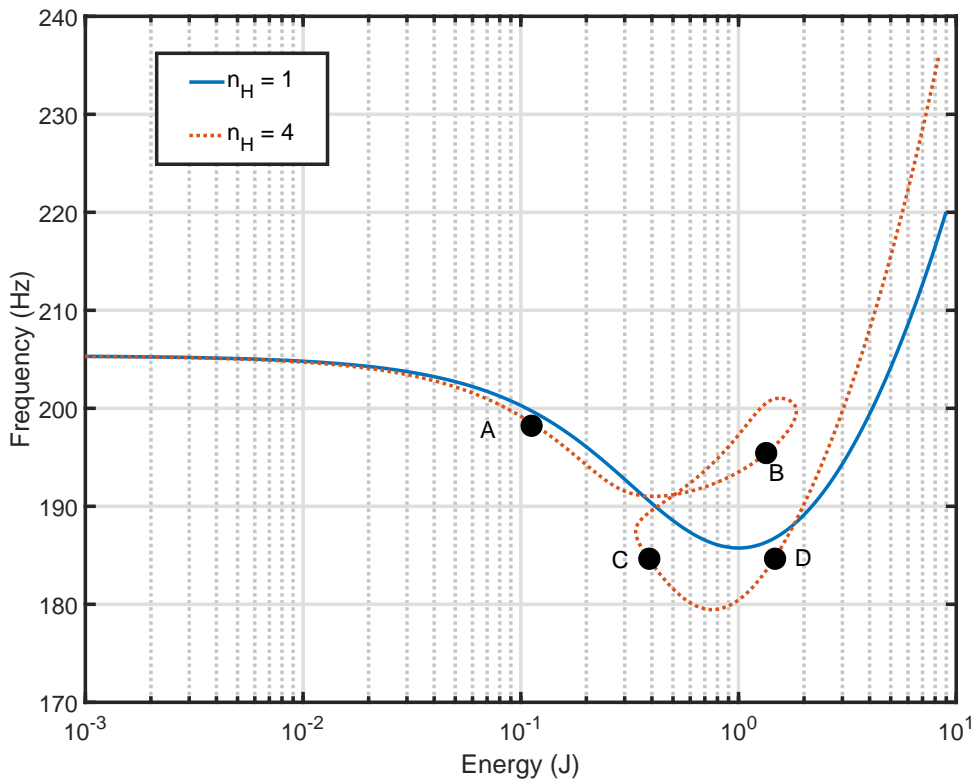


Figure 98: Nonlinear normal modes of the 2-DOF ROM after updating represented as frequency versus energy of the system.

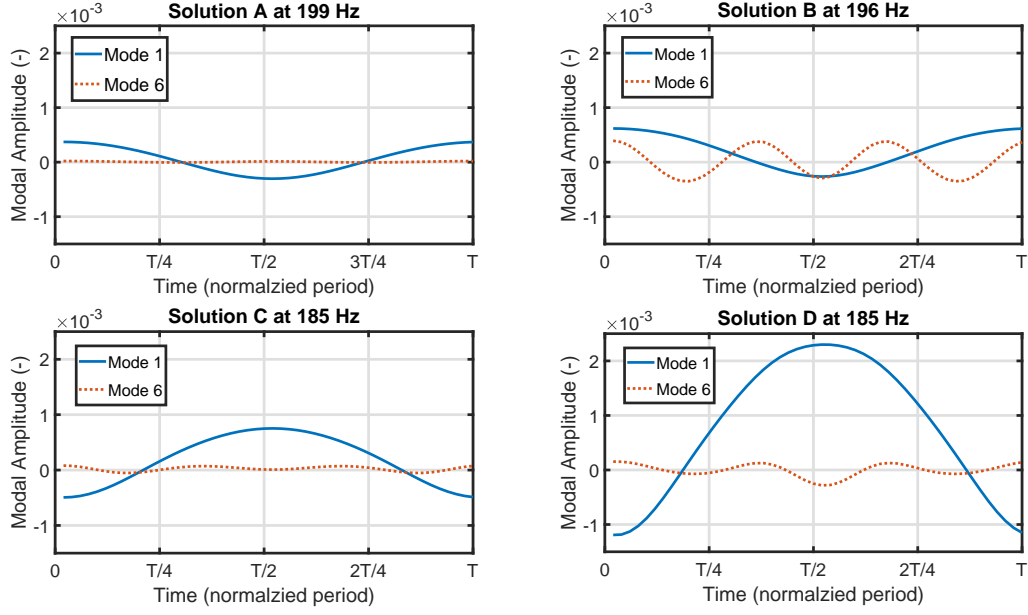


Figure 99: Modal amplitude response along the period of selected solutions from Figure 98 of the 2-DOF ROM's NNM with 4 harmonics included in the solution.

Table 23: Nonlinear cost function before and after updating the 2-DOF ROM model with different number of harmonics included within the MHB solution.

# of Harmonics	Π_0	Π_F
1	0.2151	0.0653
3	0.1176	0.0281
4	0.1004	0.0231

5.4.4 Discussion

This section described the process of updating a finite element model to match the linear frequencies of an experimental system followed by updating the nonlinear coefficients of a ROM created from the correlated FE model. In this case there was considerably more linear modes used within the linear model correlation procedure which once finished the models the ROM provided fairly accurate nonlinear normal modes compared to the experimental data. In the case of a ROM it was found that a 2-DOF ROM with four harmonics was able

to accurately capture the internal resonance portion of branch. Even though the original model was fairly accurate, the model updating procedure was able to still improve the model which had a large influence on the primary backbone of the NNM by shifting the softening to hardening transition point by 9 Hz. Model updating was not performed on the FE model because it was already fairly accurate with respect to the experimental data, for details see Appendix B.

5.5 Recap

This section covered updating both reduced order models and finite element models to match experimentally extracted NNMs of geometrically nonlinear structures. The structures included a nominally flat beam with a pure hardening NNM, a curved beam with a softening then hardening NNM and an exhaust cover plate with an internal resonance along the NNM. All of these case studies demonstrated the ability of the model updating procedure to capture the unique dynamics of each experimental structure.

6 Conclusion

This work has presented a model updating strategy for nonlinear systems represented by either a finite element model or a reduced order model, using nonlinear normal modes as a correlation metric. The model updating procedure utilized a gradient based optimization routine to drive the model's NNM towards the objective NNM. The method was enhanced because the computation of the NNM using the MHB method made it possible to compute analytical gradients of the NNMs with respect to the design parameters. Due to the

complex nature of the NNM curves, a nearest neighbor search was implemented to identify which points to compare between experimental and numerical model NNMs rather than an interpolation procedure.

The method was first demonstrated on numerical examples including a flat beam with fixed boundary conditions, the same beam with variable boundary conditions. and a flat plate with compliant boundaries. It was demonstrated that in all these cases the ROM could be updated to match the target NNM curves. In the second case the ROM coefficients were found to be in good agreement with coefficients estimated from the correct FE models demonstrating that it is possible to tune the polynomial parameters of a ROM to capture unknown physical parameters of a structure.

The method was then applied to three experimental systems; two were beams mounted on a somewhat flexible backing structure and the last was a curved, perforated plate. The first of the two beams was flat and both the FE models and ROMs were able to be tuned with ease to match the response of the structure. In this case the final ROM parameters from the model updating procedure matched well with the ROM parameters identified from the updated FE model. The second beam, which contained some curvature, exhibited a softening then hardening behavior in the NNM, providing a challenging case with complex dynamics. Nevertheless, the model updating procedure was still able to produce ROMs and FE models that were able to accurately capture the experimental NNM of the structure. The exhaust plate case study demonstrated the ability of the procedure to update ROMs to capture internal resonance branch, which was present in the experimental data. This demonstrated the ability of the procedure to work on systems with strong modal coupling present.

Tuning the parameters of a ROM from an accurate linear FE model to match the experimental NNMs provided an efficient way to obtain an accurate model to predict the nonlinear response of the system. An approach such as this could be very attractive in industry, such as when modeling aircraft panels. There it would likely be far easier to model only the panel of interest, perform linear model updating and not have to mesh the support structure and other components, which may require more effort and add detail to the FE model. The tuning of the polynomial coefficients of the ROM provide a flexible approach to capturing the nonlinear response of the structure but comes with the drawback that the coefficients are difficult to interpret physically.

Updating parameters of the FE model on the other hand, is computationally more expensive but the analyst has a stronger intuition into the validity of the parameters identified during the updating procedure. This is an appealing approach in practice because one typically wants to have confidence in the values of the actual parameters are for future design and analysis of the structure. It is anticipated that the combination of these two approaches for updating nonlinear structural systems can greatly aid the model correlation and updating practices in the aerospace industry for systems undergoing geometrically nonlinear response.

7 Future Work

The work completed to date has consisted of implementing the multi harmonic balance method for nonlinear ROMs and nonlinear FE models. The main contribution of the work has been on the development of a model updating scheme for nonlinear system using nonlinear normal modes as a correlation metric computed using the MHB method. The updating

procedure has been demonstrated on numerical systems as well as applied efficiently to experimental systems. The following are potential areas of future improvement on the procedure and updating process as whole for advanced aircrafts.

7.1 Thermal Effects

Thermal effects are present in the aerospace vehicles of interest which creates thermal stresses in the structural components that can cause alteration of linear natural frequencies and even nonlinear buckling. It would be desirable to apply the model updating procedure to a system that contains thermal effects. The nominal model would be correlated in the unheated state, then the process would be conducted at subsequent temperatures of interest. A diagram of how the thermal effects will be included within the model updating procedure is presented in Figure 100.

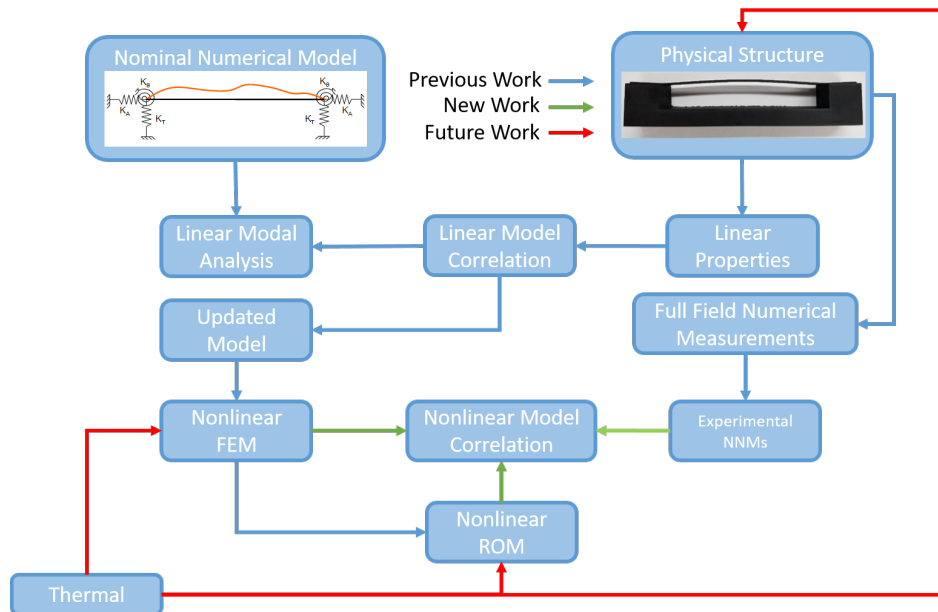


Figure 100: Overview of model updating procedure with previous work, progress this preliminary work has contributed to the field and potential future work that includes thermal effects.

7.2 Updating FE Models to Match Nonlinear Reduced Order Models

A drawback of updating a ROM directly is lack of insight into which physical parameters, i.e. parameters that one would control in a FE model, are incorrect with respect to the experimental system. Potential future work would establish a procedure to tune the parameters of a FE model to match a target set of ROM parameters. The target ROM parameters consist of the linear stiffness and the nonlinear stiffness coefficients which have been identified previously through test-analysis correlation and updating. In this process an optimization routine is setup in which the free parameters are those of the FE model, such as boundary stiffness springs, imperfections, pre-stress, etc. The optimization produce is wrapped around a ROM creation algorithm that iteratively tunes the FE parameters, creates a ROM, and evaluates the ROM parameters with respect to the target ROM in order minimize the objective function. An overview of the procedure can be found in Figure 101.

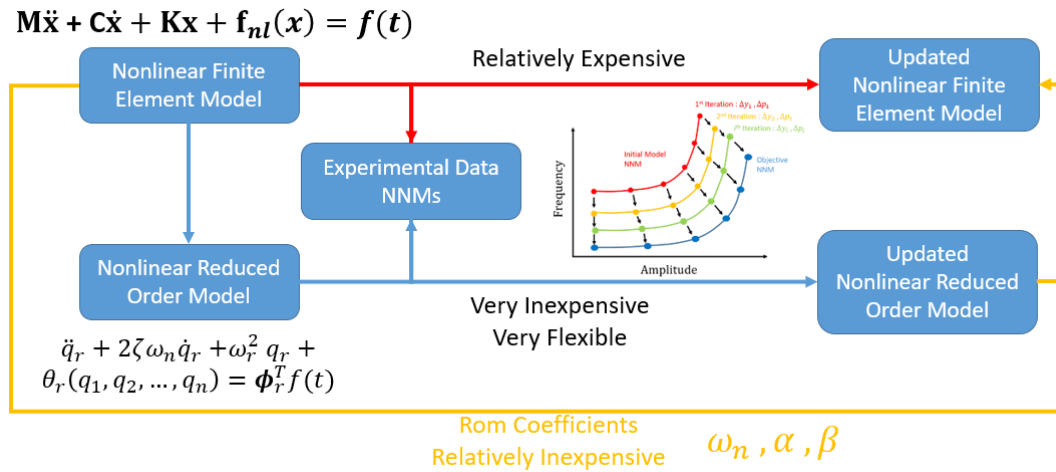


Figure 101: Flow diagram of the model updating procedure in which a ROM is updated to test data directly (blue line) and then the FE model is updated to match the parameters of the updated ROM (yellow line).

Acknowledgments

This work was supported by the Air Force Office of Scientific Research, Award # FA9550-17-1-0009, under the Multi-Scale Structural Mechanics and Prognosis program managed by Dr. Jaimie Tiley.

Appendices

A Publications of PhD Work

A.1 Journal

- C. I. Van Damme, M. S. Allen, J. J. Hollkamp, "Evaluating Reduced Order Models of Curved Structures using Static Equilibrium Paths for Random Response Prediction" *Journal of Sound and Vibration* (Under Revision)
- C. I. Van Damme, M. S. Allen, J. J. Hollkamp, "Model Updating of Geometrically Non-linear Reduced Order Models using Nonlinear Normal Modes and the Multi-Harmonic Balance Method" *AIAA Journal* (Submitted)
- C. I. Van Damme, M. S. Allen, J. J. Hollkamp, "Model Updating of Geometrically Non-linear Finite Element Models using Nonlinear Normal Modes and the Multi-Harmonic Balance Method" *Journal of Sound and Vibration* (In preparation)
- C. I. Van Damme, M. S. Allen, J. J. Hollkamp, "Application of Simultaneous Regression and Selection in Nonlinear Modal Model Identification" *Mechanical Systems and Signal Processing* (In preparation)

A.2 Conference

- C. I. VanDamme and M. S. Allen, "Using Nonlinear Normal Modes to Optimize the Design of Geometrically Nonlinear Structures," in *AIAA/ASCE/AHS/ASC Structures, Structural Dynamics, and Materials Conference*, 2019
- C. I. VanDamme, M. S. Allen, and A. M. Madrid, "Using the harmonic balance method to directly compute nnms of geometrically nonlinear finite element models'," in *ISMA*, (Leuven, Belgium), 2018
- C. I. VanDamme, M. S. Allen, and J. J. Hollkamp, "Nonlinear Structural Model Updating Based Upon Nonlinear Normal Modes," in *AIAA/ASCE/AHS/ASC Structures, Structural Dynamics, and Materials Conference*, 2018
- C. I. VanDamme, B. Moldenhauer, M. S. Allen, and J. J. Hollkamp, "Computing Nonlinear Normal Modes of Aerospace Structures Using the Multi-harmonic Balance Method," in *Nonlinear Dynamics, Volume 1*, pp. 247–259, Springer, 2018
- J. D. Schoneman, C. Ostoich, L. Jarman, C. I. VanDamme, and M. S. Allen, "Impact of Flow and Structural Nonlinearities on Hypersonic Panel Flutter Predictions," in *AIAA/ASCE/AHS/ASC Structures, Structural Dynamics, and Materials Conference*, American Institute of Aeronautics and Astronautics, 2018
- C. I. VanDamme and M. S. Allen, "Evaluating NLROMs' Ability to Predict Dynamic Snap Through of a Curved Beam in a Random Loading Environment," in *58th*

AIAA/ASCE/AHS/ASC Structures, Structural Dynamics, and Materials Conference, American Institute of Aeronautics and Astronautics, 2017

- C. I. VanDamme and M. S. Allen, “Nonlinear Normal Modes of a Curved Beam and Its Response to Random Loading,” in *Nonlinear Dynamics, Volume 1*, pp. 115–126, Springer, 2017
- L. M. Jarman, C. VanDamme, and M. S. Allen, “Nonlinear Dynamic Analysis of a Thermally Buckled Aircraft Panel Using NNMs,” in *Shock & Vibration, Aircraft/Aerospace, Energy Harvesting, Acoustics & Optics, Volume 9*, pp. 59–69, Springer, 2017
- C. I. VanDamme and M. S. Allen, “Using nnms to evaluate reduced order models of curved beam,” in *Rotating Machinery, Hybrid Test Methods, Vibro-Acoustics & Laser Vibrometry, Volume 8*, pp. 457–469, Springer, 2016

B Exhaust Plate : Nonlinear Finite Element Model

Updating

This appendix section contains NNMs of the exhaust plate from 5.4 computed directly from the FE model. After the linear model was well correlated to the low level data, nonlinear model updating was intended to be conducted. In this case the only free parameter was going to be the linear stiffness values of radial boundary springs. The value of the radial springs determine the amount of axial stretching of the main plate. A beneficial aspect of having a linear design variable is that it greatly speeds up the modeling updating procedure using the formulation in this paper since it only requires evaluation of the linear stiffness gradient. Prior to nonlinear updating the NNMs with various harmonics were computed of the model after the linear model updating procedure, those NNMs along with the experimental data are presented in Figure 102. A single harmonic solution, not shown here, continues to soften and misses the internal resonance as was shown in the previous section with the ROMs. The solution with three harmonics included does a fair job at estimating the experimental data

with an over prediction of the turning point frequency of only 1.5 Hz. When including up to four harmonics the turning point of the internal resonance converges at a value of 1.5 Hz below the experimental data, evaluated by comparing with a solution with 5 harmonics. Although after the turning point the solutions, between the four and 5 harmonic cases, do deviate the curves are nearly the same up to the extent of the available experimental data and as such the four harmonic solution will be used in the updating routine.

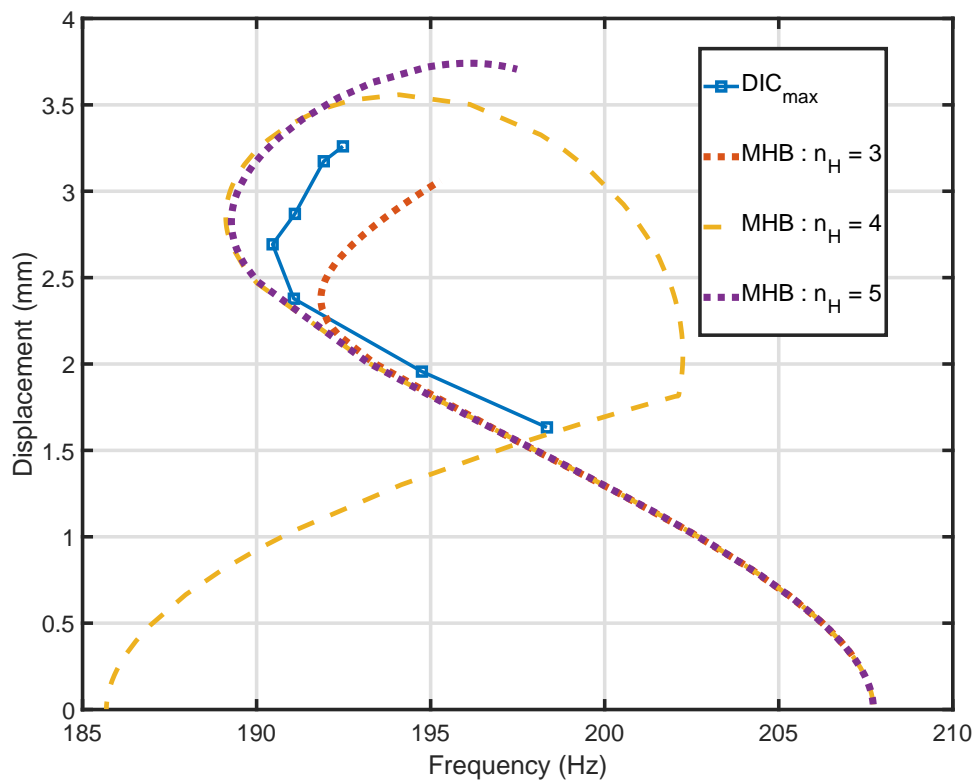


Figure 102: Comparing the NNMs of the FE model with various harmonics and the experimentally identified data.

The gradient of the NNM, represented as center of plate displacement versus frequency, with respect to the radial spring value is shown in Figure 103 when including 3 harmonics within the solution. A unit increase in the radial stiffness value shifts the curve up in fre-

quency with little influence on the displacement. The NNM solution in general is insensitive to the change in the radial stiffness value, a factor of 2 increase or decrease in the stiffness value only shifts the softening to hardening transition by a 0.10 Hz. With this information in mind, it was not pursued to further update the nonlinear finite element model since the NNM is captured fairly accurately with a maximum error of 1.5 Hz. Decreasing the error there could be accounted for by allowing the linear frequency to shift up 1.5 Hz which would still remain below 2% error of the experimental linear frequency.

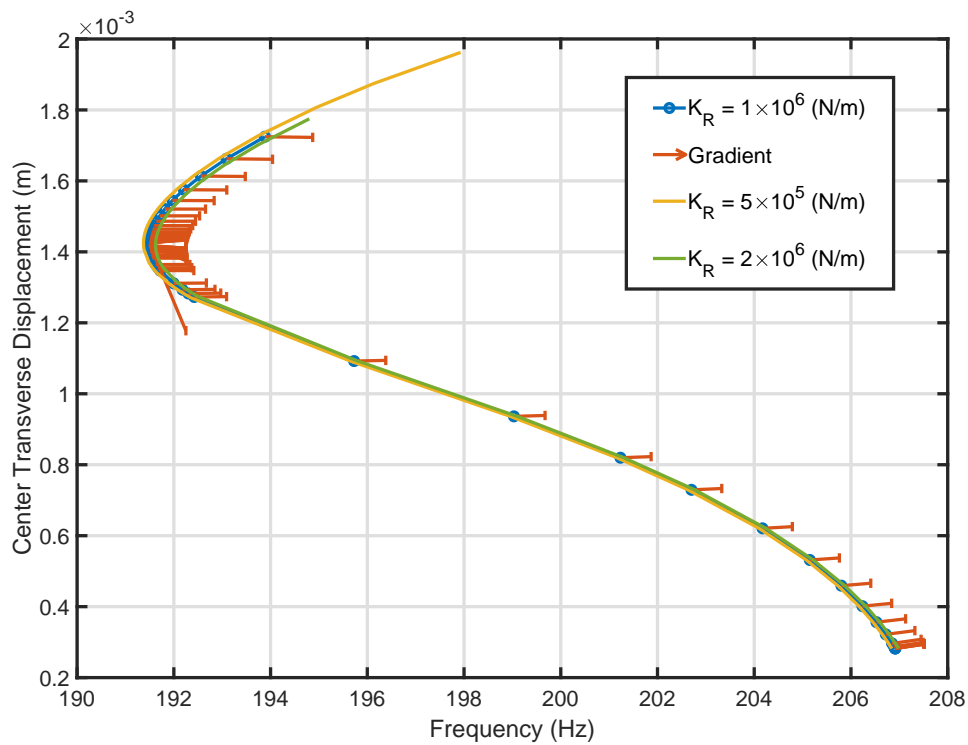


Figure 103: Gradient of the NNM curve, represented as center of plate transverse displacement versus frequency, with respect to the radial spring values.

References

- [1] E. J. Tuegel, A. R. Ingraffea, T. G. Eason, and S. M. Spottswood, “Reengineering Aircraft Structural Life Prediction Using a Digital Twin,” *International Journal of Aerospace Engineering*, vol. 2011, p. 14, 2011.

- [2] E. Glaessgen and D. Stargel, "The Digital Twin Paradigm for Future NASA and U.S. Air Force Vehicles," in *53rd AIAA/ASME/ASCE/AHS/ASC Structures, Structural Dynamics and Materials Conference*, Structures, Structural Dynamics, and Materials and Co-located Conferences, (Honolulu, Hawaii), American Institute of Aeronautics and Astronautics, Apr. 2012.
- [3] B. Zuchowski, R. Jacobs, and S. Liguore, "AIR VEHICLE INTEGRATION AND TECHNOLOGY RESEARCH (AVIATR) Task Order 0015: Predictive Capability for Hypersonic Structural Response and Life Prediction: Phase 1-Identification of Knowledge Gaps, Volume 1–Nonproprietary Version," Tech. Rep. AFRL-RB-WP-TR-2010-3068, 2010.
- [4] R. Quiroz, J. Embler, R. Jacobs, G. Tzong, and S. Liguore, "Air vehicle integration and technology research (aviatr). task order 0023: Predictive capability for hypersonic structural response and life prediction: Phase 2-detailed design of hypersonic cruise vehicle hot-structure," Tech. Rep. AFRL-RB-WP-TR-2010-0265, BOEING CO HUNTINGTON BEACH CA, 2012.
- [5] R. D. Blevins, I. Holehouse, and K. R. Wentz, "Thermoacoustic loads and fatigue of hypersonic vehicle skin panels," *Journal of Aircraft*, vol. 30, no. 6, pp. 971–978, 1993.
- [6] A. J. Culler and J. J. McNamara, "Impact of fluid-thermal-structural coupling on response prediction of hypersonic skin panels," *AIAA Journal*, vol. 49, no. 11, pp. 2393–2406, 2011.
- [7] K. D. Murphy, L. N. Virgin, and S. A. Rizzi, "Experimental snap-through boundaries for acoustically excited, thermally buckled plates," *Experimental Mechanics*, vol. 36, no. 4, pp. 312–317, 1996.
- [8] A. Przekop and S. A. Rizzi, "Dynamic Snap-Through of Thin-Walled Structures by a Reduced-Order Method," *AIAA Journal*, vol. 45, no. 10, pp. 2510–2519, 2007.
- [9] E. H. Dowell, "Nonlinear flutter of curved plates.," *AIAA Journal*, vol. 7, pp. 424–431, Mar. 1969.
- [10] J. J. Hollkamp, R. W. Gordon, and S. M. Spottswood, "Nonlinear sonic fatigue response prediction from finite element modal models: a comparison with experiments," in *44th AIAA/ASME/ASCE/AHS/ASC Structures, Structural Dynamics, and Materials Conference*, p. 1709, 2003.
- [11] S. M. Spottswood and R. J. Allemang, "On the Investigation of Some Parameter Identification and Experimental Modal Filtering Issues for Nonlinear Reduced Order Models," *Experimental Mechanics*, vol. 47, pp. 511–521, Aug. 2007.
- [12] R. W. Gordon and J. J. Hollkamp, "Reduced-order Models for Acoustic Response Prediction," technical, Tech Report: AFRL-RB-WP-TR-2011-3040., Air Force Research Laboratory, 2011.

- [13] M. Mignolet, A. Przekop, S. Rizzi, and M. Spottswood, "A review of indirect/non-intrusive reduced order modeling of nonlinear geometric structures," *Journal of Sound and Vibration*, vol. 332, no. 10, pp. 2437–2460, 2013.
- [14] M. Nash, *Nonlinear Structural Dynamics by Finite Element Modal Synthesis*. PhD Thesis, Imperial College, The University of London, 1977.
- [15] Y. Shi and C. Mei, "A Finite Element Time Domain Modal Formulation for Large Amplitude Free Vibrations of Beams and Plates," *Journal of Sound and Vibration*, vol. 193, pp. 453–464, June 1996.
- [16] C. Mei, "Response of Nonlinear Structural Panels Subjected to High Intensity Noise," tech. rep., AFWAL-TR-80-3018, 1980.
- [17] Y. Shi, R. Y. Y. Lee, and C. Mei, "Finite Element Method for Nonlinear Free Vibrations of Composite Plates," *AIAA Journal*, vol. 35, pp. 159–166, Jan. 1997.
- [18] P. Tiso, E. Jansen, and M. Abdalla, "Reduction Method for Finite Element Nonlinear Dynamic Analysis of Shells," *AIAA Journal*, vol. 49, pp. 2295–2304, Oct. 2011.
- [19] J. J. Hollkamp and P. J. O'Hara, "Using Complex Variables to Estimate the Derivatives of Nonlinear Reduced-Order Models," in *57th AIAA/ASCE/AHS/ASC Structures, Structural Dynamics, and Materials Conference*, AIAA SciTech Forum, American Institute of Aeronautics and Astronautics, Jan. 2016.
- [20] S. W. Doebling, C. R. Farrar, and M. B. Prime, "A summary review of vibration-based damage identification methods," *Shock and vibration digest*, vol. 30, no. 2, pp. 91–105, 1998.
- [21] N. Stubbs and J.-T. Kim, "Damage localization in structures without baseline modal parameters," *AIAA journal*, vol. 34, no. 8, pp. 1644–1649, 1996.
- [22] T. Abrahamsson, *Calibration and Validation of Structural Dynamics Models*. Gothenburg, Sweden: Course literature in Structural Dynamics-Model Validation, Chalmers University of Technology, Gothenburg, Sweden, 2012.
- [23] J. Mottershead and M. Friswell, "Model Updating In Structural Dynamics: A Survey," *Journal of Sound and Vibration*, vol. 167, pp. 347–375, Oct. 1993.
- [24] M. Friswell and J. E. Mottershead, *Finite element model updating in structural dynamics*, vol. 38. Springer Science & Business Media, 2013.
- [25] R. M. Rosenberg, "Normal modes of nonlinear dual-mode systems," *Journal of Applied Mechanics*, vol. 27, no. 2, pp. 263–268, 1960.
- [26] G. Kerschen, M. Peeters, A. f. Vakakis, and J. C. Golinval, "Nonlinear normal modes, Part I: A useful framework for the structural dynamicist," *Mechanical Systems and Signal Processing*, vol. 23, no. 1, pp. 170–194, 2009.

- [27] C. I. VanDamme, M. S. Allen, and J. J. Hollkamp, "Nonlinear Structural Model Updating Based Upon Nonlinear Normal Modes," in *AIAA/ASCE/AHS/ASC Structures, Structural Dynamics, and Materials Conference*, 2018.
- [28] C. I. VanDamme, M. S. Allen, and A. M. Madrid, "Using the harmonic balance method to directly compute nnms of geometrically nonlinear finite element models'," in *ISMA*, (Leuven, Belgium), 2018.
- [29] M. Peeters, G. Kerschen, and J. Golinval, "Dynamic testing of nonlinear vibrating structures using nonlinear normal modes," *Journal of Sound and Vibration*, vol. 330, pp. 486–509, Jan. 2011.
- [30] J.-P. Noël, L. Renson, C. Grappasonni, and G. Kerschen, "Identification of nonlinear normal modes of engineering structures under broadband forcing," *Mechanical Systems and Signal Processing*, vol. 74, pp. 95–110, June 2016.
- [31] D. A. Ehrhardt and M. S. Allen, "Measurement of nonlinear normal modes using multi-harmonic stepped force appropriation and free decay," *Mechanical Systems and Signal Processing*, vol. 76-77, pp. 612–633, 2016.
- [32] M. A. Crisfield, *Non-linear Finite Element Analysis of Solids and Structures*. John Wiley & Sons, 1991.
- [33] M. A. Crisfield, *Non-linear finite element analysis of solids and structures: Volume 2. Advanced topics*, vol. 2. John Wiley & Sons, Inc., 1997.
- [34] E. Riks, "An incremental approach to the solution of snapping and buckling problems," *International Journal of Solids and Structures*, vol. 15, no. 7, pp. 529–551, 1979.
- [35] M. Eriten, M. Kurt, G. Luo, D. M. McFarland, L. A. Bergman, and A. F. Vakakis, "Nonlinear system identification of frictional effects in a beam with a bolted joint connection," *Mechanical Systems and Signal Processing*, vol. 39, no. 1-2, pp. 245–264, 2013.
- [36] L. Gaul and J. Lenz, "Nonlinear dynamics of structures assembled by bolted joints," *Acta Mechanica*, vol. 125, no. 1-4, pp. 169–181, 1997.
- [37] M. R. Brake, "The effect of the contact model on the impact-vibration response of continuous and discrete systems," *Journal of Sound and Vibration*, vol. 332, pp. 3849–3878, July 2013.
- [38] M. Brake, "A hybrid approach for the modal analysis of continuous systems with discrete piecewise-linear constraints," *Journal of Sound and Vibration - J SOUND VIB*, vol. 330, pp. 3196–3221, June 2011.
- [39] M. F. Beatty and Z. Ziliang, "Finite amplitude and free vibrations of a body supported by incompressible, nonlinear viscoelastic shear mountings," *International Journal of Solids and Structures*, vol. 27, pp. 355–370, Jan. 1991.

- [40] P. B. Gonçalves, R. M. Soares, and D. Pamplona, “Nonlinear vibrations of a radially stretched circular hyperelastic membrane,” *Journal of Sound and Vibration*, vol. 327, pp. 231–248, Oct. 2009.
- [41] R. A. Schapery, “An engineering theory of nonlinear viscoelasticity with applications,” *International Journal of Solids and Structures*, vol. 2, pp. 407–425, July 1966.
- [42] A. J. Culler and J. J. McNamara, “Studies on fluid-thermal-structural coupling for aerothermoelasticity in hypersonic flow,” *AIAA Journal*, vol. 48, no. 8, pp. 1721–1738, 2010.
- [43] R. D. Cook, D. S. Malkus, M. E. Plesha, and R. J. Witt, *Concepts and applications of finite element analysis*, vol. 4. Wiley New York, 1974.
- [44] J. J. Hollkamp, M. S. Spottswood, and R. W. Gordon, “Nonlinear modal models for sonic fatigue response prediction: a comparison of methods,” *Sound and Vibration*, 2005.
- [45] A. A. Muravyov and S. A. Rizzi, “Determination of nonlinear stiffness with application to random vibration of geometrically nonlinear structures,” *Computers & Structures*, vol. 81, pp. 1513–1523, July 2003.
- [46] M. McEwan, J. Wright, J. Cooper, and A. Leung, “Combined Modal/Finite Element Analysis Technique for the Dynamic Response of a Non-linear Beam to Harmonic Excitation,” *Journal of Sound and Vibration*, vol. 243, pp. 601–624, June 2001.
- [47] J. J. Hollkamp and R. W. Gordon, “Modeling Membrane Displacements in the Sonic Fatigue Response Prediction Problem,” in *46th AIAA/ASME/ASCE/AHS/ASC Structures, Structural Dynamics and Materials Conference*, American Institute of Aeronautics and Astronautics, Apr. 2005.
- [48] A. F. Vakakis, “Non-linear Normal Modes (NNMs) and their Application in Vibration Theory : An Overview,” *Mechanical Systems and Signal Processing*, vol. 11, pp. 3–22, Jan. 1997.
- [49] S. Shaw and C. Pierre, “Non-linear normal modes and invariant manifolds,” *Journal of sound and Vibration*, vol. 150, no. 1, pp. 170–173, 1991.
- [50] S. W. Shaw and C. Pierre, “Normal modes of vibration for non-linear continuous systems,” *Journal of sound and vibration*, vol. 169, no. 3, pp. 319–347, 1994.
- [51] R. J. Kuether, L. Renson, T. Detroux, C. Grappasonni, G. Kerschen, and M. S. Allen, “Nonlinear normal modes, modal interactions and isolated resonance curves,” *Journal of Sound and Vibration*, vol. 351, pp. 299–310, 2015.
- [52] T. Detroux, L. Renson, L. Masset, and G. Kerschen, “The harmonic balance method for bifurcation analysis of large-scale nonlinear mechanical systems,” *Computer Methods in Applied Mechanics and Engineering*, vol. 296, pp. 18–38, 2015.

- [53] C. I. VanDamme, B. Moldenhauer, M. S. Allen, and J. J. Holkkamp, “Computing Nonlinear Normal Modes of Aerospace Structures Using the Multi-harmonic Balance Method,” in *Nonlinear Dynamics, Volume 1*, pp. 247–259, Springer, 2018.
- [54] D. A. Ehrhardt, M. S. Allen, and R. J. Kuether, “Nonlinear Normal Modes in Finite Element Model Validation of Geometrically Nonlinear Flat and Curved Beams,” in *56th AIAA/ASCE/AHS/ASC Structures, Structural Dynamics, and Materials Conference, AIAA SciTech Forum*, 2015.
- [55] R. J. Kuether and M. S. Allen, “A numerical approach to directly compute nonlinear normal modes of geometrically nonlinear finite element models,” *Mechanical Systems and Signal Processing*, vol. 46, pp. 1–15, May 2014.
- [56] S. Peter, A. Grundler, P. Reuss, L. Gaul, and R. I. Leine, “Towards Finite Element Model Updating Based on Nonlinear Normal Modes,” in *Nonlinear Dynamics, Vol 1, Proceedings of the 33rd IMAC, A Conference and Exposition on Structural Dynamics*, 2015.
- [57] T. L. Hill, P. L. Green, A. Cammarano, and S. A. Neild, “Fast Bayesian identification of a class of elastic weakly nonlinear systems using backbone curves,” *Journal of Sound and Vibration*, vol. 360, pp. 156–170, Jan. 2016.
- [58] X. Wang, T. L. Hill, S. A. Neild, A. D. Shaw, H. Haddad Khodaparast, and M. I. Friswell, “Model updating strategy for structures with localised nonlinearities using frequency response measurements,” *Mechanical Systems and Signal Processing*, vol. 100, pp. 940–961, Feb. 2018.
- [59] M. Song, L. Renson, J.-P. Noël, B. Moaveni, and G. Kerschen, “Bayesian model updating of nonlinear systems using nonlinear normal modes,” *Structural Control and Health Monitoring*, vol. 0, p. e2258, Sept. 2018.
- [60] V. Denis, M. Jossic, C. Giraud-Audine, B. Chomette, A. Renault, and O. Thomas, “Identification of nonlinear modes using phase-locked-loop experimental continuation and normal form,” *Mechanical Systems and Signal Processing*, vol. 106, pp. 430–452, 2018.
- [61] T. Detroux, L. Renson, and G. Kerschen, “The Harmonic Balance Method for Advanced Analysis and Design of Nonlinear Mechanical Systems,” in *Nonlinear Dynamics, Volume 2* (G. Kerschen, ed.), Conference Proceedings of the Society for Experimental Mechanics Series, pp. 19–34, Springer International Publishing, 2014.
- [62] R. J. Kuether, B. Deaner, J. J. Holkkamp, and M. S. Allen, “Evaluation of Geometrically Nonlinear Reduced-Order Models with Nonlinear Normal Modes,” *AIAA Journal*, vol. 53, no. 11, pp. 3273–3285, 2015.
- [63] S. Boyd and L. Vandenberghe, *Convex Optimization*. New York, NY, USA: Cambridge University Press, 2004.

- [64] J. Friedman, T. Hastie, and R. Tibshirani, “Regularization paths for generalized linear models via coordinate descent,” *Journal of statistical software*, vol. 33, no. 1, p. 1, 2010.
- [65] S. Boyd, N. Parikh, E. Chu, B. Peleato, and J. Eckstein, “Distributed optimization and statistical learning via the alternating direction method of multipliers,” *Foundations and Trends® in Machine learning*, vol. 3, no. 1, pp. 1–122, 2011.
- [66] P. Refaeilzadeh, L. Tang, and H. Liu, “Cross-Validation,” in *Encyclopedia of Database Systems* (L. LIU and M. T. ÖZSU, eds.), pp. 532–538, Boston, MA: Springer US, 2009.
- [67] T. T. Wu and K. Lange, “Coordinate descent algorithms for lasso penalized regression,” *The Annals of Applied Statistics*, vol. 2, no. 1, pp. 224–244, 2008.
- [68] R. J. Kuether and M. S. Allen, “Validation of Nonlinear Reduced Order Models with Time Integration Targeted at Nonlinear Normal Modes,” *Nonlinear Dynamics, Volume 1 Conference Proceedings of the Society for Experimental Mechanics Series*, 2015.
- [69] R. Gordon and J. Hollkamp, “Reduced-Order Models for Acoustic Response Prediction of a Curved Panel,” in *52nd AIAA/ASME/ASCE/AHS/ASC Structures, Structural Dynamics and Materials Conference, Structures, Structural Dynamics, and Materials and Co-located Conferences*, American Institute of Aeronautics and Astronautics, Apr. 2011.
- [70] A. F. Vakakis, *Analysis and identification of linear and nonlinear normal modes in vibrating systems*. PhD thesis, California Institute of Technology, 1991.
- [71] A. H. Nayfeh, *Introduction to perturbation techniques*. John Wiley & Sons, 2011.
- [72] M. Peeters, R. Virguie, G. Serandour, G. Kerschen, and J. C. Golinval, “Nonlinear normal modes, Part II: Toward a practical computation using numerical continuation techniques,” *Mechanical Systems and Signal Processing*, vol. 23, no. 1, pp. 195–216, 2009.
- [73] C. I. VanDamme and M. S. Allen, “Using nnms to evaluate reduced order models of curved beam,” in *Rotating Machinery, Hybrid Test Methods, Vibro-Acoustics & Laser Vibrometry, Volume 8*, pp. 457–469, Springer, 2016.
- [74] R. J. Gilmore and M. B. Steer, “Nonlinear circuit analysis using the method of harmonic balance—A review of the art. Part I. Introductory concepts,” *International Journal of Microwave and Millimeter-Wave Computer-Aided Engineering*, vol. 1, no. 1, pp. 22–37, 1991.
- [75] K. C. Hall, K. Ekici, J. P. Thomas, and E. H. Dowell, “Harmonic balance methods applied to computational fluid dynamics problems,” *International Journal of Computational Fluid Dynamics*, vol. 27, pp. 52–67, Feb. 2013.
- [76] N. Kryloff, N. Bogoliuboff, and S. Lefschetz, *Introduction to Non-Linear Mechanics. (AM-11)*. Princeton University Press, 1943.

- [77] M. Urabe, “Galerkin’s procedure for nonlinear periodic systems,” *Archive for Rational Mechanics and Analysis*, vol. 20, pp. 120–152, Jan. 1965.
- [78] Y. K. Cheung and S. L. Lau, “Incremental time—space finite strip method for nonlinear structural vibrations,” *Earthquake Engineering & Structural Dynamics*, vol. 10, no. 2, pp. 239–253, 1982.
- [79] S. L. Lau and Y. K. Cheung, “Amplitude Incremental Variational Principle for Nonlinear Vibration of Elastic Systems,” *Journal of Applied Mechanics*, vol. 48, pp. 959–964, Dec. 1981.
- [80] K. Y. Sze, S. Chen, , and J. L. Huang, “The incremental harmonic balance method for nonlinear vibration of axially moving beams,” *Journal of sound and vibration*, vol. 281, no. 3-5, pp. 611–626, 2005.
- [81] L. Liu, E. H. Dowell, and J. P. Thomas, “A high dimensional harmonic balance approach for an aeroelastic airfoil with cubic restoring forces,” *Journal of Fluids and Structures*, vol. 23, pp. 351–363, Apr. 2007.
- [82] A. LaBryer and P. J. Attar, “A harmonic balance approach for large-scale problems in nonlinear structural dynamics,” *Computers & Structures*, vol. 88, pp. 1002–1014, Sept. 2010.
- [83] J. Didier, J. J. Sinou, and B. Faverjon, “Nonlinear vibrations of a mechanical system with non-regular nonlinearities and uncertainties,” *Communications in Nonlinear Science and Numerical Simulation*, vol. 18, pp. 3250–3270, Nov. 2013.
- [84] T. M. Cameron and J. H. Griffin, “An alternating frequency/time domain method for calculating the steady-state response of nonlinear dynamic systems,” *Journal of applied mechanics*, vol. 56, no. 1, pp. 149–154, 1989.
- [85] J. L. Hwang and T. N. Shiau, “An Application of the Generalized Polynomial Expansion Method to Nonlinear Rotor Bearing Systems,” *Journal of Vibration and Acoustics*, vol. 113, pp. 299–308, July 1991.
- [86] G. Xie and J. Y. K. Lou, “Alternating frequency/coefficient (AFC) technique in the trigonometric collocation method,” *International Journal of Non-Linear Mechanics*, vol. 31, pp. 531–545, July 1996.
- [87] F. Bonani and M. Gilli, “Analysis of stability and bifurcations of limit cycles in chuas circuit through the harmonic-balance approach,” *Circuits and Systems I: Fundamental Theory and Applications*, vol. 46, pp. 881–890, 1999.
- [88] A. Dhooge, W. Govaerts, and Y. A. Kuznetsov, “MATCONT: a MATLAB package for numerical bifurcation analysis of ODEs,” *ACM Transactions on Mathematical Software (TOMS)*, vol. 29, no. 2, pp. 141–164, 2003.

- [89] C. I. VanDamme and M. S. Allen, “Nonlinear Normal Modes of a Curved Beam and Its Response to Random Loading,” in *Nonlinear Dynamics, Volume 1*, pp. 115–126, Springer, 2017.
- [90] P. Shah, E. Blades, M. Nucci, J. Schoneman, A. Cornish, and T. Hill, “Nonlinear dynamic response of hypersonic vehicle skin panels using coupled fluid-thermal-structural simulation tools,” in *Proceedings of the 35th International Modal Analysis Conference*, 2017.
- [91] L. Renson, G. Kerschen, and B. Cochelin, “Numerical computation of nonlinear normal modes in mechanical engineering,” *Journal of Sound and Vibration*, vol. 364, pp. 177–206, Mar. 2016.
- [92] R. H. Byrd, M. E. Hribar, and J. Nocedal, “An interior point algorithm for large-scale nonlinear programming,” *SIAM Journal on Optimization*, vol. 9, no. 4, pp. 877–900, 1999.
- [93] R. H. Byrd, J. C. Gilbert, and J. Nocedal, “A trust region method based on interior point techniques for nonlinear programming,” *Mathematical Programming*, vol. 89, pp. 149–185, Nov. 2000.
- [94] W. Squire and G. Trapp, “Using Complex Variables to Estimate Derivatives of Real Functions,” *SIAM Review*, vol. 40, no. 1, pp. 110–112, 1998.
- [95] A. Voorhees, H. Millwater, and R. Bagley, “Complex variable methods for shape sensitivity of finite element models,” *Finite Elements in Analysis and Design*, vol. 47, pp. 1146–1156, Oct. 2011.
- [96] G. Lantoine, R. P. Russell, and T. Dargent, “Using Multicomplex Variables for Automatic Computation of High-Order Derivatives,” *ACM Trans. Math. Softw.*, vol. 38, pp. 16:1–16:21, Apr. 2012.
- [97] J. Garza and H. Millwater, “Multicomplex newmark-beta time integration method for sensitivity analysis in structural dynamics,” *AIAA Journal*, vol. 53, no. 5, pp. 1188–1198, 2015.
- [98] N. Olhoff and J. Du, “Structural Topology Optimization with Respect to Eigenfrequencies of Vibration,” in *Topology Optimization in Structural and Continuum Mechanics* (G. I. N. Rozvany and T. Lewiński, eds.), CISM International Centre for Mechanical Sciences, pp. 275–297, Vienna: Springer Vienna, 2014.
- [99] A. P. Seyranian, E. Lund, and N. Olhoff, “Multiple eigenvalues in structural optimization problems,” *Structural optimization*, vol. 8, pp. 207–227, Dec. 1994.
- [100] P. Spellucci, “A new technique for inconsistent QP problems in the SQP method,” *Mathematical Methods of Operations Research*, vol. 47, pp. 355–400, Oct. 1998.

- [101] R. Perez, G. Bartram, T. Beberniss, R. Wiebe, and S. M. Spottswood, “Calibration of aero-structural reduced order models using full-field experimental measurements,” *Mechanical Systems and Signal Processing*, vol. 86, pp. 49–65, Mar. 2017.
- [102] D. A. Ehrhardt, M. S. Allen, T. J. Beberniss, and S. A. Neild, “Finite element model calibration of a nonlinear perforated plate,” *Journal of Sound and Vibration*, vol. 392, pp. 280 – 294, 2017.
- [103] M. Peeters, G. Kerschen, and J. Golinval, “Modal testing of nonlinear vibrating structures based on nonlinear normal modes: Experimental demonstration,” *Mechanical Systems and Signal Processing*, vol. 25, no. 4, pp. 1227–1247, 2011.
- [104] “Overview of materials for Polylactic Acid (PLA) Biopolymer.”
- [105] C. I. VanDamme and M. S. Allen, “Using Nonlinear Normal Modes to Optimize the Design of Geometrically Nonlinear Structures,” in *AIAA/ASCE/AHS/ASC Structures, Structural Dynamics, and Materials Conference*, 2019.
- [106] J. D. Schoneman, C. Ostoich, L. Jarman, C. I. VanDamme, and M. S. Allen, “Impact of Flow and Structural Nonlinearities on Hypersonic Panel Flutter Predictions,” in *AIAA/ASCE/AHS/ASC Structures, Structural Dynamics, and Materials Conference*, American Institute of Aeronautics and Astronautics, 2018.
- [107] C. I. VanDamme and M. S. Allen, “Evaluating NLRMs’ Ability to Predict Dynamic Snap Through of a Curved Beam in a Random Loading Environment,” in *58th AIAA/ASCE/AHS/ASC Structures, Structural Dynamics, and Materials Conference*, American Institute of Aeronautics and Astronautics, 2017.
- [108] L. M. Jarman, C. VanDamme, and M. S. Allen, “Nonlinear Dynamic Analysis of a Thermally Buckled Aircraft Panel Using NNMs,” in *Shock & Vibration, Aircraft/Aerospace, Energy Harvesting, Acoustics & Optics, Volume 9*, pp. 59–69, Springer, 2017.